# Wetting on micro-structured surfaces: modelling and optimization

**Cavalli, Andrea; Okkels, Fridolin; Bøggild, Peter; Taboryski, Rafael J.**

*Publication date:*
2013

*Document Version*
Publisher's PDF, also known as Version of record

Technical University of Denmark (DTU)
Department of Micro- and Nanotechnology

Doctor of Philosophy Dissertation

# Wetting on micro-structured surfaces: modelling and optimization.

Ph.D. Candidate: **Andrea Cavalli**

Supervisor: Associate Prof. Fridolin Okkels

Co-supervisors: Associate Prof. Peter Bøggild,
Associate Prof. Rafael J. Taboryski

Kgs. Lyngby, 2013

# Contents

# List of Symbols and Abbreviations

| Abbreviation | Description | Definition |
|---|---|---|
| FEM | Finite Element Method | page 6 |
| LB | Lattice Boltzmann (method) | page 6 |
| PDE | Partial Differential Equation | page 19 |
| $\mathbf{x}, x_\alpha$ | Coordinate vector | page 23 |
| $\partial_\alpha$ | Partial derivative with respect to $\alpha$-coordinate | page 20 |
| $\mathbf{u}, u_\alpha$ | Velocity field, with components $\{u, v\}$ (2D) or $\{u, v, w\}$ (3D). | page 23 |
| $P_{\alpha\beta}$ | Pressure tensor, $P_{\alpha\beta} = \mathrm{p}\ \delta_{\alpha\beta}$ if not otherwise specified. | page 23 |
| $\mu$ | Dynamic viscosity [Pa s] | page 33 |
| $\rho$ | Fluid Density [Kg / $\mathrm{m}^3$] | page 33 |
| $\gamma, \gamma_{lg}$ | Liquid-Gas surface tension [J/$\mathrm{m}^2$] | page 10 |
| $\gamma_{sg}$ | Solid-Gas surface tension [J/$\mathrm{m}^2$] | page 12 |
| $\gamma_{sl}$ | Solid-Liquid surface tension [J/$\mathrm{m}^2$] | page 12 |
| $l_c$ | Capillary length [m] | |
| $\theta, \theta_Y$ | Young contact angle [rad or $^o$] | page 12 |
| r | Roughness factor | page 15 |
| $f_{sl}$ | Solid-liquid interface per base area of the drop | page 16 |
| $\theta_W$ | Wenzel apparent contact angle [rad or $^o$] | page 15 |
| $\theta_{CB}$ | Cassie-Baxter apparent contact angle [rad or $^o$] | page 16 |
| $\chi(\mathbf{x})$ | Topology optimization design variable | page 28 |
| $s(\mathbf{x})$ | Liquid-Air interface displacement | page 38 |
| $\Delta P$ | Pressure difference at the liquid-air interface | page 10 |
| $L_{diff}$ | Topology optimization filter length | page 41 |
| Oh | Ohnesorge number, $\mathrm{Oh} = \frac{\mu}{\sqrt{\rho\gamma \mathrm{R}}}$ | page 74 |
| Bo | Bond number, $\mathrm{Bo} = \frac{\mathrm{R}^2 \mathrm{g}(\rho_{\mathrm{liq}} - \rho_{\mathrm{air}})}{\gamma}$ | page 74 |

# Abstract

The present thesis deals with the wetting of micro-structured surfaces by various fluids, and its goal is to elucidate different aspects of this complex interaction. In this work we address some of the most relevant topics in this field such as superhydrophobicity, oleophobicity, unidirectional liquid spreading and spontaneous drop removal on superhydrophobic surfaces. We do this by applying different numerical techniques, suited for the specific topic.

We first consider superhydrophobicity, a condition of extreme water repellency associated with very large static contact angles and low roll-off angles. Such behaviour arises when drops are suspended on a micron or submicron texture, so that their contact with the substrate is minute. This suspended state (known as Cassie-Baxter state) is however prone to failure if the liquid-air interface is perturbed, a common situation in real life circumstances. We apply the numerical method of Topology Optimization to this problem, in order to find the optimal texture to support the superhydrophobic configuration. Our optimization provides designs which are consistent with strategies employed by Nature to achieve the same effect. Furthermore, our control over the length scale and resolution of the design allow us to obtain patterns which are not only optimal but also suitable for microfabrication.

We next consider oleophobicity, which is the ability to repel low surface tension liquids through a combination of surface patterning and chemical properties. Our analysis considers a simple geometry already described in literature. We however characterize it in a novel way, trying to account simultaneously for both the wetting and mechanics properties of the texture. Such analysis is of high relevance for technical applications of these micro-patterns, and suggests that there is a balance between optimal wetting properties and mechanical robustness of the microposts.

We subsequently analyse liquid spreading on surfaces patterned with slanted microposts. Such a geometry induces unidirectional liquid spreading, as observed in several recent experiments. Our numerical analysis shows how such spreading can be tuned and controlled in terms of lattice properties of the texture and

wetting properties of the materials.

We conclude by analysing the phenomenon of self-propelled ejection of coalescing droplets on superhydrophobic surfaces. This remarkable phenomenon is due to a transformation of surface energy to kinetic energy, and could have several technical applications in the fields of heat exchange and enhanced condensation. We discuss different dissipation mechanisms in the process as well as how the drop properties (size, shape) affect the phenomenon.

Although the modelling and simulation of these wetting interactions plays a major role in the thesis, throughout the research activity we focus on two further aspects. First, we tune the relevant physical parameters to be as close as possible to experimental data. We also had different opportunities to collaborate with colleagues at DTU Nanotech and at other research institutes to experimentally test the wetting properties of selected surface patterns. Second, we apply an optimization approach to our analysis, i.e. we try to enhance specific wetting properties through changes in the texture geometry. A successful optimization is the natural consequence of an in-depth understanding of the wetting process, since a meaningful choice of design variables and optimization functions is fundamental to achieve an improved performance.

# Dansk Resumé

Den engelske titlen på Andrea Cavallis PhD afhandling er " Wetting on micro-structured surfaces: modelling and optimization" og omhandler vædningen af mikro-strukturerede overflader med forskellige væsker, og har som mål at forklare de forskellige aspekter af denne komplekse vekselvirkning. Ud over at beskrive og forklare de grundlæggende måder hvorpå væsker kan ligge eller sprede sig ud på en overflade, så har Andrea Cavalli også benyttet den strukturelle optimeringsmetode, Topologi optimering, til at udregne de bedst mulige overflade mikro-strukturer for at opnå vandskyende overflader (hydrofobe). Dette design er vha. rentrumsprocesser realiseret som virkelige mikrostrukturerede overflader, der derefter er karakteriseret i et samarbejde med andre studerende på DTU Nanotech. Andre strukturelle optimeringsmetoder er også benyttet til at designe hydrofobe overflader, hvor mikro-strukturerne desuden har stor mekanisk stabilitet, hvilke er vigtigt for den praktiske anvendelighed af overfladerne.

Andrea Cavalli har under sine to udenlandsophold i Oxford, UK og MIT, USA, arbejdet med relaterede overflade-effekter: Ved hjælp af små skrå søjler på en overflade at lede en vanddråbes spredning langs en speciel rute, samt hvordan mikro-overfladestrukturer kan forbedre kondenseringen af damp/gasser på en køle-flade.

Dette PhD projekt er finansieret af innovations konsortiet NanoVation, ledet af Leif Højslet Christensen, Dansk Teknologiske Institut.

# Acknowledgements

I made it by being tougher than the toughies and
smarter than the smarties. And I made it square!
Scrooge McDuck

But I could not have done it alone. Writing a Ph.D. thesis is a hard task, as I found out, and many people have to be acknowledged. First of all, I would like to thank my supervisor Fridolin Okkels for his constant and careful supervision. Through all my Ph.D. he always supported me in pursuing my research freely, while maintaining the necessary focus. I am also grateful to my co-supervisors Peter Bøggild and Rafael Taboryski, in particular for providing me with stimulating and challenging "real-life" constraint on my research, and suggesting interesting collaborations throughout the course of the Ph.D. I would like to thank all the members of the TMSO group at DTU Nanotech for their friendship and support to my research. I am particularly thankful to my office mate Kristian E. Jensen for the long hours spent in stimulating discussions.
I also thank Nis K. Andersen, Øistein Wind-Willassen and Emil Søgard for frequent brainstorming sessions on capillarity and wetting phenomena. A special thanks goes to Prof. Yeomans and her research group in Oxford, in particular Lisa Moevius and Matthew Blow. They provided me with an exciting and friendly environment, which was extremely beneficial to my work.
I am also thankful to Prof. Bush for his supervision during my visit at MIT. Although short, this experience has been extremely fruitful in widening my scope and understanding of wetting phenomena. I would also like to thank David Martin and Nenad Miljkovic for taking part in this exciting collaboration.
I would like to acknowledge the NanoVation consortium, headed by Leif Højslet Christensen, for funding my Ph.D. project, and providing a rich network of fellow researcher to discuss with. I am also grateful to the Oticon fonden, Reinholdt W. Jorck fonden, Otto Mønsted fonden and Fabrikant P.A. Fisker fonden for their

financial support to my travel expenses through my Ph.D.
My research involved a lot of travelling, and I have been blessed with many good friends in all my destinations, who helped me tackling the stress and celebrating successes. I therefore want to thank all my friends in Venice, Copenhagen, Oxford, Boston and anywhere else for the great time spent together.
Last but not least I am grateful to my family, who always supported me through hard times, and encouraged me to pursue my dreams.

# Chapter 1

# Introduction

The physics of wetting is concerned with phenomena involving the interaction of two fluid phases (typically, a liquid and a gas), and a solid surface. The wetting properties of a substrate are a direct consequence of its physical and chemical properties, and play a relevant role in designing bio-compatible, self-cleaning or low-drag materials. Since each Chapter of this thesis will have its own introduction, the aim of this Section is to describe the scope of the thesis in a broader sense. We will first introduce several examples of wetting phenomena in nature. We will then review how these natural textures have inspired artificial micro-textured coatings with similar properties. We will eventually give a brief overview of the thesis, including an account of my scientific output throughout the Ph.D.

## 1.1 Wetting in nature

Nature offers several examples of organisms who adapted their "skin" to achieve specific wetting properties.

For instance, water repellent leaves are widespread, and they all share several common features [2]. Among those, the presence of hierarchical micro- and nanostructures, usually coated with hydrophobic wax-like materials. This combination of chemical and topographic features reduces the adhesion of water to the substrate, so that droplets easily roll on such surfaces, carrying away dust and debris in their way. This design has thus been an inspiration for several artificial self-cleaning surfaces. The lotus leaf is the most cited example of extreme water repellency, its properties known since ancient times (see Fig.1.1). An even more extreme repellent property has recently been observed in springtails, arthropods who live in soil and decaying materials, whose carapace is able to repel oils and organic fluids thanks to a "mushroom like" overhanging texture [3]. Another way

Figure 1.1: Drops of water on a lotus leaf. The so called "Lotus effect" is one of the best known examples of superhydrophobicty, [1]. The extreme water repellency of this surface comes from a hierarchical micro-nano roughness and a wax-like coating of the smaller features. Photo via tanakawho on Flickr CC.

to get rid of undesired drops is unidirectional liquid motion. Butterfly wings, for example, are patterned with a ratchet micro-structure. By flapping their wings, the insect forces the occasional raindrop in the outward direction by a "conveyor belt" transport, thus avoiding getting wet [4]. The feathers of several birds also show enhanced water repellency [5]. The texture on feathers is typically elongated, and this gives rise to a directional motion of droplets, which in turn facilitates their removal.

Surface patterning can also be applied to control phase transitions, such as vapour condensation. The Namib desert beetle [6], for instance, is able to collect atmospheric dew on a highly-wettable spot on its carapace. Once the condensing drop reaches a critical size, it will roll to its mouth parts to be drunk. Eventually, the ability of water striders to walk at the water-air interface exploiting surface tension is again a direct consequence of the size and microstructure of their legs [7, 8]. Their weight is balanced by the deformation they impose to the water interface, which results in a net upward lift.

In summary, nature has thus been able to engineer different substrate to achieve valuable wetting behaviours. Our goal in this thesis is to describe in detail the physics behind these remarkable wetting properties, in order to understand them and possibly enhance them even more.

## 1.2 Wetting and microfabrication

Recent advances in microfabrication have made it possible to mimic the natural textures described in the previous Section. Micro-patterns have been realized on different materials with different lithographic techniques, as we will now briefly

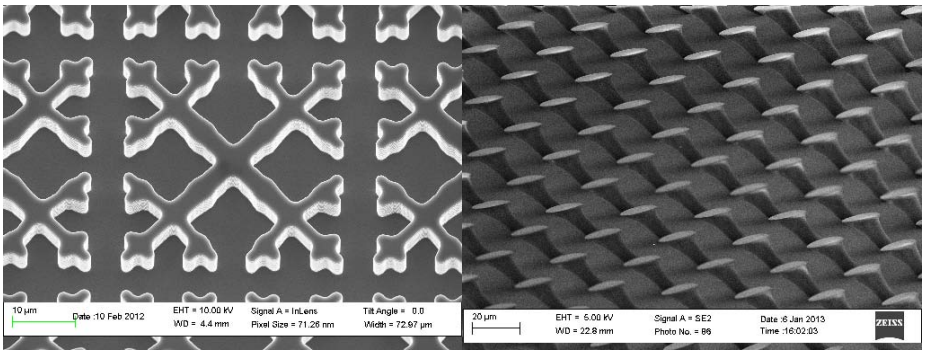


Figure 1.2: Left: topology optimized pattern for superhydrophobic surfaces. Fabrication and image by Nis K. Andersen. Right: Slanted SU8 micro-posts via inclined UV lithography. Fabrication and image by Mikkel B. Klarskov.

describe. Superhydrophobic surfaces, i.e. surfaces characterized by very low water adhesion, are among the first on which wetting research has focused, with significant results already in the late '90s [9, 10, 11]. Regular arrays of microposts and rough fractal surfaces have been shown to exhibit superhydrophobicity over a wide range of experimental conditions. The effect of several geometric parameters on the stability of the superhydrophobic state has been extensively discussed, and will also be one of main the topics of this thesis. The reduced adhesion observed on superhydrophobic surfaces is also at the origin of peculiar phenomena, such as the spontaneous ejection of coalescing droplets on such surfaces, which could find interesting applications to heat exchange devices [12].

An even more interesting property is oleophobicity, that is, the ability to repel low surface tension fluids. As we will discuss in the next Chapters, oleophobic surfaces are typically characterized by overhanging features, whose fabrication is challenging. In the last few years, however, they have been successfully realized in different shapes and materials, such as Tuteja's "micro-hoodoos" [13], Ahuja's nanonails [14] and Im's inverse trapezoids [15].

Controlled wetting and unidirectional liquid spreading are also dynamic research fields, with many relevant papers published in the last years. Chu [16] observed unidirectional liquid spreading on bent silicon nanopillars, while Guo [17] realised polymer replica of taper-ratchet features from rye grass leaves. Sekeroglu [18] also observed the unidirectional transport of encapsulated gel on similar textures.

In a similar way, polygonal patterns have been shown to control the spreading of drops, which follows the lattice orientation because of pinning of the contact line [19]. A similar controlled spreading can be achieved by chemical pattering of the surface, with patches of hydrophilic and hydrophobic materials determining the liquid spreading [20].

While the focus of this thesis will be on the modelling and optimization of micro-patterns to achieve desired wetting properties, we have closely collaborated with colleagues at DTU Nanotech to fabricate and test our designs. In Fig.1.2, we show two examples of such collaborative efforts: a topology optimized post array fabricated in silicon through e-beam lithography (Fig.1.2a) by Nis K. Andersen, and slanted microposts in SU8 fabricated by Mikkel Buster Klarskov via inclined UV lithography [21] (Fig.1.2b). These structures are currently being characterized in terms of their wetting properties, and preliminary results on their performance will be described in the following chapters.

Moreover, experimental results on these and other designs provide invaluable input to our simulations, in terms of feasible length scales, chemical properties, and (last but not least) cost effectiveness of different patterning technologies.

## 1.3 Thesis outline

### Chapter 2: Physics of Wetting

We introduce the relevant equations governing capillarity and wetting of solid surfaces. In particular, we introduce the different wetting configuration on rough or textured surfaces, such as the Cassie-Baxter and Wenzel states. We also discuss the thermodynamic stability of different wetting configuration, and how metastable states can be achieved through pinning of the liquid-air interface.

### Chapter 3: Numeric Methods

We describe the different numeric methods that we employed to describe the fluid dynamics of two-phase flows. We briefly introduce the Finite Elements Method (FEM) , the Lattice Boltzmann (LB) method and a Finite Difference scheme. We also describe Topology optimization, an optimization technique that we apply in Chapter 5.

### Chapter 4: Interface Models

We present different constitutive models to describe the liquid-air interface in mathematical and numeric terms. We particularly focus on the difference between diffuse interface descriptions and sharp interface models, which have both been used in different part of the project.

### Chapter 5: Topology Optimization of Robust Superhydrophobic Surfaces

In this Chapter we apply the tools of topology optimization to maximise the robustness of the Cassie-Baxter configuration with respect to an external pertur-

bation (an applied pressure). For a given solid fraction, we search for an optimal post cross section that offers the best support to the liquid-air interface. We find optimal designs that are reminiscent of natural strategy to achieve the same goal. These patterns have been fabricated and characterized in collaboration with Nis K. Andersen as part of his M.Sc. final project.

### Chapter 6: Parametric Optimization of Oleophobic Surfaces

In this Chapter we discuss how to obtain a oleophobic behaviour from an oleophilic material. Since most materials are inherently oleophilic, texturing the surface is the only way to significantly alter their wetting properties. We particularly focus on inverse trapezoids, a simple yet experimentally relevant [15] geometry to achieve oleophobicity. We describe how these overhanging structures, which are effective from the wetting point of view, could perform poorly in term of mechanical robustness. An optimum post shape is therefore identified, accounting for wetting and mechanical constraints at the same time.

### Chapter 7: Unidirectional Liquid Spreading on Surfaces Patterned with Slanting Microposts

In this Chapter we discuss how slanted micro-posts can be used to achieve unidirectional spreading. We use a Lattice Boltzmann algorithm to simulate the quasi-static spreading of drops on a patterned hydrophilic substrate, and we analyse the influence of several geometric parameters on the process.

### Chapter 8: Jumping of Coalescing Droplets on Superhydrophobic Substrates

In this Chapter we analyse the observed jumping motion of coalescing drops on superhydrophobic substrates, due to the release of surface energy in the merging process. We discuss the relation between the jump height (or speed) and the coalescing drops' size and shape. We also identify relevant dissipation mechanisms that could hinder the process.

### Chapter 9: Conclusions and Outlook

We summarize the results obtained and briefly outline future research work.

## 1.4 Publications during the PhD studies

The results described in this thesis have been presented in the following papers:

- A. Cavalli, P. Bøggild and F. Okkels, *Parametric Optimization of Inverse Trapezoid Oleophobic Surfaces*, Langmuir, 2012, 28 (50), pp. 17545–17551, enclosed in Chapter 5

- A. Cavalli, P. Bøggild and F. Okkels, *Topology Optimization of Robust Superhydrophobic Surfaces* , Soft Matter, 2013, 9 (7),pp. 2234-2238, enclosed in Chapter 4

- A. Cavalli, M. L. Blow and J. M. Yeomans, *Modelling of liquid spreading on unidirectional wetting surfaces* , Soft Matter, 2013, enclosed in Chapter 6

- A. Cavalli, N. Miljkovic, D. Martin and J. W. M. Bush *Jumping behaviour of coalescing droplets on superhydrophobic substrates*, under preparation, based on the results presented in chapter 8.

During my Ph.D. studies I attended the following conferences:

- A. Cavalli, M, L. Blow and J. M. Yeomans, *Modelling liquid interaction with slanted microposts for microfluidics applications*, abstract and oral presentation at Advances in Microfluidics & Nanofluidics 2013, May 24-26, 2013, University of Notre-Dame, Indiana, USA

- A. Cavalli, P. Bøggild and F. Okkels, *Structural Optimization of super Repellent Surfaces*, paper in conference proceedings and oral presentation at 10th World Congress on Structural and Multidisciplinary Optimization (WCSMO 10), May 19 - 24, 2013, Orlando, Florida, USA

- A. Cavalli, P. Bøggild and F. Okkels, *Topology Optimization of Robust Superhydrophobic Surfaces* , abstract and oral presentation at 3rd international conference on engineering optimisation (ENGOPT 2012), July 1-5, 2012, Rio de Janeiro, Brazil.

Further scientific activities include:

- A. Cavalli, F. Malet, J. C. Cremon and S. M. Reimann, *Spinorbit-enhanced Wigner localization in quantum dots*, Phys. Rev. B, 2010, 84, pp. 235117

- A. Cavalli, F. Malet, J. C. Cremon and S. M. Reimann, *Rashba coupling in few-electron Quantum Dots*, abstract and poster at International Symposium on Cold Atoms and Condensed Matter, October 4-7, 2010, Vedbæk, Denmark

- A. Cavalli, *Piu' pesi e piu' misure*, popular science article on "Post" n.4, ISBN 9788857512501

# Chapter 2

# Physics of Wetting

In this Chapter we introduce some relevant aspects of the physics of wetting, that we will apply in the rest of the thesis. We first introduce the fundamental concepts of surface tension and Young contact angle, as well as the capillary length, the characteristic scale below which capillarity forces become dominant with respect to gravity. We then briefly describe fundamental results in the wetting of textured surfaces, and introduce the Wenzel and Cassie-Baxter configurations.

## 2.1 Surface tension

The first concept we need to introduce is surface tension, a fundamental property of liquids that we can observe in countless everyday occasions, from morning dew to raindrops.

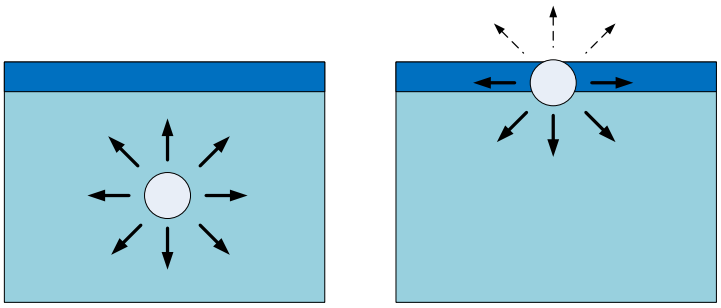

Figure 2.1: The origin of surface tension is visualized in this sketch: a molecule in the bulk (left) will share strong bonds with all its neighbours, while a molecule at the interface (right) will be connected to fewer liquid molecules, resulting in a higher energy configuration.

By surface tension we refer to the energy cost per unit area of an interface

between a liquid and another immiscible fluid. Its origin are to be found at the molecular level. Liquid molecules are tied by chemical bonds, and it is therefore energetically favourable for them to have as many neighbouring molecules of the same specie as possible. Molecules at the interface will have less neighbours, and therefore they will be in an higher energy state. Hence, any finite amount of liquid will try to minimize its exposed surface. In the following we will denote the surface tension between a liquid and gas phase by $\gamma$, or, if more precision is needed, $\gamma_{lg}$ . Its units are those of energy per surface, [J/m$^2$].

## 2.2 Young-Laplace equation

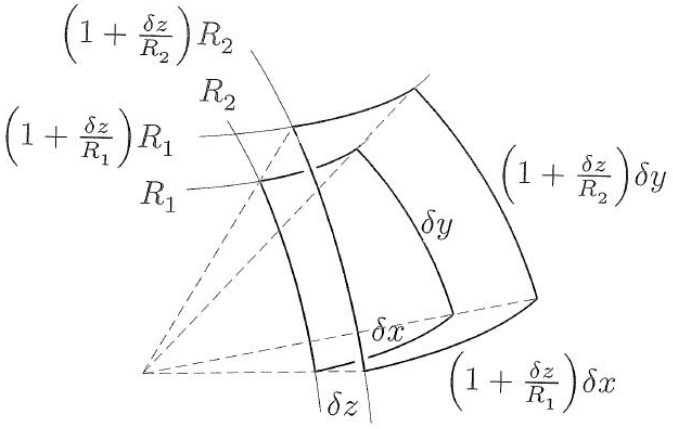


Figure 2.2: The geometry considered to derive the Young-Laplace equation is sketched. Reproduced from [22].

A consequence of surface tension is the presence of a pressure difference $\Delta P$ between a liquid drop and the medium. To understand why, let's consider a small section of the interface between a liquid and gas phase, as sketched in Fig.2.2. We now dilate the surface by an infinitesimal amount $\delta z$ along the normal to the surface, and orient the x and y axes along the two principal curvature directions. As a consequence, the local radii of curvature change from $R_i$ to $R_i + \delta z = (1 + \frac{\delta z}{R_i})R_i$. Similarly, the area $A = \delta x \delta y$ also increase to $A + \delta A = (1+\frac{\delta z}{R_1})\delta x\ (1+\frac{\delta z}{R_2})\delta y \simeq (1+\frac{\delta z}{R_1}+\frac{\delta z}{R_2})A$. The change $\delta G$ in the Gibbs free energy of the system, for an infinitesimal displacement with respect to the equilibrium configuration, must be zero. For the considered displacement, we therefore have:

$$\delta G = \gamma\left(\frac{1}{R_1}+\frac{1}{R_2}\right)A\delta z - \Delta P \delta V = 0, \tag{2.1}$$

where $\delta V = A\delta z$ is the infinitesimal change in drop volume due to the displacement of the interface. We recognize $\kappa = \left(\frac{1}{R_1}+\frac{1}{R_2}\right)$ as the local mean curvature

of the interface, and we eventually get the Young-Laplace equation:

$$\Delta P = \gamma\kappa, \tag{2.2}$$

i.e. the pressure difference across the interface is equal to the surface tension $\gamma$ times the mean interface curvature $\kappa$ (the higher pressure being in the phase containing the centre of curvature). This relation is fundamental in determining the shape of a liquid-gas interface, as we can already see. It is clear that, if we exert a pressure difference $\Delta P$ across a liquid-air interface, the higher the surface tension, the less the liquid-air interface will deform. Moreover, since curvature has units of inverse length, high pressures are required to produce deformations of the interface on a small length scale. These aspects play a relevant role in the wetting of textured surfaces, as we will discuss later.

## 2.3 Capillary length

We have seen how liquid-air interfaces come at an energy cost. Surface tension will then favour minimal surface configurations for liquid drops, i.e. spheres (or spherical caps on a solid surface, as we will see in the next section). However, in our daily experience it is common to observe free liquid assuming different rest shapes, such as puddles. This is due to the effect of other forces that contribute to the overall liquid-air interface shape. The most common example is gravity, which plays a significant role on large drops by flattening their profile, in order to reduce the gravitational energy of the liquid. A simple scaling argument allows us to derive the capillary length $l_c$, over which gravity starts to dominate over capillarity. If we search for a characteristic length $L$, at which the Young-Laplace pressure $\simeq \gamma/L$ and the correspondent hydrostatic pressure $\simeq \rho g L$ are equal, we get:

$$l_c = \sqrt{\frac{\gamma}{\rho g}}. \tag{2.3}$$

For water at $20^oC$, $l_c = 2.7$ mm. This constitutes a clear upper bound on the size of the systems we will consider in the following sections, at least as long as we focus on capillarity effects only.

## 2.4 Wetting

We now turn to the main topic of the thesis, which is the interaction of drops with solid substrates. There are now three phases involved, typically a liquid (the drop), a gas (the medium) and a solid (the substrate). liquid-gas, liquid-solid and solid-gas interfaces all have an energetic cost, since chemical bonds with molecules of the same specie are missing for the atoms or molecules at the boundary. In analogy with the surface tension between the liquid and gas phase, which we will

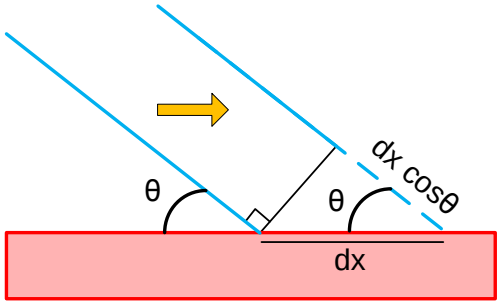


Figure 2.3: Sketch of an infinitesimal displacement of the contact line on a smooth surface. The associated energy cost depends on the surface energies of the liquid-air, liquid-solid and solid-air interfaces.

indicate as $\gamma_{lg}$, we can therefore introduce a solid-gas surface energy $\gamma_{sg}$ and a solid-liquid surface energy $\gamma_{sl}$*. We will call contact line the line where the three phases meet. The shape of a drop on a smooth surface depends on the balance between these forces. As suggested by DeGennes [1], we can define a spreading parameter $S = \gamma_{sg} - (\gamma_{sl} + \gamma_{lg})$, which is the energy cost per unit area in wetting a dry substrate with a liquid film. If $S > 0$, it is energetically favourable for the liquid phase to spread indefinitely†, to wet as large a solid area as possible. If $S < 0$, the liquid will only wet a finite area, and form an angle to the solid substrate. To find its value, consider the change in energy $\delta E$ for an infinitesimal displacement $\delta x$ of the contact line (see Fig.2.3). We have:

$$\delta E = (\gamma_{sl} - \gamma_{sg})\,\delta x + \gamma_{lg}\delta x \cos\theta \tag{2.4}$$

At equilibrium, the energy change for an infinitesimal displacement will be zero. We therefore get:

$$\cos\theta_Y = \frac{\gamma_{sg} - \gamma_{sl}}{\gamma_{lg}}. \tag{2.5}$$

This angle is known as Young or equilibrium contact angle $\theta_Y$ . If gravity can be neglected, the rest shape of a drop on a perfectly smooth surface will then be a spherical cap of suitable volume and with a contact angle equal to the Young contact angle. If $\theta_Y < 90^o$, the material is said to be "philic" with respect to the considered fluid. In this case, it is energetically favourable for the solid phase to be wet, and the liquid will tend to adhere to the substrate. If instead $\theta_Y > 90^o$, we will talk about "phobic" materials‡. In this case the contact with the substrate is energetically unfavourable, and the liquid drop retain an almost spherical shape.

*It is worth mentioning that, while it is relatively straightforward to measure liquid-gas surface tensions and contact angles, liquid-solid and solid-gas surface energies are difficult to characterize separately.

†Down to nanometric thickness: below that, the film thickness is comparable to the molecular bound range, and a continuum description is not suitable any more

‡From the greek "philos", meaning love, and "phobos", meaning fear. If the liquid considered is water, we will talk about "hydrophilic" and "hydrophobic" materials.

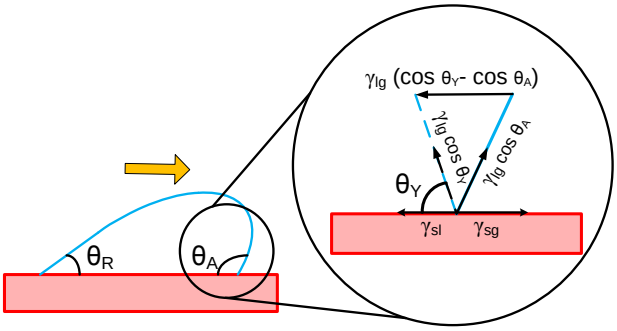


Figure 2.4: Sketch of a deformed drop under an applied volume force from left to right, showing the advancing, $\theta_A$, and receding, $\theta_R$, contact angles. In the insert, we show the initial force balance for an unperturbed shape (dashed lines), and the updated interface position and surface force for the deformed drop, with the resulting net force at the contact line equal to $\gamma_{lg}(\cos\theta_A - \cos\theta_Y)$.

Another relevant concept to introduce is contact angle hysteresis. Real surfaces are never atomically smooth. The presence of roughness and defects typically hinders the motion of drops by pinning the contact line. If a force is applied to the liquid (for example, if the surface is tilted, so that gravity exerts a component parallel to the surface), the drop will not immediately move but rather deform, showing advancing and receding contact angles $\theta_R < \theta_Y < \theta_A$, as sketched in Fig.2.4. If the contact angle is different from the equilibrium value, a force equal to $F_H = \gamma_{lg}(\cos\theta - \cos\theta_Y)$ will act on each contact line section, opposing the drop motion. Contact angle hysteresis plays a major role in determining the wetting properties of a substrate, especially when micrometric patterns are involved. As a matter of fact, a large static contact angle does not necessarily mean an easy drop removal from the substrate, since the hysteretic behaviour of the surface can also be large. We will elaborate on this point in the upcoming sections. We conclude by introducing Gibbs theory [23] for the detachment of an interface from a sharp corner. The pinning occurs because the interface would have to form an angle with the adjacent surface that differs from the equilibrium angle. Therefore, as sketched in Fig.2.5, even if a perturbation changes the local contact angle, the interface will not move as long as $\theta < \theta_A + \psi$, $\psi$ being the corner amplitude.

## 2.5 Wetting on textured surfaces

The fairly simple description of wetting we introduced in Section 2.4 gets richer on rough or textured surfaces. Once again, the equilibrium configuration is determined by a surface energy balance, which now has to account for the topography of the substrate. As sketched in Fig.2.6, there are several possible configuration

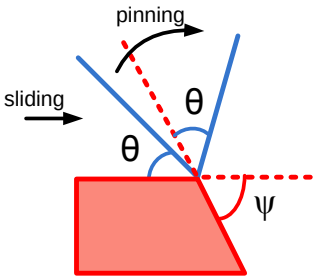


Figure 2.5: Gibbs' pinning on the corner of a post. The interface remains pinned to the post over the range of angles indicated by $\psi$, as there is a free energy barrier to its moving in either direction.

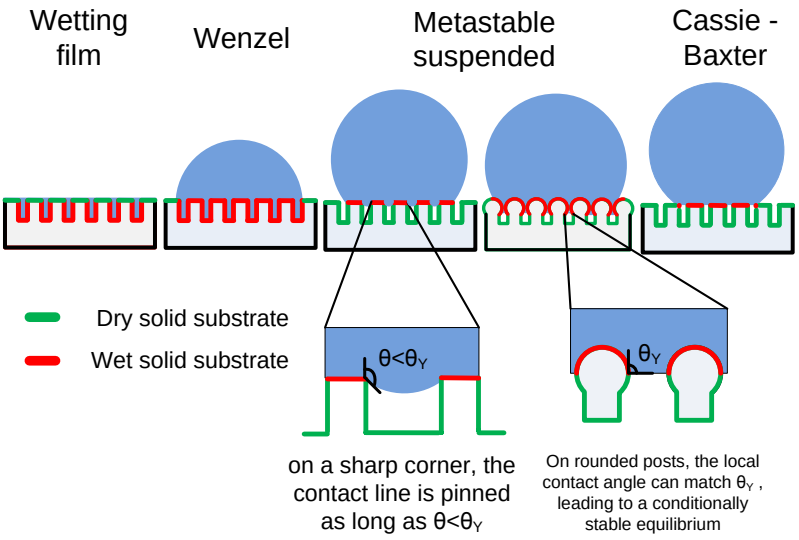


Figure 2.6: Sketch of the possible equilibrium positions for a droplet on a textured surface. The insertion shows a magnification of the idealised liquid - gas interface for the metastable configurations. Green lines represents the dry portion of the substrate, while red lines represent the wetted part.

available for a drop on a textured surface, which we will now briefly introduce.

### Wetting film

Let us start from philic materials. We saw in Section 2.4 that, if the spreading parameter $S > 0$, the liquid will wet the solid surface entirely. Since a rough surface offers even more solid substrate per unitary displacement, we expect the spreading condition to be relaxed. Indeed, liquids which would form a finite contact angle on a smooth surface can form a wetting film on a rough surface of the same material. Suppose that the liquid fills the grooves in the texture, while

the top surface is dry ( Fig.2.6, leftmost configuration). We consider a unitary surface at post height, and we denote by $f_s$ the dry fraction of the surface and by $1 - f_s$ the wet one. We also introduce the surface roughness $r$ , a nondimensional quantity defined as the actual area per unit projected area (for a smooth surface, $r = 1$). To find the critical $\theta_Y$ for which the spreading occurs, let's consider the energy change $\delta E$ for an infinitesimal displacement of the contact line $dx$,

$$\delta E = (\gamma_{sl} - \gamma_{sg})\,(r - f_s)\,dx + \gamma_{lg}\,(1 - f_s)\,dx \tag{2.6}$$

If $\delta E < 0$, it will be energetically favourable for the liquid to spread indefinitely. This means spreading occurs if

$$\cos\theta_Y > \frac{1 - f_s}{r - f_s}. \tag{2.7}$$

This condition is indeed intermediate between the one for spreading on smooth surfaces ($S > 0$), and the one for capillary imbibition of a porous medium ($\cos\theta_Y > 0$).

### Wenzel state

The Wenzel state is accessible for both phobic and philic materials, and corresponds to a configuration in which the liquid penetrates into the roughness, while retaining a finite contact angle. Wenzel's seminal paper on wetting on rough surfaces [24] is fundamental in understanding how chemical and physical properties of a solid surface contribute to its wetting behaviour. He observed that a "rough" surface will store more surface energy per unit area rather than a smooth one, and how this will affect its equilibrium contact angle. To see this, let's consider a drop forming a spherical cap, protruding inside the roughness as in Fig.2.6 (Wenzel label), with a yet unknown contact angle $\theta_W$. For an infinitesimal displacement of the contact line, the energy change is:

$$\delta E = (\gamma_{sl} - \gamma_{sg})\,r dx + \gamma_{lg} dx \cos\theta_W. \tag{2.8}$$

Again, by assuming vanishing $\delta E$ for infinitesimal displacements, the Wenzel contact angle $\theta_W$ on a surface of roughness $r$ is

$$\cos\theta_W = r\cos\theta_Y. \tag{2.9}$$

From Eq.2.9 and the previous discussion, it is easy to see that in the Wenzel state roughness always enhances the intrinsic wetting character of the material. Another relevant aspect is that drops in the Wenzel state exhibit a large contact angle hysteresis. As a matter of fact, even though rough hydrophobic materials can exhibit very large Wenzel contact angles, their roll off angle in this configuration will also be very large. This can be intuitively understood by looking at

Fig.2.6: the liquid is intruding in the solid phase, and detaching is energetically expensive, since a new interface needs to be open. A truly superhydrophobic surface will instead exhibit both large static contact angle and small contact angle hysteresis. These properties are shown by liquids in the Cassie-Baxter state, that we discuss in the next section.

### Cassie-Baxter state

We eventually describe the Cassie-Baxter state [25], most commonly associated with the "Lotus effect" superhydrophobicity. In this configuration, the liquid does not wet the substrate entirely, but it is rather suspended on top of the surface roughness, as sketched in Fig.2.6 (rightmost configuration). This reduces the adhesion with the solid phase, and thus ease the roll-off of droplets. The equilibrium contact angle can also be derived quite easily. As a matter of fact, the Cassie-Baxter apparent contact angle $\theta_{CB}$ will be equal to the average between the substrate contact angle $\theta_Y$ and the contact angle with the air trapped between the solid protrusions $\theta_{air} = 180^o$

$$\cos\theta_{CB} = f_{sl}\cos\theta_Y + f_{lg}\cos\pi = f_{sl}\cos\theta_Y - f_{lg}. \tag{2.10}$$

The weights in Eq.2.10 are the fraction of the drop base in contact with the solid substrate $f_{sl}$ and the trapped air $f_{lg}$.

Equation 2.7 gave us a condition for the transition from a Wenzel configuration to complete wetting on a textured surface. We can ask ourselves a similar question in relation to the Wenzel and Cassie-Baxter states: For a given texture and $\theta_Y$, which one is the energetically favourable state? Suppose $\theta_{app}$ is the apparent contact angle on a given substrate, arising either from a Wenzel or Cassie-Baxter configuration. We now displace the interface by an infinitesimal amount $dx$. The energy change for the system, if we are in the Cassie state, is:

$$\delta E_{CB} = (\gamma_{ls} - \gamma_{sg})\, f_{sl} dx + \gamma_{lg} f_{lg} dx + \gamma_{lg} dx \cos\theta_{app}, \tag{2.11}$$

If we instead move the interface by the same distance $dx$ in the Wenzel state , we get the energy change:

$$\delta E_W = (\gamma_{ls} - \gamma_{sg})\, r dx + \gamma_{lg} dx \cos\theta_{app}. \tag{2.12}$$

The Cassie state will therefore be favourable if the relative energy change is smaller than Wenzel's, $\delta E_{CB} < \delta E_W$. We therefore get the condition on the Young contact angle:

$$\cos\theta_Y < \frac{-f_{lg}}{r - f_{sl}}. \tag{2.13}$$

We therefore see how only inherently hydrophobic materials ($\cos\theta_Y < 0$) will have Cassie state as a global energy minimum. This is however not yet the

complete picture. In fact, even though the Wenzel state might be the lowest energy configuration, an energy barrier for the Cassie-to-Wenzel transition might exist (see the metastable states sketched in Fig.2.6). For example, pinning of the interface at the rim of the posts supporting the drop can prevent the transition to the Wenzel state, unless a significant pressure is applied [26, 27]. If the posts have a rounded shape, several equilibrium configuration can be reached, as long as the local contact angle with the side of the protrusion matches the Young contact angle [28]. Eventually, if the surface is patterned with holes, the air trapped in the pockets can prevent the penetration of liquid inside them. As a matter of fact, exploiting such metastable Cassie states to achieve a robust superhydrophobic behaviour is one of the main topics of this thesis, as we will see in Chapters 5 and 6.

# Chapter 3

# Numeric Methods

In this Chapter we will describe the numerical techniques we employed in our research. The complexity of physical phenomena associated with the dynamics of a liquid interface has led us to apply different numerical techniques to different aspects of the problem. These approaches also reflect the collaborations with different research groups during the Ph.D. activity, which allowed me to test state-of-the-art tools in computational fluid dynamics.

## 3.1 Finite elements method

The finite element method (FEM) is a numeric method for solving partial differential equations (PDEs) with widespread applications in physics and engineering. The relevant equations are discretized by projecting the physical fields on a suitable set of basis functions. The number and type of these functions will determine the accuracy of the computation. A detailed description of the FEM is out of the scope of this work. We will however here describe the fundamental steps of the FEM formulation of a partial differential equation. The reader can find further information in [29, 30]. Several software packages provide meshing, solver, assembly and postprocessing algorithms. In this thesis, we used the commercial software COMSOL [30] to carry out our FEM calculations.

We will first introduce the weak formulation of PDEs, which constitutes the starting point for the FEM analysis, considering the simple case of a time-independent problem. Let $\Omega$ be our computation domain, with boundary $\partial\Omega$. We will consider a scalar function $u(\mathbf{x})$, and a partial differential equation we want to solve

$$\begin{cases} Du(\mathbf{x}) = f & \text{on } \Omega \\ R(u(\mathbf{x}), \partial_\alpha u(\mathbf{x})) = 0 & \text{on } \partial\Omega. \end{cases} \tag{3.1}$$

Here $D$ is a differential operator, $\partial_\alpha u(\mathbf{x})$ represent a space derivative of $u$ and $R(u(\mathbf{x}), \partial_\alpha u(\mathbf{x}))$ is a set of boundary conditions. For simplicity, $D$ will involve only derivatives up to second order. We can define a weak formulation of this problem as follows: let us consider a space $V$ of "well-behaved"* functions $[v : \Omega \to \mathbb{R}]$ with a norm defined as

$$(u, v) = \int_\Omega u(\mathbf{x})v(\mathbf{x})\, d\mathbf{x}. \tag{3.2}$$

A function $u \in V$ is a weak solution for Eqs.3.1 if

$$(Du, v) = (f, v) \;\; \forall\, v \;\in V \tag{3.3}$$

The term "weak" comes from the fact that a solution to Eqs.3.1 (a "strong" solution) is also a solution to Eqs.3.3, while the converse is not generally true. For instance, if $u$ is a strong solution to Eqs.3.1, a function that differs from $u$ on a subset of $\Omega$ of zero measure would still be a weak solution, but not a strong one. An advantage of this formulation is that it relaxes the regularity constraints on the solution. We can see this considering a $\nabla^2 u(\mathbf{x})$ term and integrating by part:

$$\left(\nabla^2 u, v\right) = \int_{\partial\Omega} v(\mathbf{x})\mathbf{n} \cdot \nabla u(\mathbf{x}) - \int_\Omega \nabla u(\mathbf{x}) \cdot \nabla v(\mathbf{x})\, d\mathbf{x}. \tag{3.4}$$

The first term on the right side of Eq.3.4 can be discarded by a suitable choice of boundary conditions on $v(\mathbf{x})$, and we therefore see that, in the weak formulation, the only request on $u$ and $v$ is that they have to be continuous and piecewise differentiable.

Another relevant concept we need is that of "basis" for a function space. For a finite dimensional vector space $U$, a basis $B$ is a subset of $U$ such that each element $u \in U$ can be uniquely written as a linear combination of elements in $B$. This concept can be extended to infinitely dimensional spaces, such as a normed function space as $V$. The number of elements in the basis will be infinite, and the linear combination has to be generalized to an infinite sum. In particular, a Schauder basis $B_s$ is a countable subset of $V$ such as every $v \in V$ can be written unequivocally as:

$$v(\mathbf{x}) = \sum_{n\in\mathbb{N}} a_n \phi_n(\mathbf{x}), \;\; \phi_n \in B_s. \tag{3.5}$$

If such a base can be found, we can write $u(\mathbf{x}) = \sum_{i\in\mathbb{N}} u_i \phi_i(\mathbf{x})$, and Eq.3.3 is equivalent to:

$$\sum_{j\in\mathbb{N}} (D\phi_j, \phi_i)\, u_j = (f, \phi_i) \;\; \forall\, i \;\in \mathbb{N}. \tag{3.6}$$

We are now ready to apply the concepts introduced so far to the Finite Element Method.

*A proper definition could be complicated, let us take it as: regular enough to allow the operations involved in the weak formulation Eq.3.3

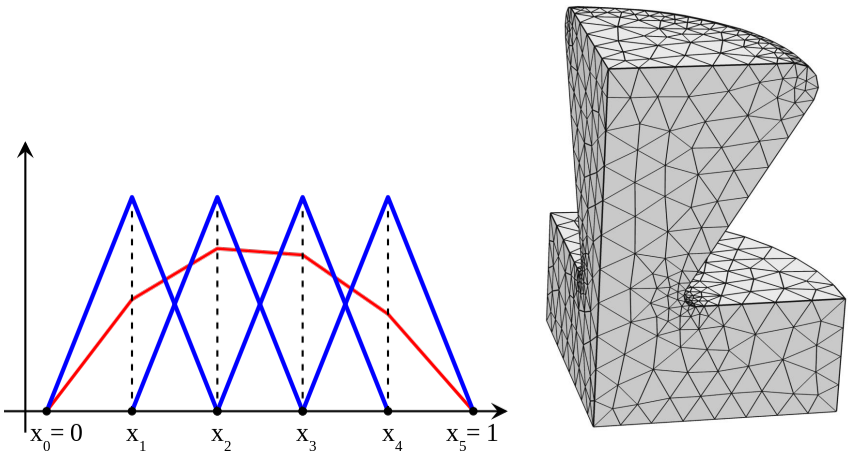


Figure 3.1: Left: A choice of piecewise linear basis functions on a 1D domain (blue lines), and a linear combination of them (red line), which is again piecewise linear. The picture is from Wikipedia [†]. Right: A typical FEM mesh over a three dimensional domain, for linear elasticity analysis.

The idea is to project our solution on a *finite* subset of a basis for V, in order to obtain a finite system of equation we can numerically solve. The first step in defining such basis functions is the choice of a mesh over the computation domain. The computational domain is tasselled with polygons (or polyhedrons in 3D, an example is given in Fig.3.1b), whose size and density can be tuned to provide fine resolution in relevant regions of the domain and a coarser discretization in the remaining part. The basis functions are then chosen to be spatially localized polynomials, with a support limited to a few mesh elements. This means that the overlap between basis functions will be small, and results in sparse matrices, which are relatively easy to handle. The accuracy of a simulation can therefore be tuned in two ways: either by selecting a finer mesh or by switching to higher polynomials over each element. The polynomial degree of the basis functions also has to match at least the highest derivative acting on them in the weak formulation of the problem. In order for our solution to be actually contained in the function space V, it is important to have a general understanding of the physics we want to simulate. For example, exponential variations over small length scales will be poorly resolved as a combination of piecewise linear functions over mesh elements of the same characteristic size. It is therefore worth noticing once more the importance of a careful discretization. Once we have a finite basis, the solution $u(\mathbf{x})$ can be expressed as:

$$u(\mathbf{x}) = \sum_{i=1...N} u_i \, \phi_i(\mathbf{x}), \tag{3.7}$$

[†]http : //en.wikipedia.org/wiki/Finite_element_method

where N is the number of basis functions we include in our simulation. If we now project Eqs.3.1 on this set of functions, we get the Galerkin formulation:

$$\mathbf{A}\mathbf{u} = \mathbf{f}, \tag{3.8}$$

where $\mathbf{u} = \{u_1 \cdots u_N\}$ is the solution vector of length N we solve for, $\mathbf{f}$ is the N-vector of components $f_i = (f, \phi_i)$ storing information about the forcing terms of the PDE and $\mathbf{A}$ is a NxN matrix of entries $A_{ij} = (D\phi_i, \phi_j)$. We have thus converted our initial set of continuous PDE into a discrete linear equation system. In order to achieve the necessary accuracy, the resulting matrix can be very large. However, thanks to the choice of local support for the basis functions, most element of the matrix will be zero. Solving such a linear system can be significantly faster that conventional matrix inversion, and less memory intensive, since only nonzero matrix elements and their location need to be stored.

## 3.2 Lattice Boltzmann method

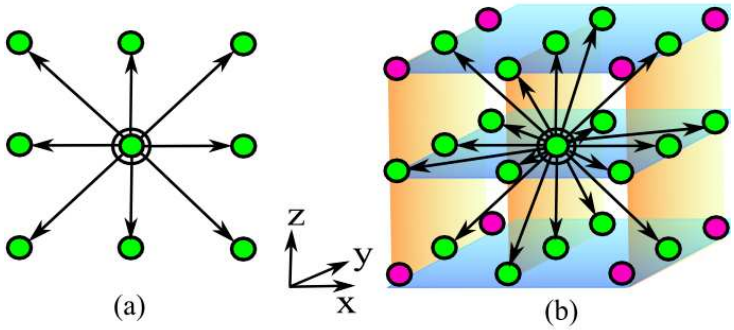


Figure 3.2: The vector sets $\vec{e}_i$ for two different lattices a) the 2D9 scheme on a square lattice. b) the 3D19 scheme on a cubic lattice. Purple sites are not directly connected to the central one. Picture reproduced with permission from Blow [31].

Lattice Boltzmann (LB) methods are a family of algorithms which are gaining increasing popularity in fluid dynamics simulations involving complex fluids and interfaces. This numerical scheme solves a discrete Boltzmann equation through a simple evolution step, consisting of a streaming phase and a collision term. Let us consider a lattice of points $\vec{x}$, connected by $i$ lattice vectors $\mathbf{e_i}$ (typical lattices are shown in Fig.3.2). A distribution function $f_i$ is associated to each vector $\mathbf{e_i}$. The distribution functions are related to the fluid density $\rho$ and momentum $\rho\mathbf{u}$ through

$$\rho = \sum_i f_i, \ \rho u_\alpha = \sum_i f_i e_{i\alpha}, \tag{3.9}$$

where $e_{i\alpha}$ are the Cartesian coordinates of the lattice vectors $\mathbf{e_i}$ (Greek letters are used to indicate Cartesian directions). We could say that each $f_i$ represents the density of fluid flowing along each lattice direction. The collision and streaming steps are then respectively:

$$\begin{aligned} f_i^*(\vec{x},t) &= f_i(\vec{x},t) - \frac{f_i(\vec{x},t) - f_i^0(\vec{x},t)}{\tau}, \\ f_i(\vec{x}+\vec{e}_i\Delta t, t+\Delta t) &= f_i^*(\vec{x},t). \end{aligned} \tag{3.10}$$

where $\Delta t$ is the discrete time step, $\tau$ a relaxation time and $\left\{f_i^0\right\}$ are a set of equilibrium distribution function -not yet specified- towards which each $f_i$ relaxes. What is required now is a connection between the simple dynamics of Eq.3.10 and the physics of the fluid system, described by the continuity and Navier-Stokes equations:

$$\partial_t \rho + \partial_\alpha(\rho u_\alpha) = 0, \tag{3.11}$$

$$\begin{aligned} \partial_t(\rho u_\alpha) + \partial_\beta(\rho u_\alpha u_\beta) &= -\partial_\beta P_{\alpha\beta} + \\ &+ \partial_\beta\left(\rho\mu\left[\partial_\beta u_\alpha + \partial_\alpha u_\beta\right] + \rho\lambda\delta_{\alpha\beta}\partial_\gamma u_\gamma\right), \end{aligned} \tag{3.12}$$

where $u_\alpha, u_\beta$ are the fluid velocity components, $\mu$ and $\lambda$ are the dynamic and second viscosities, and $P_{\alpha\beta}$ is the pressure tensor. $\partial_t$ represents a time derivative and $\partial_\alpha$, $\partial_\beta$ spatial derivatives (Einstein summation convention is assumed).

The fluid physics can indeed be recovered by a suitable choice of the equilibrium distribution functions $\left\{f_i^0\right\}$.

First of all, the conservation of mass and momentum imposes a first set of constraints on the choices for $f_i^0$. By considering the definitions in Eq.3.9, the following conditions need to apply to the zeroth and first momentum of $f_i^0$:

$$\sum_i f_i^0 = \rho, \ \sum_i f_i^0 e_{i\alpha} = \rho u_\alpha. \tag{3.13}$$

In order to get the fluid dynamics described by Eqs.3.11 and 3.12, it can be shown [32] that we also have to fix the second momentum of $f_i^0$ as

$$\sum_i f_i^0 e_{i\alpha} e_{i\beta} = P_{\alpha\beta} + \rho u_\alpha u_\beta. \tag{3.14}$$

We can now check that condition 3.13 is sufficient to recover the continuity equation for incompressible fluids. By Taylor expanding Eqs.3.10 in the left-hand side we get

$$-\frac{f_i - f_i^0}{\tau} = \sum_{k=1}^{\infty} \frac{1}{k!}\Delta t^k \left(\partial_t + e_{i\alpha}\partial_\alpha\right)^k f_i. \tag{3.15}$$

This equation can be solved recursively by the method of successive approximations. We retain terms to $O\left(\Delta t^2\right)$ and we get:

$$-\frac{f_i - f_i^0}{\tau\Delta t} = \left(\partial_t + e_{i\alpha}\partial_\alpha\right) f_i^0 - (\tau - 1/2)\,\Delta t\left(\partial_t^2 + 2e_{i\alpha}\partial_t\partial_\alpha + e_{i\alpha}e_{i\beta}\partial_\alpha\partial_\beta\right) f_i^0 + O\left(\Delta t^2\right). \tag{3.16}$$

By summing over $i$ Eq.3.16 and remembering Eqs.3.9 and 3.13, we get:

$$\begin{aligned} 0 &= \partial_t \rho + \partial_\alpha (\rho u_\alpha) \\ &- (\tau - 1/2)\,\Delta t \left\{ \partial_t^2 \rho + 2\partial_t \partial_\alpha (\rho u_\alpha) + \partial_\alpha \partial_\beta \sum_i f_i^0 e_{i\alpha} e_{i\beta} \right\} + O\left(\Delta t^2\right) \\ &\rightarrow 0 = \partial_t \rho + \partial_\alpha (\rho u_\alpha) + O(\Delta t)\,. \end{aligned} \tag{3.17}$$

Similarly, multiplying Eq.3.16 by $e_{i\beta}$ and summing over $i$ we have:

$$\begin{aligned} 0 &= \partial_t (\rho u_\alpha) + \partial_\alpha \sum_i f_i^0 e_{i\alpha} e_{i\beta} \\ &- (\tau - 1/2)\,\Delta t \left\{ \partial_t^2 (\rho u_\alpha) + 2\partial_t \partial_\alpha \sum_i f_i^0 e_{i\alpha} e_{i\beta} + \partial_\alpha \partial_\beta \sum_i f_i^0 e_{i\alpha} e_{i\beta} e_{i\gamma} \right\} + O\left(\Delta t^2\right). \\ &\rightarrow 0 = \partial_t (\rho u_\alpha) + \partial_\alpha \sum_i f_i^0 e_{i\alpha} e_{i\beta} + O(\Delta t)\,. \end{aligned} \tag{3.18}$$

By substituting the final expressions in Eqs.3.17 and 3.18 in the curly brackets of Eq.3.17, we see that Eq.3.10 indeed satisfies the continuity equation to second order in $\Delta t$. An analogous, although lengthy, procedure would recover the Navier-Stokes equation to the second order in $\Delta t$. Details on this procedure can be found for example in the paper by Swift et al. [32]. It is worth noticing that Eqs.3.13 and 3.14 do not uniquely define the basis functions $\left\{f_i^0\right\}$. By careful consideration, it is then possible to choose them to also minimize the appearance of spurious velocities in the system [31]. The equilibrium distributions $\left\{f_i^0\right\}$ are in practice chosen to be polynomial expansion in $\mathbf{u}$, with suitable coefficients that satisfy the aforementioned constraints.

The LB method has some interesting advantages over other CFD approaches. Its advection step is very simple, reducing the associated computational effort for each node. Its local nature is well-suited for parallelization, and the mesoscopic model it relies on make it easy to include thermodynamic quantities. A significant limitation, at least in most current implementations, is the use of a fixed grid, which makes curved boundaries difficult to handle.

## 3.3 Surface Evolver

It is sometimes convenient to forget about the dynamics of the liquid-air interface, and focus on its equilibrium configurations. This approach has been useful, for example, when evaluating the stability of a suspended Cassie-Baxter configuration upon applied pressure in Chapter 6.

A useful tool for this kind of analysis is Surface Evolver (SE) [33], a free software for the simulation of drops and interfaces. The interface is described by a triangular mesh, which can be refined and relaxed according to an energy

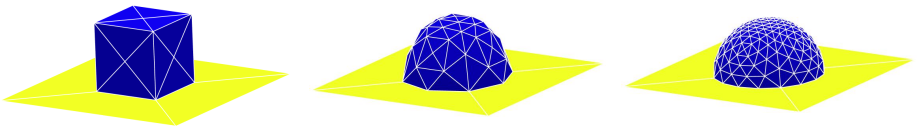

Figure 3.3: Relaxation of a liquid drop on a flat surface using Surface Evolver, for $\theta_Y = 90^o$. At every iteration, the surface mesh was refined and the vertex position relaxed with a gradient descent algorithm that minimizes surface energy.

functional. Solid walls can also be included in the simulation by constraining the motion of boundary vertices to a given surface. Since the evolution is generated with a gradient-descent algorithm, the transient dynamics of the simulation does not include inertial effects. However, the equilibria found this way coincide with the physical ones.

The total energy G of a liquid-air system can be expressed as:

$$G = \gamma_{ls} A_{ls} + \gamma_{lg} A_{lg} + \gamma_{sg} A_{sg} + PV, \tag{3.19}$$

Here V is the volume of the liquid phase, P the pressure difference across the interface, while ($\gamma_{ls}$, $\gamma_{lg}$, $\gamma_{sg}$) and ($A_{ls}$, $A_{lg}$, $A_{sg}$) are the surface tensions and contact surfaces per unit cell between liquid and solid phase, liquid and gas phase, solid and gas phase respectively. Since the solid area in the domain has a finite extent, we can introduce its value $A_{tot}$, so that: $A_{sg} = A_{tot} - A_{ls}$. Constant terms in the energy expression will not contribute to the minimization, so we can discard $A_{tot}$. Remembering the definition of Young contact angle $\cos\theta_Y = \frac{\gamma_{sg} - \gamma_{sl}}{\gamma_{lg}}$, we can then re-arrange the energy expression as:

$$G = \gamma_{lg}[A_{lg} - \cos\theta_Y A_{ls}] + PV. \tag{3.20}$$

We can see that liquid-air and liquid-solid interfaces appear with different weights, the latter being positive or negative according to the Young contact angle. It can also be seen that the solid-air interface does not appear explicitly in the relation, and therefore the liquid meniscus can be modelled taking into account only $A_{gl}$ and $A_{ls}$. Surface Evolver describes $A_{gl}$, $A_{ls}$ and V in terms of the triangular mesh. Each vertex in the simulation is then acted upon by a force depending on how much its displacement affects the surface area or the liquid volume. Details on the implementation can be found in the software manual [33]. A typical Surface Evolver setup is shown in Fig.3.3.

## 3.4 Finite difference scheme for Navier-Stokes equations on a staggered grid

We eventually describe a finite difference scheme to solve the continuity and Navier-Stokes equations, which we employed in Chapter 8.

Finite difference schemes are rather intuitive. The computation domain is discretized with some regular grid, and the relevant derivatives appearing in the PDEs are expressed in terms of finite differences among the values of the physical fields at grid nodes. The equations to be discretized are the continuity and Navier-Stokes equations for incompressible fluids:

$$\nabla \cdot \mathbf{u} = 0 \tag{3.21}$$

$$\frac{\mathrm{d}\mathbf{u}}{\mathrm{d}t} + \mathbf{u} \cdot \nabla \mathbf{u} \;=\; \frac{1}{\rho}\left(-\nabla \mathrm{p} + \mu \nabla^2 \mathbf{u}\right). \tag{3.22}$$

As usual, $\mathbf{u}$ is the velocity field, $\mu$ the dynamic viscosity, $\rho$ the fluid density and p the pressure. A simple Euler time step for the momentum equation would then look like:

$$\mathbf{u}^{n+1} = \mathbf{u}^n + \Delta t \left( f(\mathbf{u}^n) - \frac{1}{\rho}\nabla \mathrm{p}, \right) \tag{3.23}$$

where we collected as $f(\mathbf{u}^n)$ all the contributions to velocity from Eq.3.22 which are independent of p. In order to satisfy the continuity equation Eq.3.21, let's split the step in two parts:

$$\begin{aligned} \mathbf{u}^* &= \mathbf{u}^n + \Delta t f(\mathbf{u}^n) \\ \mathbf{u}^{n+1} &= \mathbf{u}^* - \frac{\Delta t}{\rho}\nabla \mathrm{p} \end{aligned} \tag{3.24}$$

We then take the divergence of the second of Eqs.3.24, which has to be equal to zero to enforce the mass conservation. This leads to a Poisson equation for the pressure:

$$\nabla \cdot \mathbf{u}^{n+1} = \frac{\rho}{\Delta t}\nabla \cdot \mathbf{u}^* - \nabla^2 \mathrm{p} = 0 \tag{3.25}$$

Which can be solved iteratively. This part of the scheme can be rather time consuming, so different tools, such as multigrid algorithms [34], can be applied to speed up the process.

We eventually need to choose a suitable discretization for the space derivatives in Eq.3.22. It would be tempting to use the same grid for the fields $\mathbf{u} = \{u, v\}$ and p, so that the second of Eqs.3.24 would be approximated as:

$$u_{ij}^{n+1} = u_{ij}^* - \frac{\Delta t}{\rho}\frac{\mathrm{p}_{i+1j} - \mathrm{p}_{i-1j}}{2\Delta x} \tag{3.26}$$

$$v_{ij}^{n+1} = v_{ij}^* - \frac{\Delta t}{\rho}\frac{\mathrm{p}_{ij+1} - \mathrm{p}_{ij-1}}{2\Delta y}. \tag{3.27}$$

It is easy to check that, with such a discretization, there are choices $\mathrm{p} \neq \text{const}$ for which $\mathrm{p}_{i+1j} - \mathrm{p}_{i-1j} = 0$ and $\mathrm{p}_{ij+1} - \mathrm{p}_{ij-1} = 0$. For instance, with reference to Fig.3.4, we can chose a pressure field with values $\mathrm{p} = c_1, c_2, c_3, c_4$ on sites labelled respectively by $\square, \triangle, \circ, \times$, and still obtain zero central finite differences for p. This means that there are different choices for the pressure field that would lead

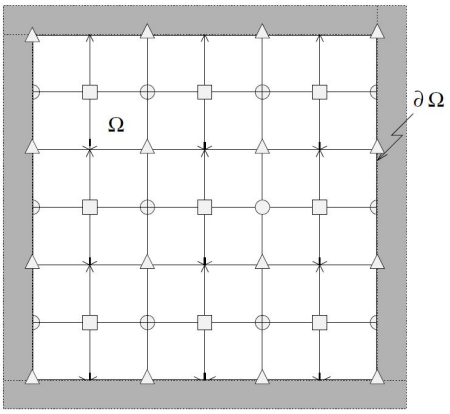


Figure 3.4: An example of a pressure check-board pattern. By using a simple central finite difference stencil, the pressure field would be defined up to four constant on each of the sites $\square, \triangle, \circ, \times$. This sketch is from [35].

to the same discrete momentum equation, affecting the stability of the solution. A staggered grid as the one depicted in Fig.3.5 avoids this issue. In this case, the horizontal velocities are defined at the midpoints of the left and right edges of each cell, the vertical velocities at the midpoints of the top and bottom edges, and the pressures in the centre of each cell. By choosing the discretization:

$$u^{n+1}_{i+\frac{1}{2}j} = u^{*}_{i+\frac{1}{2}j} - \frac{\Delta t}{\rho}\frac{\mathrm{p}_{i+1j} - \mathrm{p}_{ij}}{\Delta x} \tag{3.28}$$

$$v^{n+1}_{ij+\frac{1}{2}} = v^{*}_{ij+\frac{1}{2}} - \frac{\Delta t}{\rho}\frac{\mathrm{p}_{ij+1} - \mathrm{p}_{ij}}{\Delta y}, \tag{3.29}$$

we have that the discrete gradient of the pressure is zero iff p = const.

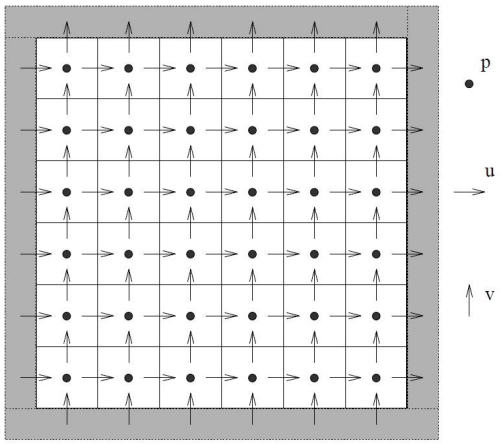


Figure 3.5: The staggered grid employed to avoid the checkboard pressure, from [35].

In the next Chapter, we will discuss how such a finite difference scheme can be coupled to a tracker particles algorithm to describe a sharp interface between two phases.

## 3.5 Topology optimization

Topology optimization [36] is an optimization method with no intrinsic constraint on the topology of the solution, which has been applied in many different fields such as structural mechanics [36], photonic crystal design [37] and microfluidic devices [38]. The general question answered by this numeric approach is: "How to distribute material in a domain to achieve the optimal structure for a given task?". The advantage of topology optimization, if compared to other relevant optimization algorithms, is that the topology of the solution is not fixed a priori, i.e. holes can in principle appear and disappear throughout the optimization steps. Let us introduce a few relevant quantities: $\chi(\mathbf{x})$ is the design variable, a continuous field over the domain describing the distribution of material. Its values range from 0 (empty region) to 1 (solid region). Let $u(\mathbf{x};\chi)$ be the relevant physical parameter in the optimization procedure (a scalar field, for simplicity), defined over the optimization domain $\Omega$. We eventually define the objective function $\phi\left(u(\chi),\chi\right)$ as a scalar quantity (typically an integral over the simulation domain) which has to be minimized by the optimal material distribution. Different kind of constraints can also be included, the most common being a upper or lower bound on the amount of material available in the optimization. Here we restrict ourselves to a minimal set of conditions, that are however descriptive of the general Topology Optimization procedure. The optimality problem can therefore be formulated as follows:

$$\left.\begin{aligned} \min_{\chi} &: \phi\left(u(\chi),\chi\right) = \int_{\Omega} f\left(u(\chi),\chi\right)\ \mathrm{dV} \\ s.t.\ &: \int_{\Omega} \chi(\mathbf{x})\ \mathrm{dV} \leq V_0 \\ &: L(u(\chi),\chi) = 0 \\ &: 0 \leq \chi(\mathbf{x}) \leq 1\ \forall \mathbf{x} \text{ in } \Omega. \end{aligned}\right\} \tag{3.30}$$

The first condition in Eqs.3.30 represents a constraint on the total amount of "material" available for the optimization. The condition $L(u(\chi),\chi) = 0$ is typically some kind of PDE that the physical field $u(\mathbf{x};\chi)$ must satisfy during the optimization. Eventually, the design variable is bounded, so $0 \leq \chi(\mathbf{x}) \leq 1$. A practical implementation of this optimality problem requires a discretization of the fields $u(\mathbf{x})$ and $\chi(\mathbf{x})$. At the core of the optimization process lies the calculation of the sensitivity

$$\frac{\mathrm{d}}{\mathrm{d}\chi}\Phi(u(\chi),\chi) \;=\; \frac{\partial\Phi}{\partial\chi} + \frac{\partial\Phi}{\partial u}\frac{\partial u}{\partial\chi}, \tag{3.31}$$

i.e. the derivative of the objective function with respect to the design variable, which provides fundamental information for the optimization algorithm. While the explicit derivative $\frac{\partial \Phi}{\partial \chi}$ in Eq.3.31 is generally simple to evaluate, it would be very complicated to evaluate the non-explicit dependence $\frac{\partial u}{\partial \chi}$ of the physical parameter on the design variable . An effective solution to this complication is the Adjoint Method, that we now briefly describe. By exploiting the condition $L(u(\chi), \chi) = 0$ we rewrite Eq.3.31 as:

$$\begin{aligned} \frac{\mathrm{d}}{\mathrm{d}\chi}\Phi(u(\chi),\chi) &= \frac{\partial \Phi}{\partial \chi} + \frac{\partial \Phi}{\partial u}\frac{\partial u}{\partial \chi} + \tilde{u}\frac{\mathrm{d}}{\mathrm{d}\chi}L(u(\chi),\chi) \\ &= \frac{\partial \Phi}{\partial \chi} + \frac{\partial \Phi}{\partial u}\frac{\partial u}{\partial \chi} + \tilde{u}\left[\frac{\partial L}{\partial \chi} + \frac{\partial L}{\partial u}\frac{\partial u}{\partial \chi}\right] \\ &= \frac{\partial \Phi}{\partial \chi} + \tilde{u}\frac{\partial L}{\partial \chi} + \frac{\partial u}{\partial \chi}\left[\frac{\partial \Phi}{\partial u} + \tilde{u}\frac{\partial L}{\partial u}\right]. \end{aligned} \tag{3.32}$$

The first two derivatives on the right side of Eq.3.32 are now simple to evaluate. On the other hand, the terms between brackets can be discarded by choosing $\tilde{u}$ so that $\frac{\partial \Phi}{\partial u} + \tilde{u}\frac{\partial L}{\partial u} = 0$. Thus, for any number of design variables (that is, for any resolution in the material distribution), the evaluation of the sensitivity can be reduced to solving one physics problem $L(u(\chi), \chi) = 0$ and one adjoint equation $\frac{\partial \Phi}{\partial u} + \tilde{u}\frac{\partial L}{\partial u} = 0$. The actual implementation of the optimization step in the algorithm is carried out with the Method of Moving Asimptotes (MMA) [39].

### 3.5.1 Minimal energy dissipation in Stokes flow

As an example of Topology Optimization applied to flow situations, we will find the distribution of material that minimizes viscous energy dissipation in a two dimensional Stokes flow. In continuity with the definitions introduced in the previous section, we have the following formulation:

$$\left.\begin{aligned} &\min_{\chi} : \phi\left(\mathbf{u}(\chi),\chi\right) = \int_{\Omega} \frac{1}{2}\mu \sum_{i,j}\left(\frac{\partial u_i}{\partial x_j} + \frac{\partial u_j}{\partial x_i}\right)^2 + \sum_i \alpha(\chi) u_i^2 \,\mathrm{dV} \\ &s.t. : \int_{\Omega} \chi(\mathbf{x})\,\mathrm{dV} \geq V_0 \\ &\quad : -\nabla P + \mu\nabla^2\mathbf{u} - \alpha(\chi)\mathbf{u} = 0 \\ &\quad : 0 \leq \chi(\mathbf{x}) \leq 1 \;\forall \mathbf{x} \text{ in } \Omega. \end{aligned}\right\} \tag{3.33}$$

The continuous distribution of material described by $\chi$ affects the Stokes equation as a porous medium, that dampen and control the fluid flow. This specific coupling represents exactly empty regions, while solid features are approximately represented by "very low porosity" areas. In principle, the optimal material distribution could be a continuously varying field $\chi(\mathbf{x})$, representing regions with

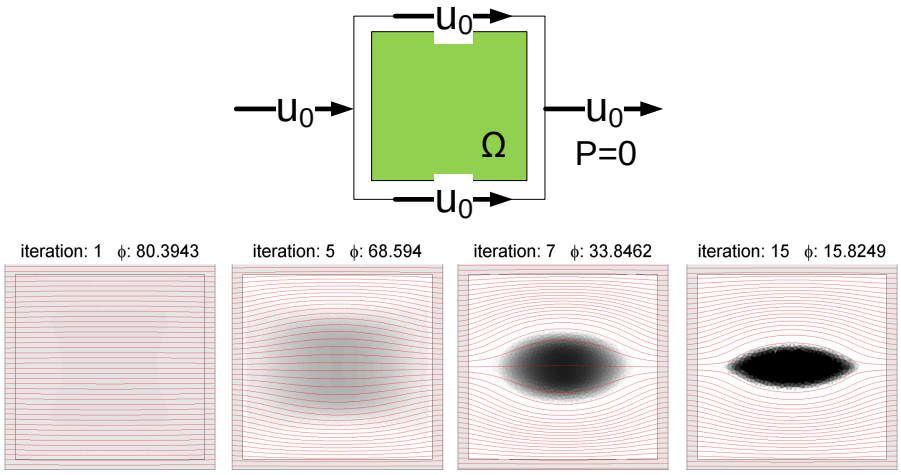


Figure 3.6: Top: Domain and boundary conditions for the energy dissipation optimization example. The green field is the Topology Optimization domain $\Omega$. Bottom: selected iterations in the optimization procedure, and value of the objective function $\phi$. Streamlines are in red, and $\chi(\mathbf{x})$ is shown in greyscale (black corresponds to solid).

more or less porous obstacles. However, it is often desirable to avoid intermediate values of $\chi$ in the solution, since a binary solid/empty structure is easier to realize experimentally. This can be achieved enveloping $\chi$ with a convex function $\alpha(\chi) = \alpha_{max} - \frac{(\alpha_{max})\cdot q\cdot(1-\chi)}{(q+\chi)}$. In this way, only values close to the maximum $\chi = 1$ will significantly affect the flow, and the volume constraints will contribute to focusing the material in localized areas.

The flow is driven by a prescribed velocity $\mathbf{u}_0$ on all boundaries. The design variable is initialised $\chi(\mathbf{x}) = V_0$ over the whole domain. In Fig.4.1, we show a few relevant iterations in the optimization routine. The "porous material" inside the domain, initially distributed homogeneously, is progressively collected and localized in the centre of the simulation box, resulting in an obstacle that distort the fluid flow. The shape is then smoothed to minimize the viscous drag, and we are eventually left with a "rugby ball" shape, which is reminiscent of an airfoil profile. The main difference is the left-right symmetry of the structure, which is a consequence of the time reversal properties of the low Reynolds number Stokes equation if compared to the full Navier-Stokes equation.

# Chapter 4

# Interface Models

In the previous Chapter we introduced numeric tools which are relevant to solve a variety of partial differential equations. In this Chapter we will instead focus on the specific modelling required to describe the liquid-air interface. Models for a two-phase system can be broadly classified in two families: Sharp interface models [40] and diffuse interface models [41]. Both approaches are characterized by strengths and weaknesses. Sharp interface methods describe the liquid-air interface as some well-defined boundary, usually in terms of a mesh, or a set of tracker particles, whose position can be interpolated to recover the interface shape. The main advantage of this approach is a direct parametrization of the interface, which allows to compute geometric properties in a straightforward way. However, extra effort is required when topological changes occur (drops merging or splitting, for instance), since the connectivity of the interface markers has to be modified. This is often performed in an *ad hoc* way [42]. Moreover, it is well known that a stress singularity arises at a sharp contact line sliding on a substrate where a no-slip velocity boundary condition is enforced [43]. This issue can be solved by allowing a finite slip velocity in a small region close to the contact line, and subsequently matching the solution near the contact line with the one in the "bulk" of the drop. The size of such slide region is however difficult to establish, and the whole procedure quite cumbersome.

On the other hand, diffuse interface methods describe the liquid-air interface as a smooth transition in some field defined across the two phases. The interface position is therefore implicitly determined by the thermodynamic properties of the fluid. This makes it easier to handle topological changes [44]. Diffuse models can also be seen as a solution to the stress singularity at the contact line we discussed before. As a matter of fact, even if a no-slip boundary condition is applied, the interface can move in a diffusive way [41], due to local flows induced by the gradients at the finite width interface.

We will also consider a third approach, namely solving only the Young-Laplace equation, which describes the equilibrium shape of a liquid-air interface for a given pressure difference across it. This latter model derives from an energy minimization principle, and does not account for transient effects. This is certainly an approximation of the system, but it proves convenient as a modelling tool for numeric optimization purposes. In such a context, a physical model has to be solved several time to test the performance of different geometries. It is therefore fundamental to describe the system in terms of a computationally affordable model.

## 4.1 Front-Tracker method for sharp interface modelling

We now describe an example of a wide family of Lagrangian methods to track the position of a liquid-gas interface [40]. We combine this approach to the finite difference scheme described in the previous Chapter, in a method called Marker and Cell (MAC) [45]. We will consider an axisymmetric setup with two fluids, so that the interface location can be described in terms of a parametric curve $\mathbf{b}(s) = \{r(s), z(s)\}$. The curve $\mathbf{b}(s)$ is supposed to meet the coordinate axes in two distinct points, and is oriented from its highest-$z(s)$ to its lowest-$z(s)$ intersection. The basic idea is to follow the interface position through fictitious marker particles, which are convected by the fluid flow. At every time step, the particles positions are used to define the interface location through an interpolation scheme. A typical choice is a cubic spline interpolation, which has the required smoothness to evaluate first and second order derivatives of the interface shape. The trackers are re-distributed at every time step along the spline curve in order to avoid clustering.

It is clear that the most delicate step in a numeric implementation of this scheme is calculating the intersection between the spline $\mathbf{b}(s)$ and the numeric grid over which the fluid variables (velocity and pressure) are defined. Once we have this information, it is simple to recover the surface tension force acting on each grid cell, as we will now show. The surface force can be included in the Navier-Stokes equations as a term $\mathbf{f_s}$:

$$\mathbf{f_s}(\mathbf{x}) = \delta_{\mathbf{b}}(\mathbf{x} - \mathbf{b}(s))\gamma\kappa\mathbf{n}, \tag{4.1}$$

where $\delta_{\mathbf{b}}(\mathbf{x})$ is a two dimensional delta function with support on $\mathbf{b}(s)$, $\gamma$ is the surface tension, $\kappa$ the curvature of the interface and $\mathbf{n}$ the normal vector to the interface. For an axisymmetric geometry, the mean curvature can be conveniently expressed as

$$\kappa\mathbf{n} = \kappa_{axi}\mathbf{n} + \frac{\mathrm{d}\mathbf{t}}{\mathrm{d}s}, \tag{4.2}$$

where $\kappa_{axi} = \frac{1}{r}\frac{\mathrm{d}z}{\mathrm{d}s}$ represents the curvature with respect to the symmetry axis, $\mathbf{t}$ is the unitary tangent vector to the interface and $\frac{\mathrm{d}\mathbf{t}}{\mathrm{d}s}$ is the curvature in the

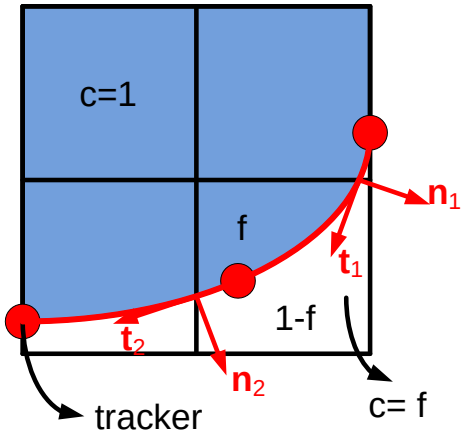


Figure 4.1: Sketch of the relevant quantities in a marker and cell method. The tangent and normal vectors to the interface are computed at the boundaries of each cell to calculate the surface force acting on it. The density and viscosity for cells which are occupied by both fluids are evaluated by a weighted average, with the fractions $\{f, 1-f\}$ occupied by phase 1 and 2 as weights.

radial plane. The force $F_{ij}$ acting on the grid cell of indexes (i,j) is then obtained integrating:

$$\begin{aligned} F_{ij} &= \iint_{\text{cell}} \mathbf{f_S}\, \mathrm{dA} \\ &= \iint_{\text{cell}} \delta_{\mathbf{b}} \gamma \kappa \mathbf{n}\, \mathrm{dA} \\ &= \gamma \int_{s_1}^{s_2} \frac{\mathrm{d}\mathbf{t}}{\mathrm{d}s} + \kappa_{axi}\mathbf{n}\, \mathrm{ds} \\ &= \gamma \left[ (\mathbf{t}(s_2) - \mathbf{t}(s_1)) + \frac{1}{r}\int_{s_1}^{s_2} \frac{\mathrm{d}z}{\mathrm{d}s}\mathbf{n}\, \mathrm{ds} \right] \end{aligned} \tag{4.3}$$

In the previous derivation, $s_1$ and $s_2$ are the values of the archlength when the splines intersects the bounds of cell (i,j). The density $\rho$ and viscosity $\mu$ of the two phases can be interpolated across the interface through a "colour" field $c(\mathbf{x})$, defined as

$$c(\mathbf{x}) = \begin{cases} 0 & \text{if outside } \mathbf{b}(s) \\ 1 & \text{if inside } \mathbf{b}(s) \\ f & \text{if } \mathbf{b}(s) \text{ crosses the cell ,} \end{cases} \tag{4.4}$$

where f is the fraction of the cell volume delimited by $\mathbf{b}(s)$, which can be computed once $\mathbf{b}(s_1)$, $\mathbf{b}(s_2)$ are known. A simple interpolation then leads to:

$$\rho = c\rho_1 + (1-c)\,\rho_2 \tag{4.5}$$

$$\mu = c\mu_1 + (1-c)\,\mu_2. \tag{4.6}$$

## 4.2 Cahn-Hilliard diffuse interface model

We will now describe the Cahn-Hilliard model for two-phase systems [46]. In this approach, the interface description is not explicit, but arises as a part of a thermodynamic model, which describes two immiscible phases. The thermodynamic state of the fluid is described at every point $\mathbf{x}$ and time $t$ by its density $\rho(\mathbf{x}, t)$. The free energy of the system, $\Psi$, is taken as a Landau double-well potential with the addition of a derivative term representing the surface tension, and a surface contribution of the form proposed by Cahn [47]:

$$\Psi = \iiint_D \left( \psi_b(\rho) - \mu_b \rho + \frac{1}{2}\kappa |\nabla \rho|^2 \right) dV - \iint_{\partial D} \mu_s \rho \, dS. \tag{4.7}$$

The first term in the integrand of Eq.4.7 is the bulk free energy density [48]

$$\psi_b(\rho) = p_c \left[ \left( \nu^2 - \beta\tau_W \right)^2 - (1 - \beta\tau_W)^2 \right]. \tag{4.8}$$

where $\rho_c$ , $p_c$ , $\tau_W$ and $\beta$ are, respectively, the critical density, critical pressure, reduced temperature and a free parameter controlling the density difference between phases, while $\nu = \frac{\rho - \rho_c}{\rho_c}$ is a normalised density. This potential leads to two equilibrium bulk densities $\rho_e = \rho_c \left(1 \pm \sqrt{\beta\tau_W}\right)$. the term $\mu_b$ in Eq.4.7 is a Lagrange multiplier constraining the total mass of fluid, while the third term is an interface energy cost, tunable through the parameter $\kappa$, associated with density gradients. It can be seen that a minimum energy configuration for the system is given by a bulk region for each phase, with a diffuse interface between them, with surface tension $\gamma$ and width $\xi$ [48]:

$$\gamma = \frac{4}{3}\rho_c \sqrt{2\kappa p_c (\beta\tau_W)^3}, \; \xi = \frac{1}{2}\rho_c \sqrt{\frac{\kappa}{\beta\tau_W p_c}}. \tag{4.9}$$

The final term in Eq.4.7 is the solid surface contribution to the free energy $\Psi$. When $\Psi$ is minimised this gives the boundary condition $\partial_\perp \rho = -\mu_s/\kappa$ which fixes the value of the density at the substrate. The contact angle $\theta$ at the surface is related to the surface chemical potential by [48]

$$\mu_s = 2\beta\tau_W \sqrt{2p_c\kappa}\, \text{sign}\left(\frac{\pi}{2} - \theta\right) \sqrt{\cos\frac{\alpha}{3}\left(1 - \cos\frac{\alpha}{3}\right)},$$
$$\alpha = \arccos(\sin^2\theta). \tag{4.10}$$

The connection between the thermodynamic and fluid dynamic of the system arises through the pressure tensor $P_{\alpha\beta}$ derived from the free energy expression Eq. 4.7 [41]:

$$P_{\alpha\beta} = \left( p_b - \frac{1}{2}\kappa \partial_\gamma \rho \partial_\gamma \rho - \kappa\rho\partial_{\gamma\gamma}\rho \right) \delta_{\alpha\beta} + \kappa \partial_\alpha \rho \partial_\beta \rho, \tag{4.11}$$

where $p_b$ is the bulk pressure defined as:

$$p_b = p_c \left(\nu^2 + 1\right) \left(3\nu^2 - 2\nu + 1 - 2\beta\tau_W\right). \tag{4.12}$$

In contrast with the MAC method, it can be thus seen that in this case the interface description does not appear explicitly, but is included in a modified pressure term for the Navier-Stokes equations. In terms of implementations, the characteristic interface thickness $\xi$ has to be as small as possible while still assuring numeric stability. This usually means a thickness close to a single mesh/lattice element.

## 4.3 Young-Laplace equation

In the previous sections we described time dependent, fully coupled systems of equations describing the fluid dynamics and the interface motion. These approaches are accurate in terms of physical modelling, but numerically intensive. These considerations suggest that, under opportune circumstances, it might be convenient to focus on a simplified system, and only solve the Young-Laplace equation, namely the deformation of an interface under an applied pressure difference.

We will here use an energy argument to derive a particular formulation of Young-Laplace equation Eq.2.2, which is suitable when the interface can be described as a function $s(x, y)$ over a two dimensional domain. We then have that the volume below the surface $V$ and the interface area $A$ can be described as:

$$V = \int_\Omega s(x, y)\mathrm{d}x\mathrm{d}y, \tag{4.13}$$

$$A = \int_\Omega |\frac{\partial s(x,y)}{\partial x} \times \frac{\partial s(x,y)}{\partial y}|\mathrm{d}x\mathrm{d}y = \int_\Omega \sqrt{1 + \left(\frac{\partial s(x,y)}{\partial x}\right)^2 + \left(\frac{\partial s(x,y)}{\partial y}\right)^2}\mathrm{d}x\mathrm{d}y. \tag{4.14}$$

The energy associated to the liquid-air surface position depends on the displacement of the fluids (through the pressure difference between them $\Delta P$) and the stretching of the interface (through the surface tension $\gamma$). We can therefore define an energy functional

$$E[s] = \int_\Omega \mathcal{L}\left(s, \partial_\alpha s\right) \mathrm{d}x\mathrm{d}y, \tag{4.15}$$

$$\mathcal{L}\left(s, \partial_\alpha s\right) = \Delta P s(x, y) + \gamma\sqrt{1 + (\partial_x s)^2 + (\partial_y s)^2}, \tag{4.16}$$

Where $\partial_\alpha s = \frac{\partial s}{\partial x_\alpha}$ is shorthand for partial derivative with respect to one coordinate direction. The configuration that minimizes this functional is found by the Euler-Lagrange equation, which in this case takes the form:

$$\frac{\partial \mathcal{L}}{\partial s} - \frac{\partial}{\partial x}\frac{\partial \mathcal{L}}{\partial(\partial_x s)} - \frac{\partial}{\partial y}\frac{\partial \mathcal{L}}{(\partial_y s)} = 0 \tag{4.17}$$

$$\Delta P - \gamma\left(\frac{\partial}{\partial x}\frac{\partial_x s}{\sqrt{1+(\partial_x s)^2+(\partial_y s)^2}} + \frac{\partial}{\partial y}\frac{\partial_y s}{\sqrt{1+(\partial_x s)^2+(\partial_y s)^2}}\right) = 0. \tag{4.18}$$

Eq.4.18 is the Young-Laplace equation ,which can also be rewritten as:

$$\gamma\nabla\cdot\left(\frac{\nabla s(\mathbf{x})}{|\nabla s(\mathbf{x})|}\right) = \Delta P \tag{4.19}$$

Instead of solving the PDE 4.19, it is also possible to minimize numerically the energy functional Eq.4.15 to obtain the interface shape. This approach is indeed exploited by the software Surface Evolver, which we described in the previous Chapter.

# Chapter 5

# Topology Optimization of Robust Superhydrophobic Surfaces

## 5.1 Introduction

As we discussed earlier, superhydrophobicity is commonly associated to the Cassie-Baxter state, i.e. a liquid drop is suspended on a micro- or nano-scale roughness. If a drop in the Cassie-Baxter state is perturbed, for instance if a pressure difference is applied between the drop and the environment, the liquid-air interface will bulge, and eventually the liquid will begin to flow along the side of the posts when the angle $\theta_{bend}$ (see Fig.5.1) exceeds the contact angle $\theta_Y$. This will lead to a Wenzel wetting state, with a strong pinning of the liquid to the substrate. This

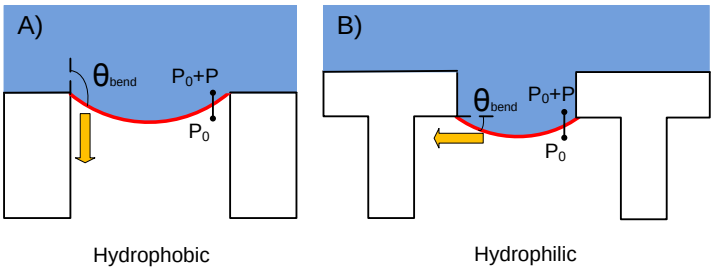


Figure 5.1: A) Interface deformation under applied pressure, for hydrophobic materials. If $\theta_{bend} > \theta_Y$, the contact line slides along the side of the post, in the direction of the yellow arrow B) Analogous setup for hydrophilic materials. If $\theta_{bend} > \theta_Y$, the liquid wets the bottom face of the plate, in the direction of the yellow arrow.

effect is particularly important for inherently hydrophilic materials, for which a suspended metastable state can be achieved through overhanging structures (see

Fig.5.1B), even if the global energy minimum would be a Wenzel state ( see Chapter 1). In such a case, the liquid will irreversibly wet the base of the texture, and the superhydrophobic configuration will be lost. Maximising the robustness of the suspended drop configuration upon applied pressure is therefore fundamental for effective superhydrophobic surfaces.

The research about "Cassie" superhydrophobicity has so far been characterized by a strong dichotomy. On one hand, complex hierarchical structures have been fabricated and tested experimentally, but their modelling is hard, since the structures are usually rough and non periodic [49]. On the other hand, there is an active research for the optimal post shape to achieve a robust Cassie state, which however usually relies on simple shape perturbations to conventional cylindrical or square posts. In this Chapter, we take a step in bridging this gap, applying the tools of topology optimization.

Topology optimization [36] is a structural optimization method with no intrinsic constraint on the topology of the solution, which has been applied in many different engineering fields (see Chapter 3). We will here apply it to obtain an optimal cross section for micro-posts, that minimizes the deformation of the liquid-air interface under applied pressure, thus making the suspended state as robust as possible. We will see that this approach generates interesting branching structures, which resemble natural and artifical superhydrophobic substrates. Moreover, the symmetry and length scale of the optimal design can be tuned in the numeric optimization procedure, leading to a better understanding and control of such features.

## 5.2 Modelling and numeric setup

In this work we will restrict our analysis to a unit cell for a square array of posts (Fig.5.2), neglecting finite size effects at the edge of the drop. We will consider a two dimensional picture, in which the liquid-air interface is flat and suspended on top of the posts (z=0) in the unperturbed configuration, and bulges between the posts to a depth $s(\mathbf{x})$ upon applying a pressure difference $\Delta P$. Such a pressure difference across the liquid-air interface can arise for different reasons, such as the Laplace pressure due to the drop curvature, or the pressure upon impact of a drop on the substrate. We also introduce non dimensional unit for length $l$, surface tension $\gamma$ and pressure p as follows:

$$\begin{aligned} \gamma &= \gamma_0 \bar{\gamma}, \\ l &= L_0 \bar{l}, \\ \mathrm{p} &= \frac{\gamma_0}{L_0} \bar{\mathrm{p}} = P_0 \bar{\mathrm{p}}. \end{aligned} \tag{5.1}$$

Here $L_0$ is the characteristic length of the system, which we will take as the side of the unit cell (typically few $\mu$m), and $\gamma_0$ can be taken as the surface tension of the liquid considered (72.9 mJ/m$^2$ for water at 20 °C). In the following, we will assume non dimensional unit are always used unless otherwise specified. We will also assume $L_0 << l_c = \sqrt{\frac{\gamma}{\rho g}}$, where $l_c$ is the capillary length for the liquid considered. This means we can neglect gravity in our further calculations.

Let us first consider a simple geometry, such as a cylindrical post (cross section is shown in Fig. 5.2 B) ). The deflection of the liquid-air interface among posts can be described by the Young-Laplace equation [26]

$$\begin{cases} \nabla \cdot \left( \frac{\nabla s(\mathbf{x})}{|\nabla s(\mathbf{x})|} \right) = \Delta P & \text{on D} \\ s(\mathbf{x}) = 0 & \text{on } \partial \mathrm{D}_1 \\ \nabla s(\mathbf{x}) \cdot \mathbf{n} = 0 & \text{on } \partial \mathrm{D}_2. \end{cases} \tag{5.2}$$

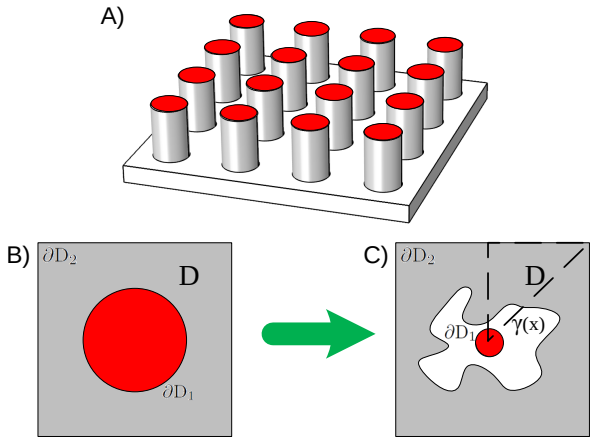


Figure 5.2: A) Sketch of the considered post array. B) Top view of a single post cell, for the basic circular cross section. C) Same view of a single cell, with a variable cross section (white area) around a fixed "nucleus" (red dot) . In the topology optimization procedure, the cross section is not fixed but varies according to the field $\chi(\mathbf{x})$. The dashed line in C) shows the reduced computation domain that exploits the symmetry of the cell.

A Dirichlet boundary condition $s(\mathbf{x}) = 0$ is used at the boundary of the solid structure $\partial \mathrm{D}_1$ to represent that the interface is pinned on the ridge of the post. A Von Neumann condition $\nabla s(\mathbf{x}) \cdot \mathbf{n} = 0$ is applied on the boundary of the unit cell $\partial \mathrm{D}_2$ to account for the symmetry of the post array (in the following, we will also exploit the symmetry of the cell to work only on one eighth of the domain).

For the optimization procedure, we will now slightly modify this setup. We still consider a "solid" support ($s(\mathbf{x}) = 0$, red dot in Fig.5.2C) in the centre of the domain, but now the post cross section is allowed to change around it, in order to provide an optimal support for the interface. The distribution of material at

point $\mathbf{x}$ inside the cell is described by the design variable $\chi(\mathbf{x})$, a scalar field which ranges from 1 (completely solid) to 0 (completely empty) through intermediate values.

The field $\chi(\mathbf{x})$ will be coupled to Eqs.5.2, leading to the following formulation of the problem:

$$\begin{cases} \nabla \cdot \left( K(\chi) \frac{\nabla s(\mathbf{x})}{|\nabla s(\mathbf{x})|} \right) = \Delta P & \text{on D} \\ s(\mathbf{x}) = 0 & \text{on } \partial \mathrm{D}_1 \\ \nabla s(\mathbf{x}) \cdot \mathbf{n} = 0 & \text{on } \partial \mathrm{D}_2. \end{cases} \tag{5.3}$$

Where $K(\chi)$ is defined as:

$$K(\chi) = K_{max} + \frac{(1 - K_{max}) \cdot q \cdot (1 - \chi)}{(q + \chi)} \tag{5.4}$$

Given the form of Eqs.5.3 and 5.4, it is possible to understand the effect of the design variable $\chi(\mathbf{x})$ on the solution $s(\mathbf{x})$. Where $\chi(\mathbf{x}) = 1$, $K(\chi)$ is equal to $K_{max}$, which is fixed to be a large value ($10^4$ in this case). This can be seen as a steep increase of the local surface tension of the interface. The value $\Delta P$ on the right side of Eq.5.3 becomes then negligible, and the liquid-air interface $s(\mathbf{x})$ does not deform significantly. We therefore recover an approximate "solid" condition $s(\mathbf{x}) \simeq 0$. On the other hand, If $\chi(\mathbf{x}) = 0$ ("empty space"), $K(\chi) = 1$, and we recover the Young-Laplace equation out of the support of the post, as in Eqs.5.2. Intermediate values of $K(\chi)$ do not have a direct physical interpretation, but are required for a smooth optimization procedure. The interpolation between these two extreme ranges is controlled by the parameter $q$ in Eq.5.4. By choosing a sufficiently small value (here $10^{-4}$), it is possible to drive the optimization procedure to give a well defined "solid-empty" binary design [36].

This formulation also resembles a 2D optimal heat conduction problem, where $K(\chi)$ corresponds to the distribution of conducting material [50].

We eventually need to define an objective function, i.e. a quantity whose minimization with respect to $\chi(\mathbf{x})$ will maximise the support to the liquid-air interface. We choose this quantity, which we indicate as $\Phi\left[s(\mathbf{x}); \chi(\mathbf{x}), \Delta P\right]$, to be the squared integral displacement of the interface (for a given pressure difference $\Delta P$ and material distribution $\chi(\mathbf{x})$):

$$\Phi\left[s(\mathbf{x}); \chi(\mathbf{x}), \Delta P\right] = \int_D s^2(\mathbf{x})\, dA. \tag{5.5}$$

With this choice, we do not control directly the angle between the interface and the side of the post, which is indeed what would trigger the penetration of the liquid among posts. However, Eq.5.5 is easy to evaluate through the optimization procedure, and its minimization naturally constrains the maximum bending angle of the interface [27], although there might be fluctuations along the post ridge.

At every iteration, the topology optimization code updates the value of $\chi(\mathbf{x})$ over the domain and evaluates $\Phi$ and the sensitivity $\frac{\delta\Phi}{\delta\chi(\mathbf{x})}$. We then use this information as input to find the configuration of $\chi(\mathbf{x})$ that minimizes the objective function $\Phi$, using the method of moving asymptotes (MMA) [39]. Details on the sensitivity analysis and the implementation of the code can be found in the paper by Olesen et al. [38]. We will also introduce a constraint on the maximum solid fraction per unit cell as:

$$\int_D \chi(\mathbf{x})\, dA \leq f_{sl}. \tag{5.6}$$

Remembering Cassie-Baxter relation $\cos\theta_{CB} = f_{sl}\cos\theta_Y - (1 - f_{sl})$ , Eq.5.6 can conveniently be interpreted as a constraint on the static contact angle shown by a surface patterned in this way.

The specific coupling $K(\chi)$ we use in Eqs.5.3 will generate a structure connected to the boundary $\partial\mathrm{D}_1$, which "radiates" the support to the $\chi \simeq 1$ regions [50]. This effectively make our analysis a shape optimization with many degrees of freedom, while the general topology optimization routine we use could as easily generate disconnected topologies.

There are a few reasons for the choice of connected designs. First, it is well known that dense and thin posts, ideally down to the nanometer scale, offer increasingly better support to drops in the Cassie-Baxter state [1, 51]. However, it is perhaps more interesting to optimize the shape of a *single* texture element, which can then be scaled up or down in size according to fabrication and performance constraints. Second, if we are interested in obtaining a hydrophobic behaviour from hydrophilic materials, overhanging structures are required. In this perspective, the central support in our optimisation can be considered as the stem of the post (see Fig.5.1), while we effectively optimise the cross section of the top plate. Eventually, we argue that connected structures would show higher mechanical robustness than hair-like features, in particular to buckling and shear loads. This latter property is of great relevance for practical fabrication purposes, since most practical application would include significant stresses for the substrates [52].

A final remark regards the length scales in the optimal design: at every iteration in the optimisation routine we calculate a smoothed version $\tilde{\chi}(\mathbf{x})$ of the design variable $\chi(\mathbf{x})$, applying a PDE filter [53]:

$$L_{diff}^2 \nabla^2 \tilde{\chi}(\mathbf{x}) = \tilde{\chi}(\mathbf{x}) - \chi(\mathbf{x}). \tag{5.7}$$

While calculating the sensitivity, $\tilde{\chi}(\mathbf{x})$ is then used. This process allows to control the minimum size of the features appearing in the optimal design through the characteristic diffusion length $L_{diff}$ . As we will discuss in the next section, without filtering small length scale features would appear in the optimal design,

ideally down to the mesh scale. However, these small solid features surrounded by empty space are transformed by the diffusion step in a homogeneous area with intermediate $\chi(\mathbf{x})$ value, and thus are penalized by the $K(\chi)$ function, which favours a binary solid-empty solution. The main advantage of this filtering technique is its formulation in terms of a partial differential equation, which relies on the same numeric tools used for Eqs.5.3.

The actual implementation of our optimization routine is a Matlab code, that relies on the commercial software COMSOL to solve the partial differential equations at every iteration step.

## 5.3 Discussion of optimized designs

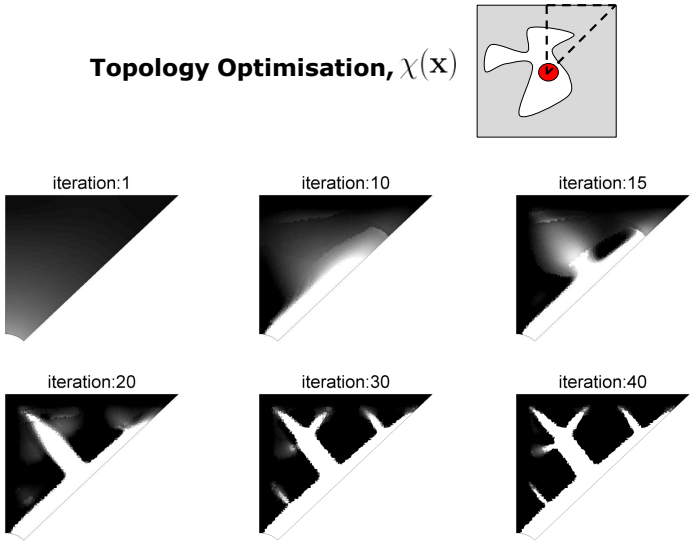


Figure 5.3: Snapshots of selected topology optimization steps, over a reduced domain that exploits the symmetry of the unit cell.

Fig.5.3 shows a typical sequence of steps in the topology optimization procedure. We start from an initial homogeneous distribution of material over the whole domain, equal to the desired solid surface coverage $f_{sl}$, which is imposed as a constraint. In just a few steps, we observe a swift transition to a binary design, with the material (white in Fig.5.3) accumulating along the diagonal of the unit cell. In later stages, further branching appears in the cross directions, and the overall designs appears to minimize the empty space between solid features.

In Fig.5.4 we compare the performance of a cylindrical post (A) and an optimized design (C) inside a unit cell, for a pressure difference of $\Delta P = P_0$. The surface plots displayed on the right (B-D) show the vertical displacement $s(\mathbf{x})$ obtained through Eqs.5.2. For both structures, the solid fraction is $f_{sl} = 0.25$. It

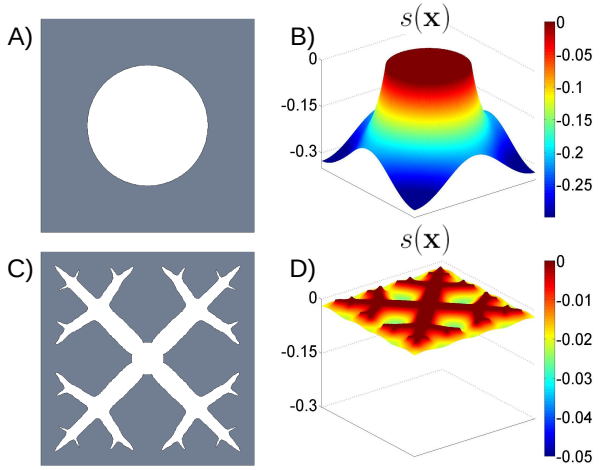


Figure 5.4: A) Top view of a cylindrical post with solid fraction $f_{sl} = 0.25$. B) Displacement plot for applied pressure $\Delta P = P_0$. C) Optimized material distribution with solid fraction $f_{sl} = 0.25$. D) Displacement plot for the topology optimized design.

is easy to see the enhanced performance of the topology optimized structure, with the mean displacement reduced by a factor 10. There are different reasons why the optimised design is more effective. It is clear that the branching in the optimal structure increases the length of the contact line, where the surface tension acts on the side of the post to balance the effect of the applied pressure difference. This result in a reduction of the interface deformation. However, we think that just choosing a meandering cross section would not improve dramatically the performance. Lobaton and Salamon [27], for instance, considered a simpler sinusoidal perturbation to a circular cross section. While significantly increasing the contact line length, such a shape modification showed modest improvement in the critical pressure value. The added feature of our optimal designs is the convenient placement of the branches, that adjust to the cell shape (here a square unit cell, however analogous solution have been tested for hexagonal lattices) to reduce the gaps between solid features. We therefore argue that the significant reduction in the surface displacement arises from the interplay of optimal location of the main branches and increased contact line length coming from the secondary branches.

This physical picture makes it easy to understand the effect of the filtering length $L_{diff}$ on the optimal design.

It can be seen that, for any value of $L_{diff}$, the structure branches along the diagonals of the square cell, thus filling the largest gap between two posts. If the resolution is sufficiently fine, further branching appears, with new branches filling the gap among the diagonals. The process continues for even smaller length

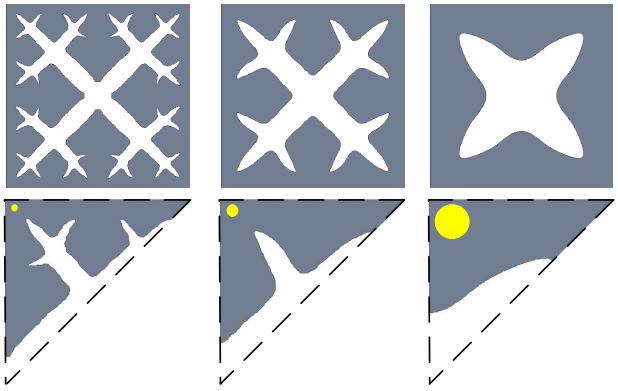

Figure 5.5: Optimal design for $f_{sl} = 0.3$ and $L_{diff}$=0.5, 1, 3 times the meshsize $h_{mesh}$. The designs shown in the upper row are obtained by solving for the domain shown in the bottom row. The radius of the yellow dot in each column is equal to $L_{diff}$.

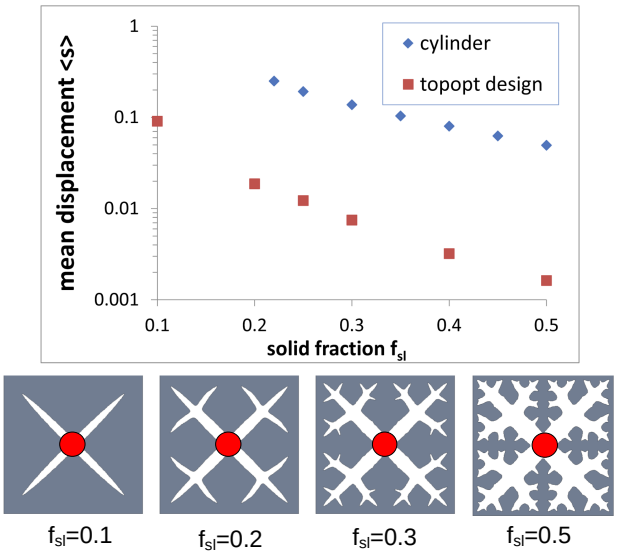


Figure 5.6: Optimal designs as a function of solid fraction $f_{sl}$. The red dot represents the fixed support in the optimisation procedure. In the chart, the mean vertical displacement of the liquid-air interface is compared for cylindrical posts and topology optimised ones.

scales and we get an overall quasi-fractal behaviour. It is then possible to see how the filtering procedure constrains the minimal length scale in the optimal design. This control over the level of detail in the optimal design allows us to obtain structures suitable for fabrication, i.e. with a feasible amount of branching.

These fractal-like structures resemble several biologic surfaces (such as the lotus leaf), which use analogous multi-scale structures to achieve their superhy-

drophobic properties. Our designs are however planar, while most plants are characterized by a three dimensional pattern. A three dimensional optimization would however be very intensive in terms of computation resources. It is however possible to complement the suggestions from topology optimization with general knowledge from superhydrophobic surfaces, to get an even more effective texture. Indeed, most artificial and natural superhydrophobic surfaces are characterized by a micron scale texture with superimposed nanometric roughness. The cross sections shown here should then be considered an optimal micron scale pattern, over which nano-grass features can be grown, thus achieving a multi-layer support for the interface.

In Fig.5.6, we eventually analyse the dependence of the mean interface displacement $\langle s \rangle = \sqrt{\frac{1}{D}\int_D s^2(\mathbf{x})\, dA}$ on the solid fraction $f_{sl}$ for a fixed filter length $L_{diff} = 0.75\ h_{mesh}$, where $h_{mesh}$ is the characteristic mesh size. An increasing branching for larger solid fraction is clearly seen in the optimal designs, which results in a better support for the interface. In the chart we compare the mean displacement for the optimal design to the displacement for a post of circular cross section and same $f_{sl}$. We can see that the optimised design always performs better than the simple circular cross section, and even more so for large solid fractions, which is again a consequence of the higher degree of branching in the optimised configuration.

## 5.4 Fabrication and characterization of topology optimised designs

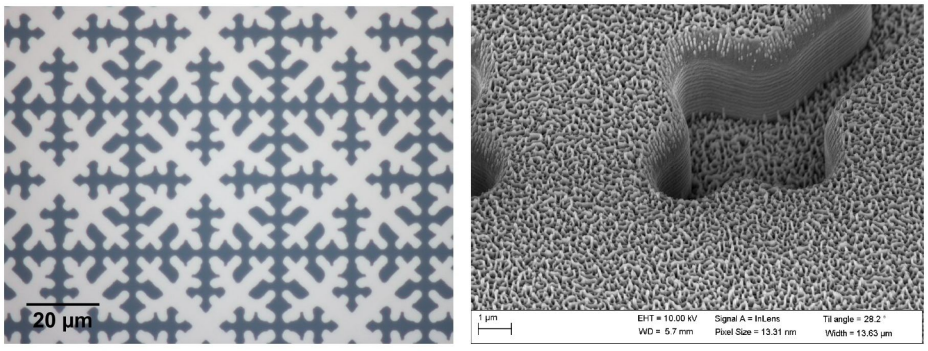


(a) (b)

Figure 5.7: Left: Optical microscope image of the UV-lithography mask for an optimised design. Right: Detail of the Nickel negative shim for injection moulding. The black silicon method generates the sub-micron roughness, which is effectively transposed to the mould. Both pictures have been taken by Nis K. Andersen, and are reproduced with permission from [54].

The optimal designs described in the previous sections have been fabricated by Nis K. Andersen as part of his M.Sc. final project, and are currently been characterized in terms of their wetting and mechanical properties. We will here briefly describe some preliminary results, which are useful in assessing the feasibility of the suggested designs.

A first consideration regards the fine tuning of the optimal designs. It is well understood that sharp features are difficult to realize on micron or sub-micron scale. Therefore, the branches of the topology optimised designs have been adjusted to have a constant thickness equal to the lithographic resolution, and smooth round tips (see Fig.5.7a).
The fabrication steps are the following:
Selected optimised designs, corresponding to different solid fractions $f_{sl}$, have been included in a UV lithography mask (Fig.5.7a). A silicon master has then been fabricated through Deep Reactive Ion Etching (DRIE), and subsequently Nickel has been deposited on the surface to obtain a negative design shim (Fig.5.7b). Eventually, the Nickel template is used in the injection moulding process to transfer the pattern to a polymer substrates (the selected polymer for these tests is Topas8007) .

An unexpected advantage of the topology optimised designs, if compared to isolated pillars, is an increased ease of release of the polymer from the mould. As a matter of fact, thin, rod-like structures tend to get bent or distorted in the release phase of the moulding procedure, while this effect is less intense for the connected optimised designs, which can thus be fabricated with a higher aspect ratio.

As discussed before, hierarchical micro- and nano-roughness offer a two-layer support for the Cassie configuration, and are widespread in nature. It is thus interesting to add such a feature to our designs. Nano-roughness can be introduced on the silicon master by the so called "black silicon" method [55]. This procedure involves a controlled reactive ion etching, which affects the post top face and base faster than the side walls. It is therefore possible to obtain posts with rough tops and smooth sides. It is interesting to notice that such fine features can be transposed with high fidelity in the moulding process (see Fig.5.7b).

We eventually discuss some preliminary results concerning the characterization of the substrates. This set of tests were performed on the silicon "master", treated with a FDTS hydrophobic coating to achieve a large static contact angle. The topology optimised substrates perform well under standard water-repellency and self cleaning tests (they show high static contact angle, low hysteresis, easy dust removal), but then the same applies to surface patterned with cylindrical posts with the same lattice spacing. It is therefore important to get a comparative analysis of different geometries, mainly with respect to the performance upon pressure perturbations , which was the optimization goal of the numeric

algorithm. To this purpose, in Fig.5.8 static contact angles are shown for drop impacting on the substrate from different heights (different terminal velocities), for three different patterns. These are: topology optimised structures in a 40 $\mu$m square lattice, topology optimised structures in a 80 $\mu$m square lattice and cylindrical posts in a 40 $\mu$m square lattice, as sketched in the picture. All structures are the same height (2.3 $\mu$m). We observe a clear transition in the contact angle value for two design, associated to the onset of a strong pinning. This is representative of a Cassie-to-Wenzel transition, and is observed for fast impacting drops. However, it is possible to see that the dot pattern (blue triangles in the plot) is the first to fail, followed by large topology optimised structures (red dots), while smaller optimised structures (black squares) maintain the Cassie configuration over the range of velocities considered. It is necessary to mention that more statistics has to be acquired on this test. These preliminary results however seem to corroborate the theoretical prediction described in the previous sections.

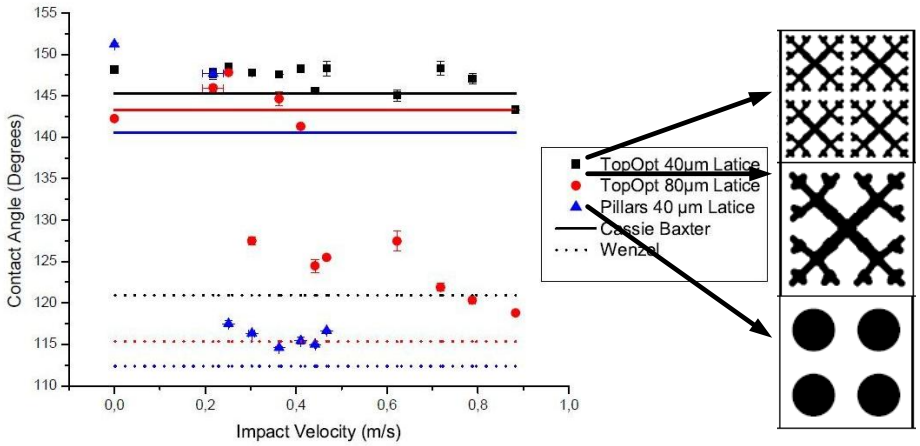


Figure 5.8: Impacting drop experiment on the silicon sample, for the designs shown on the right. The transition from Cassie to Wenzel state is clearly visible, and consistently delayed for the topology optimised designs. Although preliminary, this results are consistent with what the numerical model predicts. Adapted with permission from [54].

## 5.5 Conclusion and outlook

In this Chapter we applied topology optimisation to the stability of superhydrophobic surfaces. We found that this technique is very effective for the task. Branching structures are found to be optimal to support hydrostatic pressure for a Cassie-Baxter state, in a two dimensional analogy to natural micropatterns. We also analysed the effect of a solid fraction constraint on the optimal design, as well as the use of a PDE filter to obtain designs suitable for fabrication. Ongoing work

regards the fabrication and characterization of such optimised microtextured surfaces. Preliminary fabrication results obtained at DTU Nanotech suggest that the optimal shapes can be reproduced with a high degree of precision using common lithographic techniques. We are currently analysing the reproducibility of the optimised designs through injection moulding and the characterization of the wetting properties of such substrates.

# Chapter 6

# Parametric Optimization of Inverse Trapezoid Oleophobic Surfaces.

## 6.1 Introduction

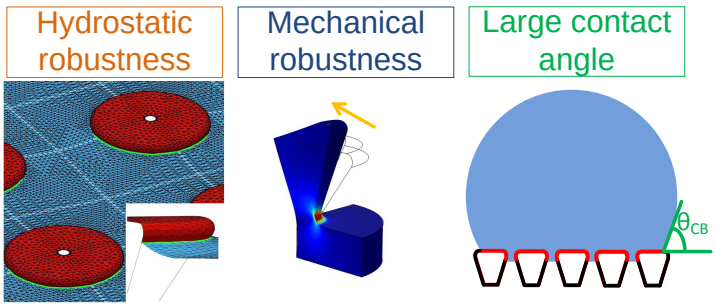


Figure 6.1: Sketch of the objective functions we consider for an ideal oleophobic pattern.

In this Chapter we will describe an optimization approach for oleophobic surfaces. An oleophobic surface is a surface that, through micro-patterning, exhibit an oil-repellent behaviour (organic liquid drops exhibit large static contact angles, and small roll-off angles), even though it is made of intrinsically oleophilic materials.

As discussed in Chapter 2, the Cassie-Baxter state commonly associated with superhydrophobicity can be realised as a metastable state. In fact, a suspended

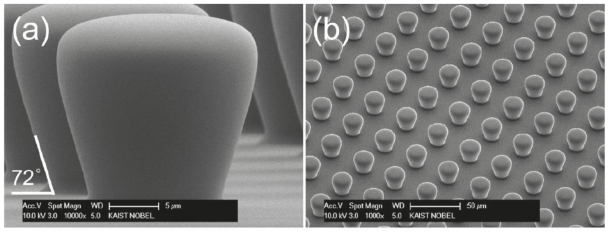


Figure 6.2: SEM image of a single PDMS inverse trapezoid (a) and an array of them (b) from Im [15]

configuration is the global energy minimum only if [1],

$$\cos\theta_Y \leq \frac{-f_{gl}}{r - f_{sl}}, \tag{6.1}$$

where, as usual, $r$ is the roughness of the surface, and $f_{gl}$ and $f_{sl}$ are the air-liquid and solid-liquid interfaces per unit base area of the drop, respectively. Since the right side of Eq.6.1 is always negative, the inequality is never satisfied for hydrophilic materials ($\cos\theta_Y > 0$). Nevertheless, *local* energy minima, corresponding to a suspended solid-air interface, are possible, and thus a micro-texture can convert a oleophilic substrate into a metastable oleophobic or even superoleophobic one. This local energy minimum can be attained using an overhanging texture, so that the local contact angle with the sidewalls of the posts matches the Young contact angle. Since this equilibrium is not a global energy minimum, its stability against perturbations, such as an applied external pressure, must be carefully tested. We will here consider a wider picture, accounting for three different objective functions of a candidate oleophobic microstructures (see Fig.6.1). These are: (a) the maximum pressure difference the liquid-air interface can withstand while being in the suspended state, (b) the mechanical robustness of the micro-structures and (c) the apparent or macroscopic contact angle shown by drops on the texture. We will show how the interplay of these objective functions is essential in defining an optimal oloephobic structure. As a test geometry, we will consider inverse trapezoids as those realized by Im in [15] and shown in Fig.6.2. These structures have been shown to be realizable in a wide range of shape and aspect ratios with high regularity, combining PDMS replication procedures and backside 3D diffuser lithography.

## 6.2 Modeling and setup

From now on, we will consider a drop sitting on a square array of inverse trapezoid posts, as can be seen in Fig.6.2 and later in Fig.6.6. A complete description of a drop on a textured surface is a rather delicate task, that could include dynamic effects and several length and time scales [56]. Some relevant features of such a

system can however be explained in terms of simpler static considerations. First of all we will describe the liquid-air interface on the textured substrate, defining a model to assess the capillary stability of the suspended Cassie-Baxter configuration. We will then consider the mechanical robustness of the microstructures, using linear elasticity theory. To generalize the scope of the analysis, we introduce normalized surface tensions, lengths and pressure as follows:

$$\begin{aligned} \gamma_{ij} &= \gamma_0 \bar{\gamma}_{ij}, \\ l &= L_0 \bar{l}, \\ P &= P_0 \bar{P} \end{aligned} \tag{6.2}$$

Where $\gamma_0$ will be the liquid-air surface tension for the considered liquid, for instance $\gamma_0 = 21.7$ mN/m at 19 $^o$C for octane [57]. $L_0$ will be a characteristic length for the texture, and we choose it to be $L_0 = 5\,\mu$m, which is consistent with experimental studies [13, 15]. $P_0$ can be related via Young-Laplace equation to the other quantities, so $P_0 = \gamma_0/L_0 = 4.34 \cdot 10^3\,\mathrm{N/m^2}$.

### 6.2.1 Wetting analysis: energetic considerations and failure modes

If we neglect effects due to the finite size of the drop (i.e., the drop radius is much larger than the texture size), we can restrict our analysis to a unit cell of the texture, exploiting the periodicity of the system. We will also forget about gravity effects - this assumption is valid if the drop size is smaller than the associated capillary length $l_c = \sqrt{\frac{\gamma}{\rho g}}$, where $\gamma$ is the liquid-air surface tension, $\rho$ is the fluid density and $g$ is the gravitational acceleration.

As shown by several authors [28, 58], a drop on a micro-texture finds a local energy minimum if the local contact angle $\theta_{loc}$ with the solid wall equates the Young contact angle $\theta_Y$, i.e.

$$\cos\theta_{loc} = \cos\theta_Y. \tag{6.3}$$

Furthermore, it can be shown [28, 58] that this equilibrium will be stable for infinitesimal displacements if the profile of the pillars/trenches is convex, i.e. the centre of curvature is inside the solid phase. These conditions then put a first set of constraints on the candidate profiles for an oleophobic texture.
In any case, a transition to a fully wetted configuration is still possible under applied pressure at the liquid-air interface. Among others, Tuteja [13] has underlined the relevance of two failure mechanisms for such overhanging structures. If $\theta_{loc}$ exceeds $\theta_Y$, the contact line will slide along the pillars side, eventually wetting the base of the micro-structures (this failure mode is termed "angle" or "$T^*$-failure" in [13] and is shown in Fig.6.3A). Alternatively, the liquid-air interface could bend enough for the meniscus to touch the bottom of the texture, triggering a transition to a fully wetted state. This process is termed "height" or

"$H^*$ -failure" in [13] and is shown in Fig.6.3B).

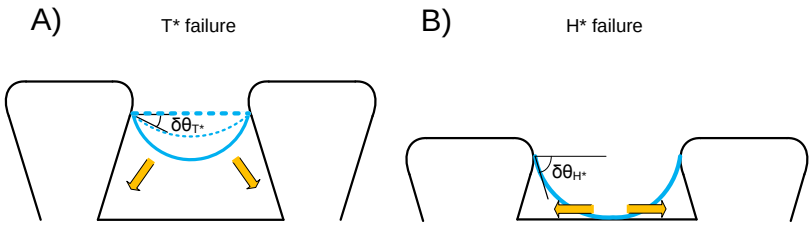


Figure 6.3: 2D Sketch of the possible failure modes for a suspended drop, with relevant geometric parameters shown. A) $T^*$ failure: the local contact angle gets too large for equilibrium, and the fluid slides on the side of the post. B) $H^*$ failure: the bending liquid-air interface touches the bottom of the texture, leading to full wetting.

The critical pressure triggering either failure mode can be obtained analytically only for simple geometries, such as two dimensional ridges. Alternatively, a numerical simulation can be used to predict the shape of the interface under applied pressure and therefore the onset of the failure mode. We carried out such simulation using the software Surface Evolver, introduced in Section 3.3.

### 6.2.2 Modelling of surface deformation

Although it is possible to get an approximate description of the liquid-air interface on textured surfaces, an exact analytic solution is often not available, and numerical modelling is therefore required to account for specific geometries. Some authors (Lobaton [27] , Zeng [26], Emami [49]) have already considered the static problem of a liquid-air interface under applied pressure. However, Zheng et al. [26] consider already hydrophobic materials, while Lobaton and Salamon [27] assume sharp corners that pin the contact line. Our numerical model will instead be fully three-dimensional, thus allowing the sliding of the contact line along the side of the pillar structures.

The standard Surface Evolver evolution takes downhill steps according to a provided energy function, the minima of which represent equilibrium interface configurations, as discussed in Section 3.3. Each vertex in the interface mesh is acted upon by a force depending on how much its displacement affects the surface area (through the surface tension) or the liquid volume (through the prescribed pressure). Details on the implementation can be found in the software manual [33]. A typical Surface Evolver setup for our geometry is shown in Fig.6.4. In order to find the maximum hydrostatic pressure for which a suspended state can be supported by the posts, we run successive simulations with increasing applied pressure difference $\Delta P$. While we increase the pressure, the interface slides along the post side to satisfy the contact angle condition Eq.6.3, and bulges

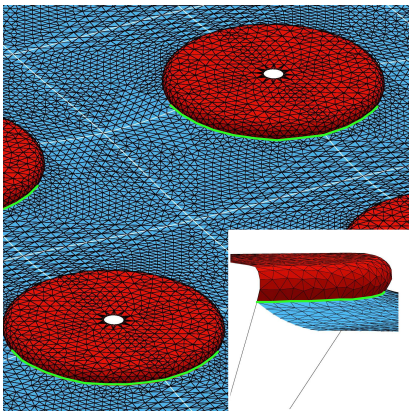

Figure 6.4: Main figure: top view of the inverse trapezoid array inside Surface Evolver. The red facets represent the wetted solid surface, while the blue facets are the liquid-air interface. The contact line is coloured green. Insert: close up on the computation domain, where the curvature of the liquid-air interface is visible.

to match Young Laplace equation $\Delta P = \gamma\kappa$. The breakthrough pressure is then reached when the interface slides all the way along the post side to the base of the simulation box ($T^*$ failure), or touches the base of the domain while bulging ($H^*$ failure).

### 6.2.3 Modelling of mechanical robustness

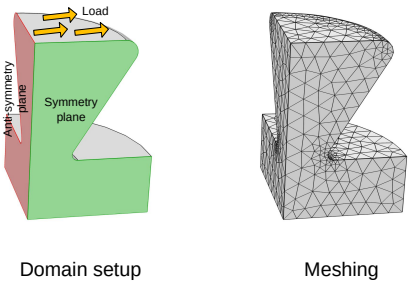


Figure 6.5: Typical domain and mesh used for the linear elasticity analysis, in the commercial FE software COMSOL [30].

A novel element in our optimality analysis will be an assessment of the mechanical robustness of the posts. Oleophobic surfaces can find application in multiple fields, ranging from lab-on-a-chip devices to food processing, where the integrity of the surface functionality will be compromised as smaller or larger areas are damaged; even minor changes of the surface may lead to pinning, contamination and ultimately functional failure. While of key importance for any practical application, such issues are rarely addressed. The lifetime of any struc-

ture based on overhanging micro-structures will benefit if the surface is able to support different kinds of mechanical stresses.

We therefore perform a linear elasticity analysis to constrain feasible geometries, using the commercial FE software COMSOL. We focus on a shear load acting on the top face of the structures, since this would generate large stresses at the neck of the trapezoids and corresponds to a range of common situations encountered, for instance, during mechanical cleaning. The equations solved are then, using tensor notation:

$$\begin{cases} \partial_\alpha \sigma_{\alpha\beta} = 0 & \text{on D} \\ \sigma_{\alpha\beta} n_\beta = \tau_\alpha & \text{on } \partial\text{D}. \end{cases} \tag{6.4}$$

where $\sigma_{\alpha\beta}$ is the Cauchy stress tensor, and $\tau_\alpha$ is a boundary load. The material considered in the simulation is a PDMS (Polydimethylsiloxane) elastomer, corresponding to the structures described by Im [15].

The modelling and failure analysis of elastomers is a complex topic, since their response to stress depends dramatically on parameters such as their composition, curing, and temperature. Their ability to stretch several time their original size is usually described in terms of hyperelastic models, such as Mooney-Rivlin's. It is only in the limit of small deformations, however, that we recover a linear elastic response [59]. In this work , we will therefore limit ourselves to this regime, which can already give a useful insight into the dependence of the mechanical properties of the posts on their shape and aspect ratio. The relevant material parameters we will use are then a Young's modulus $Y = 6 \cdot 10^5$ Pa and Poisson ratio $\nu = 0.49$ [60, 61].

Using a symmetric boundary condition along the direction of the load allows us to model only half of the structure. Moreover, given the linearity of our model, we can use an antisymmetric boundary condition on the plane passing through the centre of the structure perpendicular to the load direction (see Fig.6.5), and thus solve only for a quarter of the structure. Fig.6.5 shows the computational domain and a typical mesh of $n \simeq 35000$ elements used in the calculations.

## 6.3 Design variables and objective functions

Having described the relevant physical properties of the liquid-solid interaction, we can now proceed to define the design variables.

As stated before, we optimize cylindrically symmetric inverse trapezoid structures, which can be parametrized in terms of the design variables top radius $b$, base radius $a$ and height $h$ (see Fig.6.6). Another useful parameter can be the side angle $\theta_{side} = \arctan\left(\frac{b-a}{h}\right)$, again shown in Fig.6.6. The top corner of the microstructures is smoothed by a fillet of radius $r_{fil} = 0.2\, L_0$, to reproduce the experimental shape obtained by Im [15, 62] . These parameters appropriately

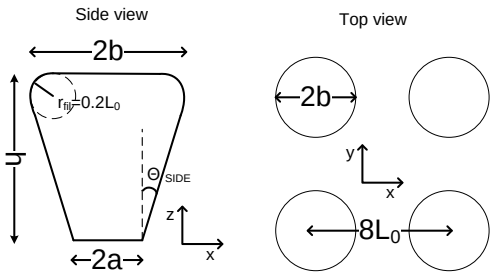


Figure 6.6: Sketch of the trapezoid array considered in the optimization procedure. Relevant geometric parameters (top width $b$, height $h$, base width $a$, side angle $\theta_{side}$, are shown.

define the slenderness and aspect ratio of the structures. However, it is worth noticing that the length scale of the posts is another fundamental parameter in assessing the robustness of oleophobic surfaces. Indeed, scaling down the posts while keeping the solid fraction constant would make the interface more robust to pressure deformation, while keeping the Cassie-Baxter angle fixed. One can expect that scaling down the size of the structures could improve mechanical robustness as well. However, non trivial geometries like inverse trapezoids are difficult to fabricate at arbitrarily small length scales with precision and regularity. At the same time, a high degree of control over aspect ratio and slopes can be achieved experimentally on micron-sized structures. It is therefore interesting to optimise such structures on a scalable unit cell, which should ideally be reproduced at the smallest length scale that assures perfection of features. Since the existence of a suspended state is a necessary condition for oleophobicity, we will use the breakthrough pressure $P_B$ as our first objective function. We define $P_B$ as the smallest pressure difference for which either of the failure mechanism described in the modelling section triggers.

Apart from the breakthrough pressure, we will include two further objective functions, that will be considered as constraints in defining admissible geometries. The first one is the apparent contact angle $\theta_{CB}$, which gives a clear indication of the degree of oleophobic or superoleophobic behaviour shown by the textured surface. Since we assume the suspended configuration for drops, the Cassie relation $\cos\theta_{CB} = f_{sl}\cos\theta_Y - f_{lg}$ can be used to describe the apparent contact angle. This results in a constraint on the solid fraction per unit cell, $f_{sl}$. The last parameter we include in our optimality analysis is a measure of the mechanical robustness of the inverse trapezoids. The most likely mechanical failure for such structures is a tear-off caused by fracture propagation. The ideal mechanical properties of the material can be achieved moving towards nanometric scale features, which will be almost atomically smooth. However, on the scale of several microns that we address in this work, the presence of cracks and other defects

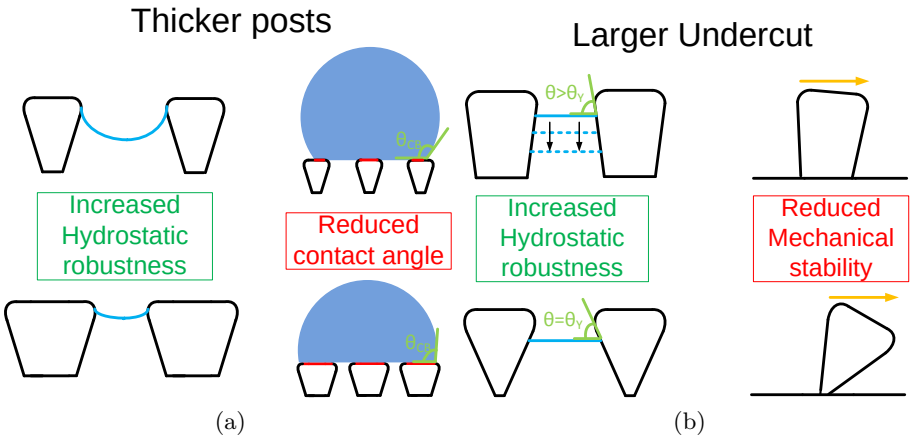


Figure 6.7: Examples of how changes in the geometry will have conflicting effect on different optimality parameters. In Fig.6.7a, post thickness is increased, resulting in better support to the liquid air interface, at the cost of an increased solid wetted area $f_{sl}$. In Fig.6.7b, a larger undercut makes it easier to match the contact angle with the sidewalls, but increases the stress at the neck of the post.

can lower the performance sensibly. A detailed analysis of this phenomenon is however beyond the scope of the current work, where we want to assess how the shape and aspect ratio of the posts affects the mechanical performance as part of a broader parametric optimization. We will therefore introduce a simple yet relevant measure of the response of the structures to an applied shear load, which is the maximum principal strain in the structure. The utility of this measure is twofold. First, by measuring it, we can assess the range of validity of the linear approximation we use in modelling the elastomer structures. Second, we can expect large strains to be directly correlated to the onset of a tear-off failure. We then argue that a maximum strain threshold can be a useful confidence bound in characterizing such structures. As an example, we will consider a shear load of modulus $|\vec{\tau}| = P_0/2$, and a threshold strain of $10\% - 15\%$.

## 6.4 Results and discussion

To show the interplay of the different objective functions, we plot them as a function of the design variables introduced in the previous section, for a fixed Young contact angle $\cos\theta_Y = 0.3$ (i.e. $\theta_Y = 72.5^o$). In Fig.6.8a we show the breakthrough pressure $P_B$ (plotted as contour lines in "warm" color scale), the apparent contact angle $\theta_{CB}$ (green dashed contours) and the maximum percent strain (blue dash-dot contours), as a function of the trapezoids top width $b$ and side angle $\theta_{side}$. The trapezoids height is fixed at $h = 2\,L_0$.

It can be seen that the three objective functions present opposing trends.

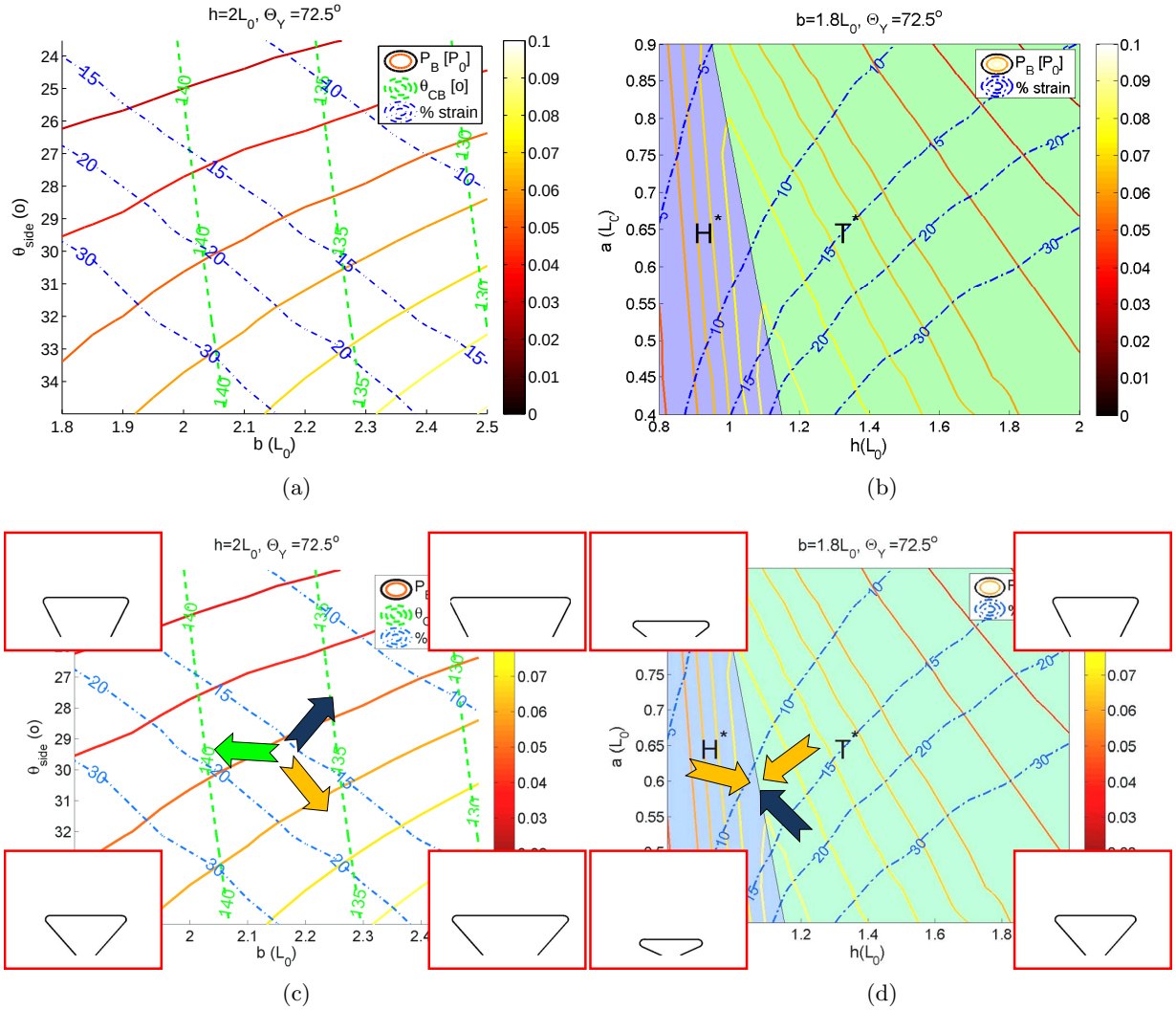


Figure 6.8: a) $b$-$\theta_{side}$ parameter space (h=$2L_0$), $\cos\theta_Y = 0.3$. b) $a$-$h$ parameter space ($b$=$1.8L_0$), $\cos\theta_Y = 0.3$. In each plot, the color legend is as follows: warm color scale: Breakthrough pressure, Green: apparent contact angle $\theta_{CB}$ , Blue: percent strain. The blue and green patches in Fig.6.8b identify the $H^*$ and $T^*$ failure modes, respectively (see Sec. 6.2). c)-d) copies of fig (a)-(b) showing the interplay of the optimality parameters. Each arrow represent an optimality direction, for mechanical robustness (blue), apparent contact angle (green) and maximum breakthrough pressure (orange). In each corner of the geometric space, the corresponding trapezoid is shown.

we sketch two significant cases in Figs.6.7a and 6.7b. For example, a larger breakthrough pressure $P_B$ would be achieved by increasing the top surface radius $b$, while keeping the side angle and cell size fixed (Fig.6.7a). In this way, we effectively reduce the spacing between solid features. This means that a higher pressure would be required to cause a significant bulging of the liquid-air interface, which is at the origin of both the $T^*$ and $H^*$ failure modes. However, increasing b would change the wetted solid fraction per unit cell, which results in a lower apparent contact angle $\theta_{CB}$. In the same way, a large $\theta_{side}$ for fixed top radius $b$ would reduce the risk of $T^*$ failure, as Eq.6.3 suggests. However, this results in a smaller base for the pillar, which implies very large stresses will build up at its neck, increasing the risk of failure and tear off of the posts. From a design point of view, the geometric parameters space can then be imagined as partitioned into regions of almost constant $\theta_{CB}$ and strain values, inside which the geometry that gives the maximum $P_B$ is well defined. If we instead considered only $P_B$-optimality, we would be lead to asymptotically large values of b and $\theta_{side}$. This corresponds to trapezoids with large top plate and minute supports, which would show modest contact angles and be prone to tear-off even for small applied loads. Similar considerations apply to figure Fig.6.8b, where we fix the pillar top width $b = 1.8\,L_0$ and change the height $h$ and base width $a$. Here an optimal height in terms of the breakthrough pressure $P_B$ can be found, corresponding to the transition from the $T^*$ failure mode to the $H^*$ failure mode. Because of the specific shape of inverse trapezoids, the height and side angle are connected by $\theta_{side} = \arctan\left(\frac{b-a}{h}\right)$. In other words, if we make the posts higher for a fixed top area (this reducing the risk of $H^*$ failure), we reduce $\theta_{side}$ (increasing the risk of $T^*$ failure). Therefore it is not convenient to arbitrarily increase the height of the posts, as would be the case for superhydrophobic surfaces, but the optimal height is rather the one for which both failures would happen for the same pressure. Since the $b$ parameter is fixed, the apparent contact angle is almost constant at $\theta_{CB} \simeq 145^o$ throughout Fig.6.8b (small variations coming only from the roundness of the corners), and is therefore not displayed in the picture. In the a-h plane, the strain is minimum for short trapezoids with almost parallel wall (low $h$, large $a$), and grows with the side angle and height of the structures.

Plots like figure Figs.6.8a and 6.8b can then be considered optimality charts for oleophobic surfaces with specific constraints. The balance between optimality parameters is clearly depicted in Fig.6.8c and Fig.6.8d, where each arrow points in the optimal direction for a given parameter (green for contact angle, blue for mechanical robustness and orange for sustainable hydrostatic pressure). In each corner of the design parameter space, the corresponding geometry is also shown as an insert.

The usefulness of this analysis as a design tool can be shown by further

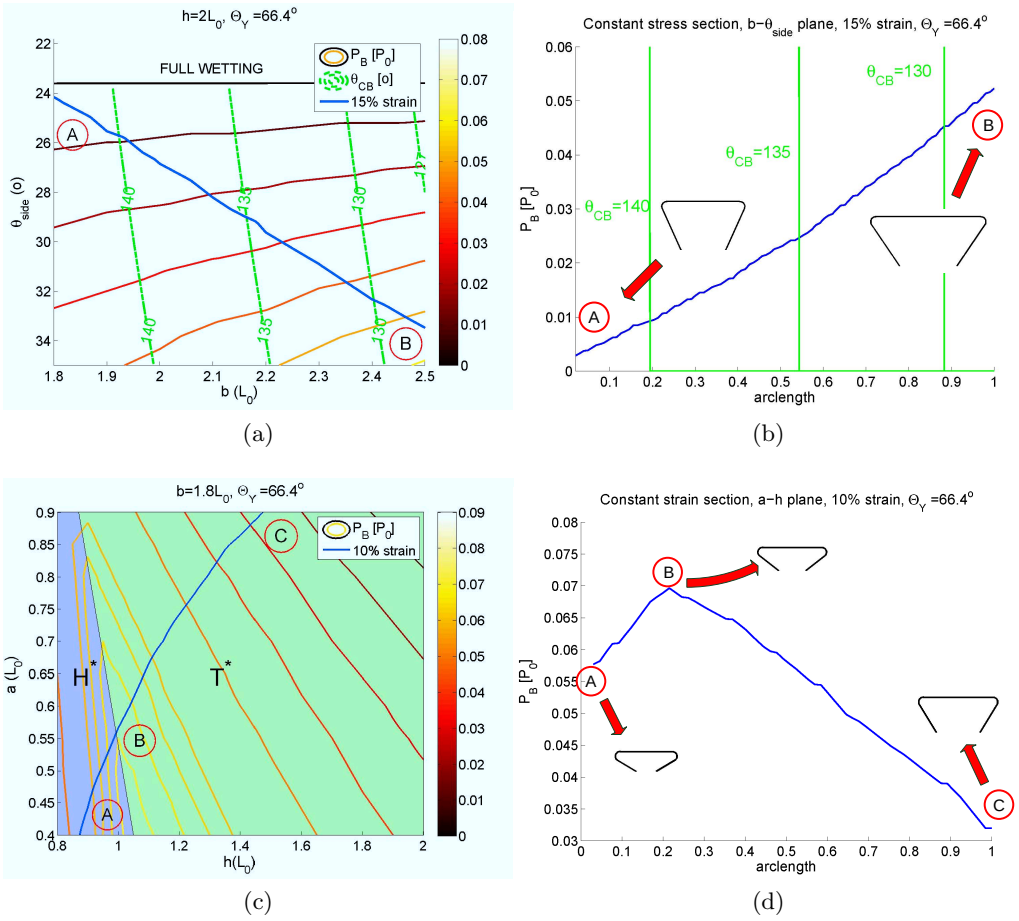


Figure 6.9: a)-c) $b$-$\theta_{side}$ and $a$-$h$ plots for $\cos\theta_Y = 0.4$ as in Figs.6.8a and 6.8b. A possible choice for a maximum strain contour is shown. b)-d) Breakthrough pressure along the contour in fig. a)-c). Relevant positions in both plots are mapped using labels and corresponding geometries are also shown.

restricting the performance constraints. To show the applicability of this method for different wetting configurations, let us also change the Young contact angle so that $\cos\theta_Y = 0.4$ (i.e. $\theta_Y = 66.4^o$ ). In Figs.6.9a, 6.9c we show plots similar to Figs.6.8a, 6.8b, but with a fixed maximum strain contour (10 and 15 %). If we move along this line, we get a curve for $P_B$ , as shown in Figs.6.9b, 6.9d. It is then possible to identify the most $P_B$-robust structures capable of supporting a prescribed mechanical stress, and associate them to the corresponding shape. Relevant positions in both plots are mapped using labels and correspondent post shapes are also shown.

## 6.5 Conclusion and outlook

In this Chapter we analysed in detail the interaction between wetting and mechanic robustness of textured oleophobic surfaces. Design charts showing the interplay of these objective functions have been introduced for different values of the intrinsic contact angle of the substrate. We have shown how these objective functions present opposite trend, so that a non trivial optimal shape is defined in terms of design requirements.

While we addressed the elasticity of the post as a measure of their robustness, flexible posts have an intrinsic interest, since they will exhibit a different wetting behaviour if compared to rigid ones, with remarkable consequences. Roman and Bico [63], for example, have described in detail how flexible hairs can bundle under capillary action, or pierce the liquid-air interface if stiff enough. A thorough analysis of different wetting mode on flexible hairs has been carried out by Blow and Yeomans [64], who present a phase-space diagram with transition between different "Cassie-like" and "Wenzel like" as a function of hairs' contact angle and stiffness.

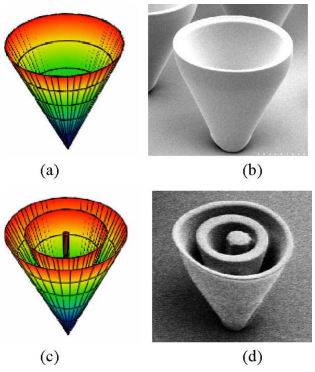


Figure 6.10: Inverse cone structures obtained with continuously rotational inclined UV lithography, from [65].

A final remark concerns the specific geometry addressed in this work. Although general in the observed trends, our results are partly dependent on the specific post shape we analysed. This is however not a major constraint, since inverse trapezoids are among the simplest overhanging geometries that can be micro-fabricated in a cheap and regular fashion. Apart from the backside diffuse lithography employed by Im in [15], it is worth mentioning the use of inclined UV lithography [65] as a mean of fabricating 3D overhanging patterns. This lithographic technique exploit a moving stage to expose a positive photoresist at a given angle, thus obtaining slanted features. By continuously changing the exposure angle, conical structures as those shown in Fig.6.10 can be obtained, remarkably similar to those analysed in this chapter.

# Chapter 7

# Modelling Unidirectional Liquid Spreading on Slanted Microposts

## 7.1 Introduction

Anisotropic wetting and spreading of drops on natural and artificial surfaces are often a consequence of the micro-structure of the substrate [1]. For example, drops spreading on superhydrophobic surfaces patterned with micron-scale ridges reach an elongated final state [66, 67], and a drop imbibing into a surface patterned with posts can form a faceted final configuration, which reflects the symmetry of both the lattice and of the posts themselves [68].

The physics behind this behaviour was first described by Gibbs, who pointed out that an interface can pin on the edge of a post over a range of angles, as illustrated in Fig.7.1. The pinning occurs because there is a free energy penalty to the interface moving away from the edge in either direction, as it would then have to form an angle with the adjacent surface which differs from the equilibrium contact angle. A pinning strength that depends on the lattice direction leads to the drop having one or more preferred directions of motion, and hence anisotropic drop movement and shapes.

In this Chapter we focus on unidirectional drop motion: where the symmetry of the underlying surface structure can pick out one easy direction of spreading [69, 70]. Such surfaces occur naturally, for example, the unidirectional motion of droplets on butterfly wings results from their ratchet-like structure [4, 71], and rye-grass leaves shed water in a preferred direction [17] due to the asymmetric contact angle hysteresis. Microfabricated surfaces that lead to uni-directional motion are, on the other hand, a very recent development. Unidirectional spreading has been observed on bent silicon micro pillars [16], while other authors

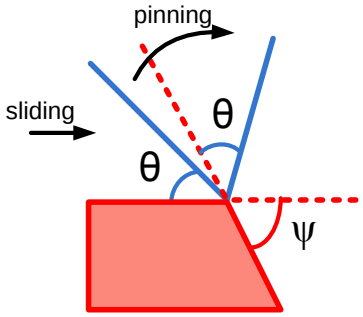


Figure 7.1: Gibbs' pinning on the corner of a post. The interface (blue line) remains pinned to the post over the range of angles indicated by $\psi$ as there is a free energy barrier to its moving in either direction.

[72, 18] were able to transport droplets on vibrating ratchet structures. Similar results where obtained using PDMS replicas of the naturally occurring asymmetric micro-texture [17] taken from rye grass, and anisotropic hysteresis was observed on printed ratchetlike surfaces [73]. Despite the different material and geometries employed, the unidirectional liquid motion consistently reflects the asymmetry of the substrate on microscopic length scales. This highlights the importance of understanding the underlying physical phenomena involved.

We use a two-phase lattice Boltzmann algorithm to model the imbibition of an hydrophilic surface patterned with slanting posts, varying the contact angle of the substrate and the tilt angle of the posts. For a range of contact angles we observe a single, preferred spreading direction as described in recent experiments [16]. The results are in good qualitative agreement with a two-dimensional model of the uniaxial spreading proposed in [16], and enable us to describe the corrections to the model for a three dimensional geometry. By visualizing the shape of the contact line, we describe in detail the mechanisms through which the interface pinning and de-pinning occurs.

## 7.2 Modelling

### 7.2.1 Governing equations

To model a two phase system interacting with a surface, we apply the diffuse interface scheme introduced in Chapter 4, which we briefly recall here. The free energy of the system, $\Psi$, is given as:

$$\Psi = \iiint_D \left( \psi_b(\rho) - \mu_b \rho + \frac{1}{2}\kappa |\nabla \rho|^2 \right) dV - \iint_{\partial D} \mu_s \rho \, dS. \tag{7.1}$$

The first term in the integrand of Eq. 7.1 is the bulk free energy density [48]

$$\psi_b(\rho) = p_c \left[ \left(\nu^2 - \beta\tau_W\right)^2 - (1 - \beta\tau_W)^2 \right]. \tag{7.2}$$

where $\rho_c$ , $p_c$ , $\tau_W$ and $\beta$ are, respectively, the critical density, critical pressure, reduced temperature and a free parameter controlling the density difference between phases and $\nu = \frac{\rho - \rho_c}{\rho_c}$ is a normalised density. In our simulations, the main parameters are set as follows: $\kappa = 0.01$, $p_c = 0.125$, $\beta = 1$, $\tau_W = 0.3$, $\rho_c = 3.5$. The corresponding surface tension is $\gamma = 0.04$ and the surface thickness is $\chi = 0.9$ (in simulation units).

The hydrodynamics of the fluid is described by the continuity and Navier-Stokes equations:

$$\partial_t \rho + \partial_\alpha(\rho u_\alpha) = 0, \tag{7.3}$$

$$\begin{aligned} \partial_t(\rho u_\alpha) + \partial_\beta(\rho u_\alpha u_\beta) &= -\partial_\beta P_{\alpha\beta} + \\ &+ \partial_\beta \left(\rho\mu \left[\partial_\beta u_\alpha + \partial_\alpha u_\beta\right] + \rho\lambda\delta_{\alpha\beta}\partial_\gamma u_\gamma\right), \end{aligned} \tag{7.4}$$

where usual conventions are assumed. As mentioned, the equations are solved using the Lattice Boltzmann algorithm described in Chapter 3.

### 7.2.2 Geometry

Each post has a flat top face, and a square cross section of dimensions $w$, which was typically chosen to be equal to 5 or 10 computational grid spacings. The posts sidewalls form an angle $\phi$ with the positive $x$-axis, and extend to a height $h = 4w$ above the surface. We start considering a rectangular array of posts with lattice constant $a_x = 4.6w$ in the x direction and $a_y = 4w$ in the y direction as shown in Fig.7.2.

Placing a sufficiently large drop on the surface to allow significant spreading through the posts is computationally expensive. Therefore we define a reservoir of fluid in the centre of the post array typically extending across $\simeq 10w$ and reaching to the top of the posts. If the fluid density inside the reservoir decreases below the equilibrium density of the liquid phase, new mass is slowly added to feed the imbibition. The contact angle of the liquid with both the posts and the substrate is $\theta$ which we vary in the range $30^o$ to $70^o$. This range is representative of different hydrophilic material, for example the polymers considered in [16] or [19].

We first consider a quasi-2D geometry which allows us to concentrate on the directional spreading in the $x$-direction. We choose a simulation box of length $40w$ in the $x$-direction, $4w$ in the $y$-direction and $6w$ along $z$, with periodic boundary conditions along both $x$ and $y$. The reservoir spans the simulation box in $y$ corresponding to simulating a cylindrical drop with interfaces which lie, on average, parallel to the $y$-direction. The average of any fluid motion is along

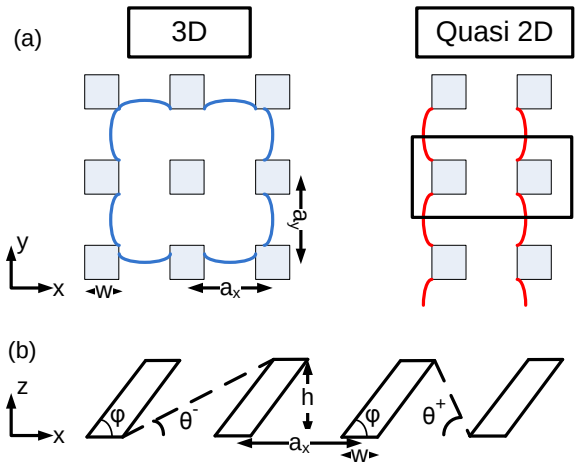


Figure 7.2: (a) Diagrams to contrast the quasi-2D and full 3D geometries used in the simulations. The red and blue lines represent typical interface positions.(b) Side view of the posts showing the interface geometry corresponding to the threshold for movement which is assumed in deriving Eq.7.5.

$x$. We then present results for a full 3D geometry, using a simulation box with typical dimensions $40w \times 32w \times 6w$, with periodic boundary conditions along $x$ and $y$. A schematic comparison of quasi-2D and 3D spreading is given in Fig.7.2a.

## 7.3 Results

Fig.7.3 shows snapshots of the imbibition process as a function of time for the quasi-2D geometry and a contact angle $\theta = 45^o$. The interface advances in the positive $x$-direction, but not in the negative $x$-direction, because of pinning on the posts. As pointed out in Chu et al. [16], a good understanding of why this occurs follows from assuming that the interface is pinned at the top corner of the posts, and ignoring any interface curvature along $y$. We illustrate this situation in Fig.7.2(b). The bottom of the interface will advance along the surface until it reaches the equilibrium contact angle $\theta$. If this enables the interface to reach the next post, it will wet this post and move forwards. If not, it will remain pinned, because any forward motion will increase the free energy. Because of the two dimensional nature of the model, it is easy to work out the threshold Young angles for spreading in the two directions as a function of the post geometry. Defining these as $\theta^+$ and $\theta^-$ for spreading along $+x$ and $-x$ respectively, gives [16]

$$\theta_{cr,\pm X} = \tan^{-1}\left(\frac{H}{a_x - w \mp H\cot(\phi)}\right). \tag{7.5}$$

Thus there are three regimes: the interface can remain pinned in both direc-

tions, advance just along $+x$, or move forward in both directions. The different regimes predicted by Eq.7.5 are indicated in Fig.7.4 as a function of the Young angle $\theta$ and the post inclination $\phi$. Note that, for $\phi = 90^0$, $\theta^+ = \theta^-$ as expected. The value of $a_x$ also affects the transition between different spreading regimes, as is apparent from Eq.7.5: closer posts will ease the spreading, while posts that are further apart will make it more difficult. Our choice of $a_x = 4.6w$ allows us to observe the different spreading regimes over the range of contact angles $\theta$ and slanting angles $\phi$ that we consider.

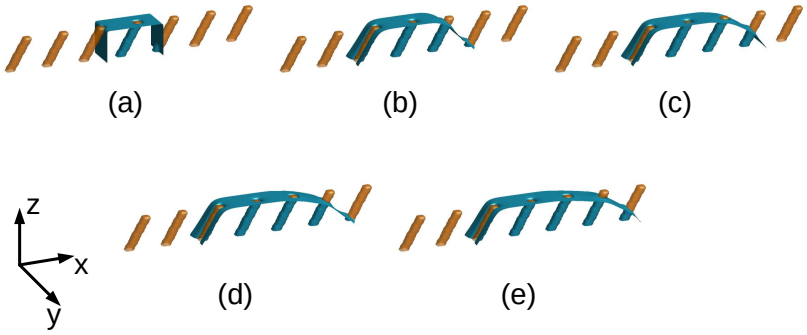


Figure 7.3: Advancing front in the unidirectional spreading regime for contact angle $\theta = 45^o$ and post angle $\phi = 60^o$. This is a quasi-2D geometry with periodic boundary conditions along $y$. The snapshots (a)-(e) correspond to 0,1,2,4,5 $\times 10^4$ time steps.

Fig. 7.4 also shows the results of simulations for the quasi-2D geometry. All three regimes are reproduced in the simulations. The analytic model gives a good account of the boundaries between them, but spreading in both directions is slightly more difficult than predicted by the 2D theory. The simulations allow us to identify this as being due to the details of the interface pinning on the posts. For an interface advancing along the positive $x$-axis, where the post points towards the direction of travel, we observe three different possible pinning mechanisms, labelled $||$, $B$ and $X$ in Fig.7.5. If the post is almost vertical, the leading interface is disconnected and is pinned to the vertical sides of the post ($||$ label). For a more pronounced post tilt the interface remains disconnected, but does not reach the top of the final post ($B$ label). For large tilt the leading interface is connected and has reached the equilibrium contact angle on the substrate. However, in contrast to two dimensions, the final post is only partially wet ($X$ label). The situations, $B$ and $X$, where the interface has only reached the top of the penultimate post is only observed for slanted posts. It occurs because the interface can take the correct contact angle on the final post without a large penalty in curvature energy. The interface configuration resembles that in the partially suspended state identified in Kusumaatmaja and Yeomans [71].

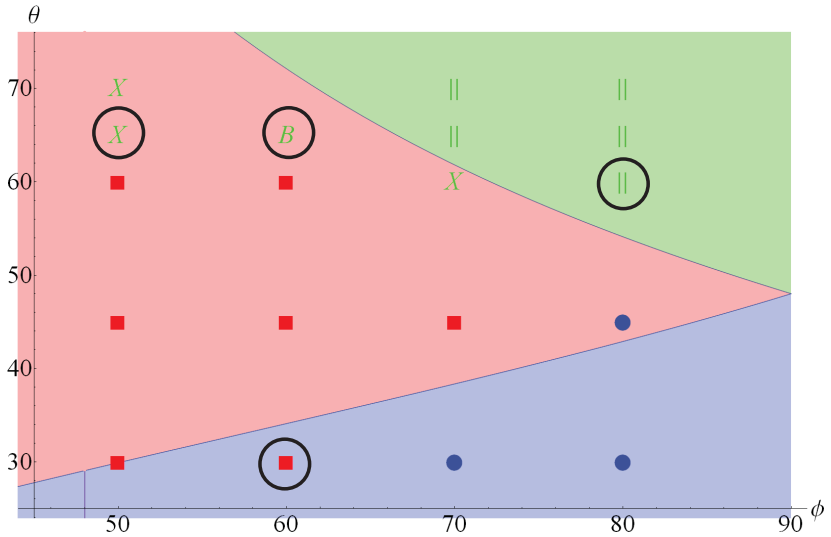


Figure 7.4: Plot of the different wetting regimes in the quasi-2D geometry, as a function of wetting angle $\theta$ and post angle $\phi$. The other geometric parameters are: $a_x = 4.6w$, $h = 4w$. The legend is: blue/circles: bidirectional spreading, red/squares: unidirectional spreading, green: no spreading. The different green symbols represent different pinning modes in the forward direction, as described in Fig.7.5. Selected configurations (black circles) are shown in Fig.7.5. The background indicates wetting regimes from a theory assuming a 2D geometry, see Eq.7.5 [16].

We considered a small spacing between posts to facilitate spreading over a wide range of wetting angles. It is however worth noticing that, if the spacing between posts were increased in the spreading direction, configurations analogous to the 2D theory would likely appear, with pinning on the final rather than penultimate row of posts.

In the hard direction for spreading, $-x$, the interface is pinned at the edges of the final line of posts, adjusting to their slope, as shown in Fig.7.5, label $*$. Bidirectional spreading only occurs for very low contact angles $\theta < 30^o$ or posts close to vertical $\phi > 70^o$.

These simulations correspond to quasi-static spreading, with the fluid reservoir replenished very slowly. Borderline configurations between different wetting modes (such as $\phi = 70^o$, $\theta = 60^o$) are very sensitive to exact details of the position and filling speed of the reservoir. This is expected because the free energy barriers and capillary forces driving the flow are very small. A comparison between two resolutions used shows that, as expected, spreading is slightly more difficult for a narrower interface. We also note that, if the rate at which fluid is added to the reservoir is increased, the resulting inertia allows the fluid to de-pin from the top of the posts, forming a spherical cap.

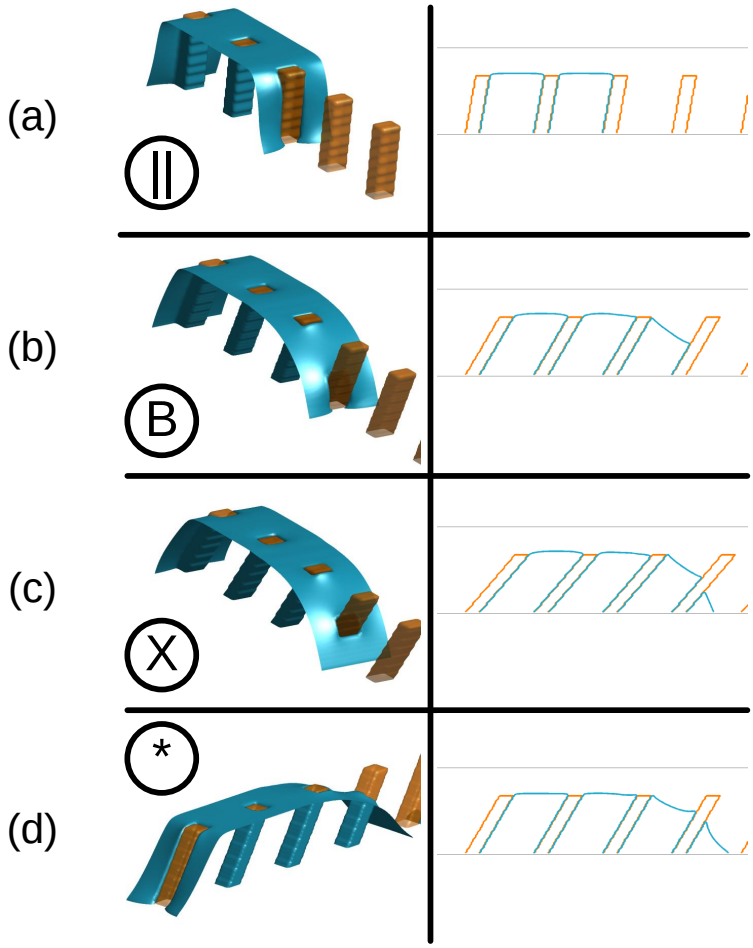


Figure 7.5: Different pinning configurations appearing in the quasi 2D simulations. The first three correspond to the easy spreading direction, $x$, while the last shows the typical pinning in the hard direction, $-x$. They can be identified with the circled points in Fig.7.4 by matching symbols. Cross sections taken through the centres of the posts are shown on the right as full blue lines. (a) If the post is almost vertical, the leading interface is disconnected and pinned to the vertical sides of the post (|| label). (b) For more pronounced post tilt the interface remains disconnected, but does not reach the top of the final post ($B$ label). (c) For large tilt the leading interface is connected and has reached the equilibrium contact angle on the substrate. However, in contrast to two dimensions, the final post is only partially wet. ($X$ label). (d) The interface in the negative $x$-direction is disconnected, and pinned by the sides of the final post ($*$ label). A penguin!

We next report a full three-dimensional simulation which allows the fluid to spread along both $x$ and $y$. The reservoir is defined as a circular region of radius $10w$ in the centre of the domain, and the contact angle is $\theta = 45^o$. In Fig.7.6 we plot contour lines showing the spreading of the drop base for subsequent time

steps. The first plot is for vertical posts; as expected it reflects the symmetry of the lattice. In the second plot the lattice spacing is the same, but the posts are now slanted with $\phi = 60^o$. In the slanting direction, the behaviour is consistent with the quasi-2D model, with the liquid spreading only in the positive $x$ direction. The spreading in the $y$ direction is comparable to the vertical post case. The overall dynamics closely resembles the imbibition observed in experiments by Chu et al. [16]. In Fig.7.6(c) the posts are closer in the x-direction. One can see that the asymmetry of the spreading becomes more pronounced, with the fluid spreading easily from one row to the next along x, while only spreading very slowly along y. This occurs because the thermodynamic driving force for spreading is much stronger in the x direction. For a contact angle of $45^o$ there is slow spreading along y, however for a larger contact angle the fluid will remain pinned along y (the crossover can be estimated from Eq.7.5, taking $\phi = 90^o$ in Figure 4), and/or x (as seen in the quasi-2D simulations reported in Fig.4) . Eventually, in Fig.7.6(d), we simulate densely packed posts in the $y$ direction, while keeping the same $x$-spacing as in Fig.7.6(b). The behavior is now quite different, with the spreading happening first in the transverse direction, and only subsequently along the slanting direction. The unidirectionality is however maintained. These results indicate that the final shape of a spreading drop can be tuned in detail by varying the lattice geometry and tilt angle of the posts, while retaining the relevant property of unidirectionality.

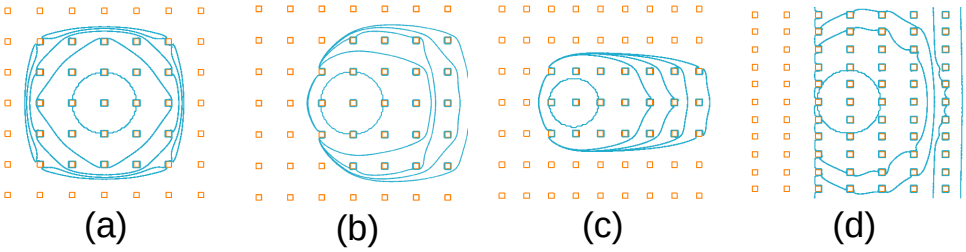


Figure 7.6: Three dimensional spreading for $\theta = 45^o$ and (a) $\phi = 90^o$ , $a_x = a_y = 4.6w$. (b) $\phi = 60^o$ , $a_x = a_y = 4.6w$. (c) $\phi = 60^o$ , $a_x = 3.6w$, $a_y = 4.6w$. (d) $\phi = 60^o$ , $a_x = 4.6w$, $a_y = 2.53w$. The blue contours show the interface position at the base of the drop at increasing times.

## Conclusions and outlook

We have applied a lattice Boltzmann algorithm for two phase flow to model the spreading of liquid drops on a surface patterned by a lattice of slanted microposts. Gibb's pinning of the interface on the sides or top of the posts led to unidirectional spreading over a wide range of fluid-substrate contact angles and inclination angles of the posts. Regimes for spreading in no, one or two directions

were identified, and shown to agree well with a two-dimensional theory proposed by Chu et al [16]. A more detailed numerical analysis of the contact line configurations enabled us to understand deviations from the two dimensional model, and to identify the configurations of the pinned interfaces.

The final drop shape depends on spacing of the post lattice, the contact angle, and the geometry and inclination of the posts. Our simulations correspond to slow spreading, but inertial terms will also alter the final drop configuration. Thus there are many, varied possibilities to use slanted posts to control drop shapes or the direction of a flowing stream of fluid. Contact angles can be varied in situ by electrowetting, and it would be of interest to design substrates with addressable posts where the contact angle of each of the posts could be varied independently to allow steering of capillary flows.

Another exciting possibility is introducing slanted posts into microfluidic channels, in order to tune and control capillary flows. For example, we could obtain a microfluidic logic gate by controlling the pinning on few strategically placed posts inside a micro-channel. In Fig.7.7 we show an example of a "Frey switch", based on this concept. We are considering an open top microchannel T-junction with two slanted posts in the main branch, whose slanting we assume we can control externally. The fluid enters the T-junction through capillary imbibition, but the symmetry of the spreading is broken when the front meets the slanted posts at different angles. The interface is therefore pinned on the right side, but spreads freely on the left side, thus effectively steering the capillary flow. A reversed configuration would allow flow in the right arm, while the two posts leaning towards each other would pin the interface on both sides, stopping the flow unless enough pressure is applied. Controlling the slanting angle of microposts is indeed a complicated tasks form the fabrication point of view, even though the use of magnetic fields to orient paramagnetic posts could be an effective option in implementing such a design.

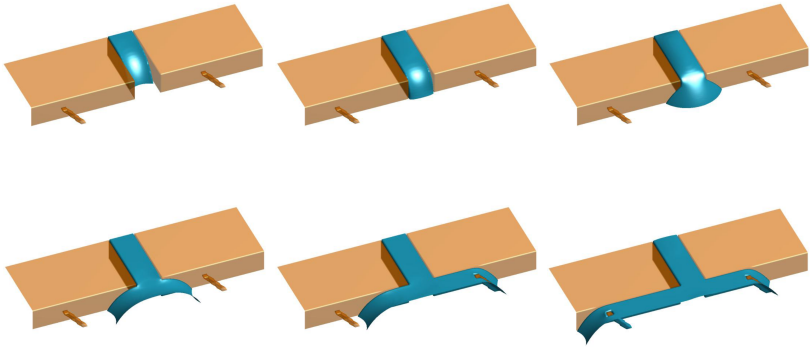

Figure 7.7: Snapshot of capillary imbibition in the switch design. The simulation box is $200 \times 80 \times 30$ lattice units. The symmetry in the early stages of spreading is broken by the asymmetric slanting of the posts, resulting in unidirectional liquid flow.

# Chapter 8

# Jumping of Coalescing Droplets on Superhydrophobic Surfaces

## 8.1 Introduction

Deformed liquid drops or sheets can store significant amount of surface energy, which can be efficiently converted into other energy forms, such as kinetic energy. For example, several fungi of the Ballistospore family exploit this discharge mechanism to release spores in the environment [74, 75]. Boreyko [76] has recently observed how coalescing drops on a superhydrophobic surface can release enough surface energy on contact to detach from the substrate, reducing the wetted fraction of the substrate and thus improving significantly the condensation rate. This behaviour can also be exploited to achieve self-cleaning substrates by removing debris through the jumping mechanism [77]. A similar jumping behaviour has been observed by Lee [78] upon actuation of electrolyte drops. Several authors [79, 80] have also exploited surface tension as a mean of removing or reshaping micron-sized metal structures, which are melted in a controlled fashion by laser pulses. In this Chapter we will introduce a numeric model which is able to describe many of these phenomena with an unified approach. We analyse the relevance of several geometric parameters to identify different contribution to the energy balance and possible dissipation sources. Our model is then compared to existing data [78, 81, 82] to verify the understanding of the underlying mechanics.

## 8.2 Model

In the following we will consider an axially symmetric system, with a liquid phase of density $\rho_{liq}$ and viscosity $\mu_{liq}$ surrounded by a gaseous phase (with density and

viscosity $\rho_{air}$, $\mu_{air}$, respectively). The equations introduced in the following are to be considered in non dimensional form, with a characteristic length scale $R$, and a capillary time scale $T$

$$T = \sqrt{\frac{R^3 \rho_{liq}}{\gamma}}, \tag{8.1}$$

where $\gamma$ is the liquid-gas surface tension. Assuming incompressibility in both fluids, the equations of motion dictated by mass and momentum conservation for the whole system are the continuity and Navier-Stokes equation:

$$\nabla \cdot \mathbf{u} = 0 \tag{8.2}$$

$$\frac{\mathrm{d}\mathbf{u}}{\mathrm{d}t} + \mathbf{u} \cdot \nabla \mathbf{u} \;=\; \frac{1}{\rho}\left(-\nabla \mathrm{p} + \mathrm{Oh}\nabla \cdot \left(\mu\left[\nabla \mathbf{u} + \nabla \mathbf{u}^T\right]\right) - \mathrm{cBo}\mathbf{k} + \delta_S \kappa \mathbf{n}\right). \tag{8.3}$$

Here $\mathbf{u}$ is the velocity field; p the pressure; $\mathbf{k}$ is a unit vector pointing downwards; and $\mathbf{n}$ is the outward unit normal to the surface of the drop. $\mathrm{c}(\mathbf{x})$ is a marker field describing the presence of the liquid phase at a given position in the domain, ranging from 0 (gaseous phase) to 1 (liquid phase). While the fluid properties are constant in the bulk for each phase, at the interface they are interpolated using the following relations:

$$\rho = c + (1 - c)\, D \tag{8.4}$$

$$\mu = c + (1 - c)\, M, \tag{8.5}$$

where $D = \frac{\rho_{air}}{\rho_{liq}}$ and $M = \frac{\mu_{air}}{\mu_{liq}}$ are the density and viscosity ratio, respectively. The non dimensional numbers Oh and Bo that characterize our system are the Ohnesorge and Bond number , defined as ($U = \frac{R}{T}$ is the characteristic velocity for the system)

$$\mathrm{Oh} = \frac{\mu_{liq}}{U R \rho_{liq}} = \frac{1}{\mathrm{Re}} \simeq \frac{\text{Viscosity}}{\text{Inertia}} \tag{8.6}$$

$$\mathrm{Bo} = \frac{\mathrm{R}^2 \mathrm{g}\left(\rho_{liq} - \rho_{air}\right)}{\gamma} \simeq \frac{\text{Gravity}}{\text{Surface Forces}}. \tag{8.7}$$

A final note concerns the boundary conditions applied. The simulation domain is sketched in Fig.8.1. Both the floor and the ceiling of the simulation box enforce free slip boundary conditions. Since the jumping phenomenon is commonly observed on superhydrophobic surfaces, neglecting the friction on the substrate can be considered as a reasonable approximation to ease the treatment of contact line motion. Accounting for a finite contact angle and the force exerted on the contact line could be a further step to reproduce experimental measurements more closely.

Eqs.8.2 and 8.3 are solved on a staggered grid, using the finite difference scheme introduced in Chapter 3 and a fourth order Runge-Kutta algorithm for the time stepping. The pressure term is handled along the lines of the projection

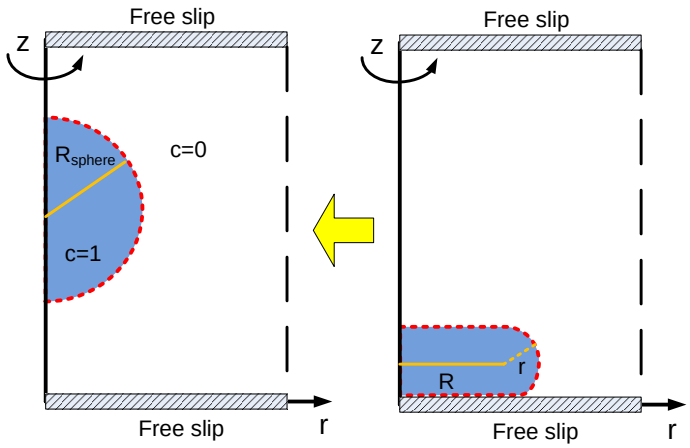


Figure 8.1: Sketch of the axisymmetric domain of the simulation, with boundary conditions specified. The relevant radii $R$, $r$, and $R_{sphere}$ from Eq.8.8, describing the recoil from the elongated disk to a spherical shape, are also shown.

method described by Brown in [83]. We keep track of the interface through the marker method introduced by Popinet et al [40], which we described in Chapter 4.

## 8.3 Results and discussion

### 8.3.1 Electrowetting jump

Recent experiments by Jun and Lee [78, 81] are useful for a validation of our method. They actuate a drop resting on a superhydrophobic substrate with a square pulse of characteristic time $T_{pulse} \simeq 8.7$ ms. In response, the droplet center of mass is shifted and the drop can even detach and jump. The relatively large scale of the experiment (the drop has an initial radius of about 1 mm, and the time scale of the jump is about 10 ms) allows for a clear visualization of the process, and the presence of the electrode helps in confining the drop to a vertical motion. The associated non dimensional numbers are $Oh = 0.0033$ and $Bo = 0.147$, and the experimentally observed efficiency of the energy conversion process is about 20% [76, 78].

It is simple to evaluate the maximum energy stored in a rounded disk of main radius R and height $h = 2r$, as sketched in Figure 8.1:

$$\Delta_{SE} = \gamma \left( A_{disk} - A_{sphere} \right) = \gamma \left( 2\pi R^2 + 2\pi^2 r \left( R + \frac{2r}{\pi} \right) - 4\pi R_{sphere}^2 \right), \quad (8.8)$$

With the additional constraint of volume conservation

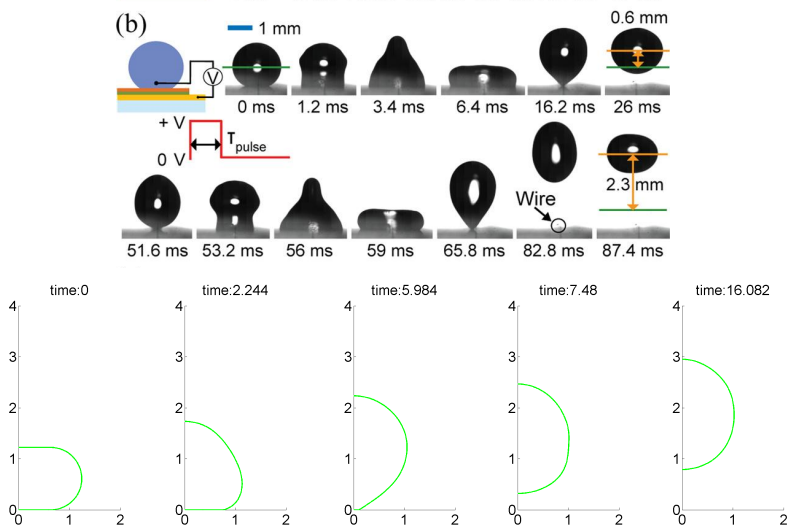


Figure 8.2: Top: electrowetting actuation of drops from [78]. The electric pulse is a square pulse with a characteristic time $T_{pulse} \simeq 8.7$ ms. Bottom: selected profiles from the numeric simulation, with parameters M=0.02, D=0.005, Oh=0.004, Bo=0.15. We observe a qualitative agreement on the time scale of the numeric profiles and the images (times are expressed in ms, lengths in mm). The reproducibility of the jump is not addressed in detail in the aforementioned paper, we are currently carrying out measurements in this sense.

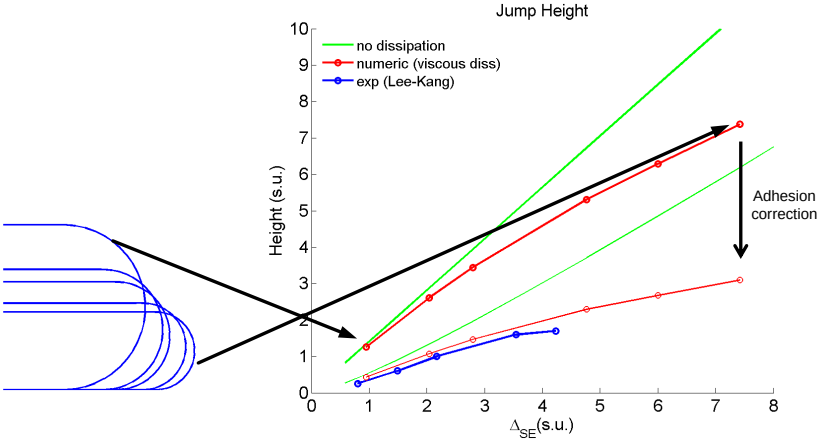


Figure 8.3: Left: Initial conditions for increasingly deformed drops with fixed volume. Right: associated jump heights. Green lines represent the maximum jump height from energetic considerations (Eq.8.8), the red line connects the numerical results, which account for viscous dissipation, and the blue line connects the experimental data from [78]. The thin lines (both red and green) are obtained by reducing the available energy by a factor $\propto \pi R^2$ to qualitatively account for the adhesion to the substrate, as described in the main text.

$$\frac{4}{3}\pi R_{sphere}^3 = \pi R^2 h + \pi^2 r^2 \left( R + \frac{4r}{3\pi} \right). \tag{8.9}$$

In Fig.8.2, we show some snapshots for the simulated detachment of the drop, compared to images presented in [78], for parameters M=0.02, D=0.005, Oh=0.004, Bo=0.15. The simulated drop shapes conform qualitatively to the recorded images, and the time scale is also close. Published data do not allow a more thorough comparison, and we are therefore carrying out similar experiments to get better resolution in the time evolution of the drop, in collaboration with Dr. Miljkovic at MIT. In Fig.8.3 we compare the experimentally measured jump heights from [78] to the numerical results and the maximum jump height from Eqs. 8.8 and 8.9 . A common trend can be observed, namely a larger energy dissipation for highly deformed initial shapes, which results in a jump height further away from the ideal value. This is easily understood looking at the energy dissipation for the different setups. Indeed, highly deformed drops are affected by a larger viscous dissipation related to the internal flow in the drop. However, we can still notice a significant offset between the ideal and numerical results and the experimental ones. A reasonable source of dissipation not accounted for in the simulation is the adhesion work required to create a new liquid-air / solid-air interface when the drop detaches from the substrate. This contribution will naturally scale with the liquid-solid contact area, i.e. $W_{adhesion} \propto \pi R^2$. By subtracting a correction of this kind to the maximum energy available for the jump, we can indeed obtain a good agreement with the experimental data. This suggest that adhesion and internal viscous dissipation are main contribution to energy loss in the system. We are currently modifying the model to account for adhesion directly in the numeric simulation, to further test our hypothesis.

### 8.3.2 Drop size scaling

The jumping phenomenon has been observed over a variety of droplet radii, from a few microns for nucleating drops [12] to millimetre-sized in experiments by Jun [78]. In this section we therefore analyse how the drop size affects its dynamics, and which effects are more or less relevant for different droplet sizes. The drop is initialized in the same way as in the previous section; we will assume $R_0 \simeq 1$ mm, as in the electrowetting results discussed before. We will then consider increasingly small droplets, expressing their radius as a fraction of $R_0$. Since the equations are in nondimensional form, by adequately scaling the Ohnesorge $\mathrm{Oh} = \frac{\mu_{liq}}{UR\rho_{liq}} \propto \frac{1}{\sqrt{R}}$ and Bond number $\mathrm{Bo} = \frac{\mathrm{R}^2 \mathrm{g}\left(\rho_{liq} - \rho_{air}\right)}{\gamma} \propto R^2$, we can effectively control the length scale of the simulation, without changing the simulation box size. We can therefore consider slightly deformed drops with a fixed aspect ratio of $\simeq 2$ at different length scales, and look at the time evolution of the kinetic

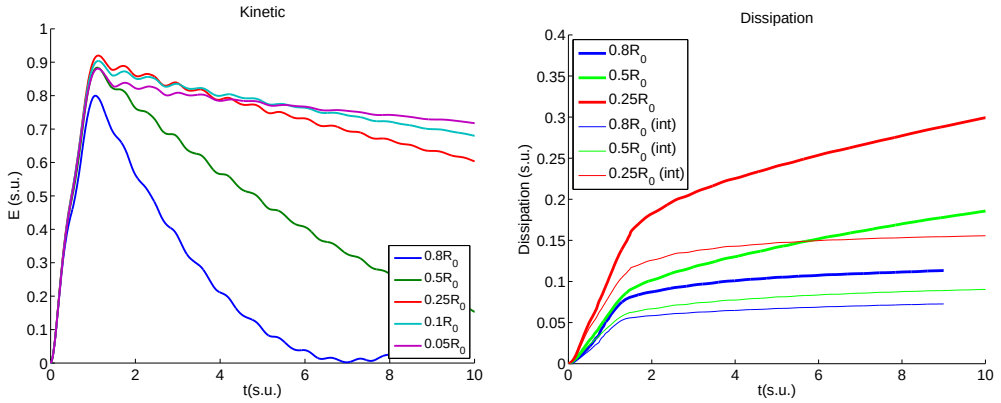


(a) (b)

Figure 8.4: Kinetic energy (Fig.8.4a) and Dissipated energy (Fig.8.4b) over time for different values of the initial radius of the drop. The thin lines in Fig.8.4b represent the energy dissipated inside the liquid phase.

energy of the drops for different radii in Fig.8.4a and the dissipated energy over time in Fig.8.4b.

There are a few common trends to observe. The dissipation plot, for example, shows a characteristic kink, roughly corresponding to the detachment of the drop form the ground. This is probably due to the steep velocity gradient in the recoiling phase, when the mean fluid flow becomes orthogonal to the substrate before the detachment.

The kinetic energy shows a characteristic frequency of oscillation close to the capillary time $T = \sqrt{\frac{R^3 \rho_{liq}}{\gamma}}$, associated to the wobbling of the drop during the flight stage. However, such an oscillation is not observed in the dissipation profiles. We argue that, for the relatively small deformation considered in these simulations, internal viscous dissipation due to drop oscillations is not relevant, and the slow dissipation in the flight stage is due to viscous drag of the gas phase on the drop. Indeed, by integrating only the energy dissipated inside the liquid drop, we observe a saturation after the detachment.

It seems possible to discriminate three "size ranges" with different dynamics.

Large drops (dark blue, green lines, $R \simeq 1$ mm) dissipate little energy, since their Ohnesorge number is small and their velocity modest. Therefore, dissipation is small both in the early stages ( $t \leq 2$, when energy is lost to the viscous recoiling of the liquid drop) and later stages, when drag is likely to be the main source of dissipation. However, the droplets escape velocity (or kinetic energy, Fig.8.4a ) is also small, since gravity plays a relevant role. Medium sized drops (red, light blue lines $R \simeq 100$ to 500 $\mu$m) dissipate more energy both in the retracting and flying phase. As a matter of fact, their Ohnesorge number is larger and their velocity higher, since gravity becomes almost irrelevant in this regime. Even

smaller drops (fuchsia line, $R \simeq 50\ \mu$m) dissipate even more energy in the early stages. However, due to their reduced cross-area, are less affected by drag in later stages, and therefore eventually overcome "medium sized" drops in terms of velocity.

### 8.3.3 Leidenfrost rings

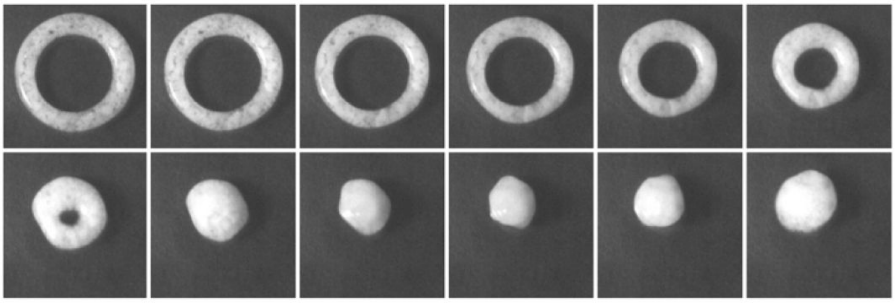

Figure 8.5: Top view of a collapsing liquid ring, from [82]. The time between frames is 8 ms, and the initial radii $R$ and $a$ are 4 and 2 mm, respectively.

We eventually consider a more exotic experiment by Texier et al. [82], which is however very close to our modelling assumptions. In this work, rings of liquid oxygen in the Leidenfrost state were realized by pouring the liquid on a glass substrate and applying an annular magnetic field, which attracts the paramagnetic liquid. Once the field is switched off, the ring collapses with a constant acceleration (see Fig.8.5). Our frictionless, axisymmetric setup looks ideal to test this result. We can also reproduce density and viscosity ratio quite closely ($D = 0.005$ and $M = 0.1$). One main result derived in [82] is the remarkably simple dynamics of the torus in the early recoiling phase. Indeed, it can be shown that the major radius $R$ of the ring evolves in time as [82]:

$$R(t) = R_0 - \frac{\gamma}{\rho R_0 a_0} t^2. \tag{8.10}$$

Here $R_0$ is the initial major radius, $a_0$ is the diameter of the torus and $\gamma$ and $\rho$ are the surface tension and density of the liquid phase. We therefore initialize our simulation according to this geometry i.e. tori with different $R_0$, $a_0$, and dimensionless numbers Bo $= 0.22$, Oh $= 0.0024$. We then compare the numeric evolution to Eq.8.10. In Fig.8.6 we plot the major radius over time, compared with the parabolic trend form Eq.8.10, which is expected to hold in the preliminary collapse phase. The agreement of our numeric results with Eq.8.10 is indeed very good for several values of $R_0$ and $a_0$. The low surface tension of liquid oxygen implies a large Bond number, meaning that the drop will be flattened by gravity, and the jumping harder to observe. The simulations also show the ring

deforming from an initial toroidal shape to an elongated one, under the effect of gravity. However, the jumping can still be achieved considering smaller values of Bo (for instance, smaller rings).

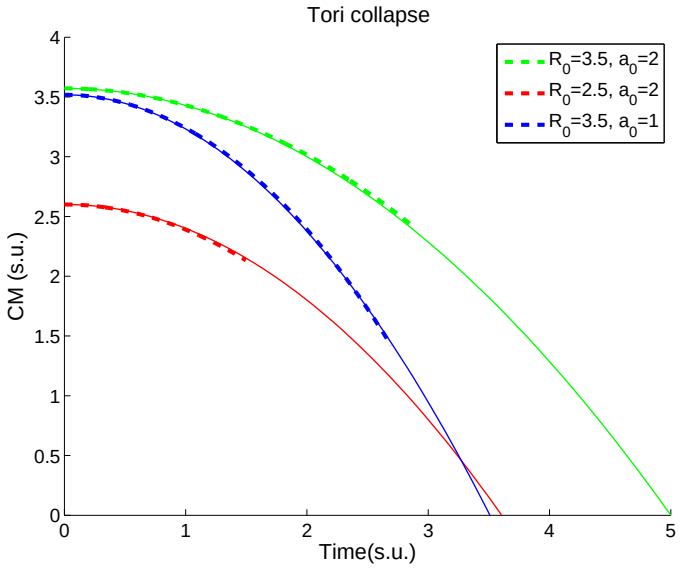


Figure 8.6: Collapse dynamics for toroidal rings of different initial radius $R_0$ and cross section $a_0$. Dotted lines are numerical data, while full lines follow Eq.8.10.

## 8.4 Conclusions and outlook

In this Chapter we analysed and reproduced numerically jumping droplets on superhydrophobic surfaces. Our simulations suggest that different dissipative effects play a role, depending on the coalescing drop size, deformation and adhesion to the substrate. We compared our results to available experimental data, observing good qualitative agreement. An ongoing collaboration with Nenad Miljkovic at MIT aims at testing our simulations experimentally through suitable electrowetting experiments. An interesting extension of the current analysis would be to consider the optimal shape to achieve the highest jump, accounting not only for the stored surface energy, but also for the viscous dissipation in the recoiling phase.

# Chapter 9

# Conclusions and Outlook

The present thesis and literature review show clearly how micro-patterning leads to a great variety of wetting phenomena, which may find technical applications in the near future. We developed analytic models and numeric simulations of these phenomena, which constitute a significant step towards engineering ad-hoc patterns with specific wetting behaviours.

We first addressed the Cassie-Baxter model for super-repellent surfaces, and we analysed how different patterns perform under perturbations of the equilibrium configuration. In Chapter 5, we applied topology optimization to the cross section of microposts, to minimize the deformation of the liquid-air interface under an applied pressure. In Chapter 6, we studied the oleophobic properties of overhanging posts, and addressed their wetting and mechanical properties at the same time. We then moved our attention to dynamic phenomena, both in the extremely hydrophilic and hydrophobic range. In Chapter 7, we analysed how to steer and direct the wetting on a surface patterned with hydrophilic slanted posts, and described the effect of several geometric parameters on the spreading pattern. Eventually, in Chapter 8 we considered the recently observed phenomenon of jumping droplets on superhydrophobic substrates. We described how the terminal velocity of the jump scales with the droplet size, and different sources of dissipation that affect the efficiency of the process.

## 9.1 Outlook

The results described in this thesis suggest several future research directions, both on the technological and fundamental levels.

One clear direction for future research is the experimental fabrication and characterization of the described patterns and associated wetting behaviours. We started several ongoing collaborations with this aim. Nis K. Andersen and

Prof. Taboryski at DTU Nanotech are currently characterizing the topology optimised designs described in Chapter 5. Mikkel B. Klarskov and Prof. Bøggild are working with inclined UV lithography to fabricate slanted microposts inside micro channels, in order to test the results of Chapter 7. Detailed measurements of the jumping behaviour in nano-drops are currently carried out by Dr. Nenad Miljkovic at MIT.

On the fundamental level, the natural step forward is to consider multi-physics problems, i.e. combine wetting and other phenomena. This interplay is twofold. On one hand, electric fields, heat flows, or mechanical actuation can provide excellent tools to control drops and realize tunable, dynamic wetting system. On the other hand, controlling the wetting properties of a substrate can result in enhanced mechanical, thermal or conductive properties.

As regards the mechanical actuation of drops, an interesting extension of the results presented in Chapter 7 is to study "Cassie drops" on flexible cilia. Droplets suspended on an asymmetric texture can exhibit unidirectional motion due to a directional contact angle hysteresis, a mechanism that can be employed to transport a "cargo" inside the liquid [18]. Flexible posts could also be employed to realise switching microfluidic devices such as the T-junction described in the end of Chapter 7.

The lattice Boltzmann scheme described in Chapter 7 is also well suited to analyse phase transitions (such as nucleation or evaporation) combined with different flow configurations, since it naturally includes a thermodynamic description of two interacting phases. Many interesting results have recently been published in this field [12, 84], which show how the heat exchange due to condensation or evaporation can be enhanced on suitably patterned surfaces. An example is the self-ejection of droplets on superhydrophobic surfaces we model in Chapter 8, which allows a continuous nucleation on the substrate, not interrupted by flooding.

Eventually electrowetting, i.e. controlling the wetting properties of electrolyte droplets through electric fields, promises exciting technological applications. For example, confined drops can be used as micro-lenses [85], whose focal length can be adjusted by changing the interface curvature through an electrostatic-induced pressure. The shape of the drop-lens is controlled by the surface geometry, and could benefit from the topology optimization approach we described in Chapter 5.

Opportunities are therefore plentiful, and the best has yet to come.

# Bibliography


[1] P. G. De Gennes, F. Brochard-Wyart, and D. Quéré. *Capillarity and wetting phenomena: drops, bubbles, pearls, waves*. Springer Verlag, 2004. [cited at p. 4, 12, 41, 50, 63]

[2] C. Neinhuis and W. Barthlott. Characterization and distribution of water-repellent, self-cleaning plant surfaces. *Annals of Botany*, 79(6):667–677, 1997. [cited at p. 3]

[3] R. Helbig, J. Nickerl, C. Neinhuis, and C. Werner. Smart skin patterns protect springtails. *PloS one*, 6(9):e25105, 2011. [cited at p. 3]

[4] Y. Zheng, X. Gao, and L. Jiang. Directional adhesion of superhydrophobic butterfly wings. *Soft Matter*, 3(2):178–182, 2007. [cited at p. 4, 63]

[5] E. Bormashenko, Y. Bormashenko, T. Stein, G. Whyman, and E. Bormashenko. Why do pigeon feathers repel water? hydrophobicity of pennae, cassie–baxter wetting hypothesis and cassie–wenzel capillarity-induced wetting transition. *Journal of colloid and interface science*, 311(1):212–216, 2007. [cited at p. 4]

[6] A. R. Parker and C. R. Lawrence. Water capture by a desert beetle. *Nature*, 414(6859):33–34, 2001. [cited at p. 4]

[7] D. L. Hu, B. Chan, and J.W.M. Bush. The hydrodynamics of water strider locomotion. *Nature*, 424(6949):663–666, 2003. [cited at p. 4]

[8] X. Gao and L. Jiang. Biophysics: water-repellent legs of water striders. *Nature*, 432(7013):36–36, 2004. [cited at p. 4]

[9] T. Onda, S. Shibuichi, N. Satoh, and K. Tsujii. Super-water-repellent fractal surfaces. *Langmuir*, 12(9):2125–2127, 1996. [cited at p. 5]

[10] J. Bico, C. Marzolin, and D. Quéré. Pearl drops. *EPL (Europhysics Letters)*, 47:220, 1999. [cited at p. 5]

[11] J. Bico, U. Thiele, and D. Quéré. Wetting of textured surfaces. *Colloids and Surfaces A: Physicochemical and Engineering Aspects*, 206(1-3):41–46, 2002. [cited at p. 5]

[12] N. Miljkovic and E. N. Wang. Condensation heat transfer on superhydrophobic surfaces. *MRS Bulletin*, 38(05):397–406, 2013. [cited at p. 5, 77, 82]

[13] A. Tuteja, W. Choi, J. M. Mabry, G. H. McKinley, and R. E. Cohen. Robust omniphobic surfaces. *Proceedings of the National Academy of Sciences*, 105(47):18200, 2008. [cited at p. 5, 51, 52]

[14] A. Ahuja, J. A. Taylor, V. Lifton, A. A. Sidorenko, T. R. Salamon, E. J. Lobaton, P. Kolodner, and T. N. Krupenkin. Nanonails: A simple geometrical approach to electrically tunable superlyophobic surfaces. *Langmuir*, 24(1):9–14, 2008. [cited at p. 5]

[15] M. Im, H. Im, J.-H. Lee, J.-B. Yoon, and Y.-K. Choi. A robust superhydrophobic and superoleophobic surface with inverse-trapezoidal microstructures on a large transparent flexible substrate. *Soft Matter*, 6(7):1401–1404, 2010. [cited at p. 5, 7, 50, 51, 54, 60]

[16] K. H. Chu, R. Xiao, and E. N. Wang. Uni-directional liquid spreading on asymmetric nanostructured surfaces. *Nature Materials*, 9(5):413–417, 2010. [cited at p. 5, 63, 64, 65, 66, 68, 70, 71]

[17] P. Guo, Y. Zheng, C. Liu, J. Ju, and L. Jiang. Directional shedding-off of water on natural/bio-mimetic taper-ratchet array surfaces. *Soft Matter*, 8(6):1770–1775, 2012. [cited at p. 5, 63, 64]

[18] K. Sekeroglu, U. A. Gurkan, U. Demirci, and M. C. Demirel. Transport of a soft cargo on a nanoscale ratchet. *Applied physics letters*, 99:063703, 2011. [cited at p. 5, 64, 82]

[19] R. J. Vrancken, M. L. Blow, H. Kusumaatmaja, K. Hermans, A. M. Prenen, C. W. M. Bastiaansen, D. J. Broer, and J. M. Yeomans. Anisotropic wetting and de-wetting of drops on substrates patterned with polygonal posts. *Soft Matter*, 9(3):674–683, 2013. [cited at p. 5, 65]

[20] A. Dupuis, J. Léopoldès, D. G. Bucknall, and J. M. Yeomans. Control of drop positioning using chemical patterning. *Applied Physics Letters*, 87(2):024103–024103, 2005. [cited at p. 5]

[21] M. Han, W. Lee, S.-K. Lee, and S. S. Lee. 3d microfabrication with inclined/rotated uv lithography. *Sensors and Actuators A: Physical*, 111(1):14–20, 2004. [cited at p. 6]

[22] H. Bruus. *Theoretical microfluidics*. Oxford University Press, 2007. [cited at p. 10]

[23] J. W. Gibbs. *The Scientific Papers of J. Willard Gibbs*. Dover Publications, 1961. [cited at p. 13]

[24] R. N. Wenzel. Resistance of solid surfaces to wetting by water. *Ind. Eng. Chem*, 28(8):988–994, 1936. [cited at p. 15]

[25] A. B. D. Cassie and S. Baxter. Wettability of porous surfaces. *Trans. Faraday Soc.*, 40(0):546–551, 1944. [cited at p. 16]

[26] Q. S. Zheng, Y. Yu, and Z. H. Zhao. Effects of hydraulic pressure on the stability and transition of wetting modes of superhydrophobic surfaces. *Langmuir*, 21(26):12207–12212, 2005. [cited at p. 17, 39, 52]

[27] E. J. Lobaton and T. R. Salamon. Computation of constant mean curvature surfaces: Application to the gas-liquid interface of a pressurized fluid on a superhydrophobic surface. *Journal of colloid and interface science*, 314(1):184–198, 2007. [cited at p. 17, 40, 43, 52]

[28] A. Marmur. From hygrophilic to superhygrophobic: Theoretical conditions for making high-contact-angle surfaces from low-contact-angle materials. *Langmuir*, 24(14):7573–7579, 2008. [cited at p. 17, 51]

[29] L. H. Olesen. Computational fluid dynamics in microfluidic systems. Master's thesis, Technical University of Denmark, Denmark, 2003. [cited at p. 19]

[30] COMSOL Multiphysics. Comsol multiphysics reference guide, 2008. [cited at p. 19, 53]

[31] L. M. Blow. *Wetting on flexible and anisotropic surfaces*. University of Oxford, 2010. [cited at p. 22, 24]

[32] M. R. Swift, E. Orlandini, W. R. Osborn, and J. M. Yeomans. Lattice boltzmann simulations of liquid-gas and binary fluid systems. *Physical Review E*, 54(5):5041, 1996. [cited at p. 23, 24]

[33] K. A. Brakke. The surface evolver. *Experimental mathematics*, 1(2):141–165, 1992. [cited at p. 24, 25, 52]

[34] A. Brandt. Multi-level adaptive solutions to boundary-value problems. *Mathematics of computation*, 31(138):333–390, 1977. [cited at p. 26]

[35] M. I. Gerritsma. *Time dependent numerical simulations of a viscoelastic fluid on a staggered grid*. University Library Groningen, 1996. [cited at p. 27]

[36] M. P. Bendsøe and O. Sigmund. *Topology optimization: theory, methods, and applications*. Springer Verlag, 2003. [cited at p. 28, 38, 40]

[37] O. Sigmund and K. G. Hougaard. Geometric properties of optimal photonic crystals. *Physical review letters*, 100(15), 2008. [cited at p. 28]

[38] L. H. Olesen, F. Okkels, and H. Bruus. A high-level programming-language implementation of topology optimization applied to steady-state navier–stokes flow. *International Journal for Numerical Methods in Engineering*, 65(7):975–1001, 2006. [cited at p. 28, 41]

[39] K. Svanberg. The method of moving asymptotes: a new method for structural optimization. *International journal for numerical methods in engineering*, 24(2):359–373, 1987. [cited at p. 29, 41]

[40] S. Popinet and S. Zaleski. A front-tracking algorithm for accurate representation of surface tension. *International Journal for Numerical Methods in Fluids*, 30(6):775–793, 1999. [cited at p. 31, 32, 75]

[41] D. M. Anderson, G. B. McFadden, and A. A. Wheeler. Diffuse-interface methods in fluid mechanics. *Annual review of fluid mechanics*, 30(1):139–165, 1998. [cited at p. 31, 34]

[42] M. Muradoglu and S. Tasoglu. A front-tracking method for computational modeling of impact and spreading of viscous droplets on solid walls. *Computers & Fluids*, 39(4):615–625, 2010. [cited at p. 31]

[43] E. B. Dussan. On the spreading of liquids on solid surfaces: static and dynamic contact lines. *Annual Review of Fluid Mechanics*, 11(1):371–400, 1979. [cited at p. 31]

[44] M. R. Swift, W. R. Osborn, and J. M. Yeomans. Lattice boltzmann simulation of nonideal fluids. *Physical Review Letters*, 75(5):830–833, 1995. [cited at p. 31]

[45] F. H. Harlow and J. E. Welch. Numerical calculation of time-dependent viscous incompressible flow of fluid with free surface. *Physics of fluids*, 8:2182, 1965. [cited at p. 32]

[46] J. W. Cahn and J. E. Hilliard. Free energy of a nonuniform system. i. interfacial free energy. *The Journal of Chemical Physics*, 28:258, 1958. [cited at p. 34]

[47] J. W. Cahn. Critical point wetting. *The Journal of Chemical Physics*, 66:3667, 1977. [cited at p. 34]

[48] A. J. Briant, A. J. Wagner, and J. M. Yeomans. Lattice boltzmann simulations of contact line motion. i. liquid-gas systems. *Physical Review E*, 69(3):031602, 2004. [cited at p. 34, 65]

[49] B. Emami, H. V. Tafreshi, M. Gad-el Hak, and G. C. Tepper. Predicting shape and stability of air–water interface on superhydrophobic surfaces with randomly distributed, dissimilar posts. *Applied Physics Letters*, 98(20):203106–203106, 2011. [cited at p. 38, 52]

[50] A. Gersborg-Hansen, M. P. Bendsøe, and O. Sigmund. Topology optimization of heat conduction problems using the finite volume method. *Structural and multidisciplinary optimization*, 31(4):251–259, 2006. [cited at p. 40, 41]

[51] Q. Zheng, C. Lv, P. Hao, and J. Sheridan. Small is beautiful, and dry. *SCIENCE CHINA Physics, Mechanics & Astronomy*, 53(12):2245–2259, 2010. [cited at p. 41]

[52] A. Cavalli, P. Bøggild, and F. Okkels. Parametric optimization of inverse trapezoid oleophobic surfaces. *Langmuir*, 28(50):17545–17551, 2012. [cited at p. 41]

[53] B. S. Lazarov and O. Sigmund. Filters in topology optimization based on helmholtz-type differential equations. *International Journal for Numerical Methods in Engineering*, 86(6):765–781, 2011. [cited at p. 41]

[54] N. K. Andersen. Injection moulding and characterization of self cleaning surfaces. Master's thesis, Technical University of Denmark, Denmark, 2012. [cited at p. 45, 47]

[55] M. Stubenrauch, M. Fischer, C. Kremin, S. Stoebenau, A. Albrecht, and O. Nagel. Black silicon—new functionalities in microsystems. *Journal of Micromechanics and Microengineering*, 16(6):S82, 2006. [cited at p. 46]

[56] T. Deng, K. K. Varanasi, M. Hsu, N. Bhate, C. Keimel, J. Stein, and M. Blohm. Nonwetting of impinging droplets on textured surfaces. *Applied Physics Letters*, 94(13):133109–133109, 2009. [cited at p. 50]

[57] J. A. Dean. Lange's handbook of chemistry. 1985. [cited at p. 51]

[58] M. Nosonovsky. Multiscale roughness and stability of superhydrophobic biomimetic interfaces. *Langmuir*, 23(6):3157–3161, 2007. [cited at p. 51]

[59] Y.-S. Yu and Y.-P. Zhao. Deformation of pdms membrane and microcantilever by a water droplet: Comparison between mooney–rivlin and linear elastic constitutive models. *Journal of colloid and interface science*, 332(2):467–476, 2009. [cited at p. 54]

[60] D. Armani, C. Liu, and N. Aluru. Re-configurable fluid circuits by pdms elastomer micromachining. In *Micro Electro Mechanical Systems, 1999. MEMS'99. Twelfth IEEE International Conference on*, pages 222–227. Ieee, 1999. [cited at p. 54]

[61] J. E. Mark. *Polymer data handbook*. Oxford University Press New York, 2009. [cited at p. 54]

[62] M. Im, H. Im, J.-H. Lee, J.-B. Yoon, and Y.-K. Choi. Analytical modeling and thermodynamic analysis of robust superhydrophobic surfaces with inverse-trapezoidal microstructures. *Langmuir*, 26(22):17389, 2010. [cited at p. 54]

[63] B. Roman and J. Bico. Elasto-capillarity: deforming an elastic structure with a liquid droplet. *Journal of Physics: Condensed Matter*, 22(49):493101, 2010. [cited at p. 60]

[64] M. L. Blow and J. M. Yeomans. Superhydrophobicity on hairy surfaces. *Langmuir*, 26(20):16071–16083, 2010. [cited at p. 60]

[65] Y.-K. Yoon, J.-H. Park, and M. G. Allen. Multidirectional uv lithography for complex 3-d mems structures. *Microelectromechanical Systems, Journal of*, 15(5):1121–1130, 2006. [cited at p. 60]

[66] Y. Chen, B. He, J. Lee, and N. A. Patankar. Anisotropy in the wetting of rough surfaces. *Journal of colloid and interface science*, 281(2):458–464, 2005. [cited at p. 63]

[67] F. Zhang and H. Y. Low. Anisotropic wettability on imprinted hierarchical structures. *Langmuir*, 23(14):7793–7798, 2007. [cited at p. 63]

[68] M. L. Blow and J. M. Yeomans. Anisotropic imbibition on surfaces patterned with polygonal posts. *Philosophical Transactions of the Royal Society A: Mathematical, Physical and Engineering Sciences*, 369(1945):2519–2527, 2011. [cited at p. 63]

[69] M. J. Hancock, K. Sekeroglu, and M. C. Demirel. Bioinspired directional surfaces for adhesion, wetting, and transport. *Advanced Functional Materials*, 22(11):2223–2234, 2012. [cited at p. 63]

[70] C. W. Extrand. Retention forces of a liquid slug in a rough capillary tube with symmetric or asymmetric features. *Langmuir*, 23(4):1867–1871, 2007. [cited at p. 63]

[71] H. Kusumaatmaja and J. M. Yeomans. Anisotropic hysteresis on ratcheted superhydrophobic surfaces. *Soft Matter*, 5(14):2704–2707, 2009. [cited at p. 63, 67]

[72] N. A. Malvadkar, M. J. Hancock, K. Sekeroglu, W. J. Dressick, and M. C. Demirel. An engineered anisotropic nanofilm with unidirectional wetting properties. *Nature Materials*, 9(12):1023–1028, 2010. [cited at p. 64]

[73] M. Barahman and A. M. Lyons. Ratchetlike slip angle anisotropy on printed superhydrophobic surfaces. *Langmuir*, 27(16):9902–9909, 2011. [cited at p. 64]

[74] A. Pringle, S. N. Patek, M. Fischer, J. Stolze, and N. P. Money. The captured launch of a ballistospore. *Mycologia*, 97(4):866–871, 2005. [cited at p. 73]

[75] X. Noblin, S. Yang, and J. Dumais. Surface tension propulsion of fungal spores. *Journal of Experimental Biology*, 212(17):2835–2843, 2009. [cited at p. 73]

[76] J. B. Boreyko and C. H. Chen. Self-propelled dropwise condensate on superhydrophobic surfaces. *Physical review letters*, 103(18):184501, 2009. [cited at p. 73, 75]

[77] K. M. Wisdom, J. A. Watson, X. Qu, F. Liu, G.S. Watson, and C.-H. Chen. Self-cleaning of superhydrophobic surfaces by self-propelled jumping condensate. *Proceedings of the National Academy of Sciences*, 2013. [cited at p. 73]

[78] S. J. Lee, S. Lee, and K. H. Kang. Droplet jumping by electrowetting and its application to the three-dimensional digital microfluidics. *Applied Physics Letters*, 100(8):081604–081604, 2012. [cited at p. 73, 75, 76, 77]

[79] M. Fuentes-Cabrera, B. H. Rhodes, J. D. Fowlkes, A. López-Benzanilla, H. Terrones, M. L. Simpson, and P. D. Rack. Molecular dynamics study of the dewetting of copper on graphite and graphene: Implications for nanoscale self-assembly. *Physical Review E*, 83(4):041603, 2011. [cited at p. 73]

[80] P. D. Rack, Y. Guan, J. D. Fowlkes, A. V. Melechko, and M. L. Simpson. Pulsed laser dewetting of patterned thin metal films: A means of directed assembly. *Applied Physics Letters*, 92(22):223108–223108, 2008. [cited at p. 73]

[81] S. J. Lee, S. Lee, and K. H. Kang. Jumping of a droplet on a superhydrophobic surface in ac electrowetting. *Journal of visualization*, 14(3):259–264, 2011. [cited at p. 73, 75]

[82] B. Darbois Texier, K. Piroird, D. Quéré, and C. Clanet. Inertial collapse of liquid rings. *Journal of Fluid Mechanics*, 717, 2013. [cited at p. 73, 79]

[83] D. L. Brown, R. Cortez, and M. L. Minion. Accurate projection methods for the incompressible navier–stokes equations. *Journal of Computational Physics*, 168(2):464–499, 2001. [cited at p. 75]

[84] R. Xiao, S. C. Maroo, and E. N. Wang. Negative pressures in nanoporous membranes for thin film evaporation. *Applied Physics Letters*, 102(12):123103–123103, 2013. [cited at p. 82]

[85] C. U. Murade, D. van der Ende, and F. Mugele. High speed adaptive liquid microlens array. *Optics express*, 20(16):18180–18187, 2012. [cited at p. 82]

# Appendices

## Appendix A

# Paper 1: Topology Optimization of robust superhydrophobic surfaces

Soft Matter

RSC Publishing

PAPER

View Article Online
View Journal | View Issue

# Topology optimization of robust superhydrophobic surfaces

Cite this: *Soft Matter*, 2013, **9**, 2234

Andrea Cavalli, Peter Bøggild and Fridolin Okkels*

In this paper we apply topology optimization to micro-structured superhydrophobic surfaces for the first time. It has been experimentally observed that a droplet suspended on a brush of micrometric posts shows a high static contact angle and low roll-off angle. To keep the fluid from penetrating the space between the posts, we search for an optimal post cross-section that minimizes the vertical displacement of the liquid–air interface at the base of the drop when a pressure difference is applied. Topology optimisation proves effective in this framework, showing that posts with a branching cross-section are optimal, which is consistent with several biologic strategies to achieve superhydrophobicity. Through a filtering technique, we can also control the characteristic length scale of the optimal design, thus obtaining geometries feasible *via* standard lithography.

Received 25th September 2012
Accepted 6th December 2012

DOI: 10.1039/c2sm27214h

**www.rsc.org/softmatter**



## Introduction

Superhydrophobicity is a remarkable natural phenomenon, recently analysed[1–6] and reproduced artificially[2,7–10] by numerous research groups. Superhydrophobic surfaces show very large static contact angles and small roll-off angles for water, and these properties are usually associated with self-cleaning surfaces.

A micro- and/or nano-scale texture is usually at the origin of superhydrophobicity.[11,12] A drop can reach several different equilibrium states on a textured substrate, as sketched in Fig. 1. The effective minimum energy configuration depends on the chemical and geometrical properties of the liquid–solid interface. We will now focus on superhydrophobicity, which is usually associated with the Cassie–Baxter state.[13] In this configuration, the drop is suspended by the protruding features, so that its base is in contact with a heterogeneous solid–air substrate. The apparent static contact angle $\theta_{CB}$, according to the Cassie–Baxter theory, is given by:

$$\cos\theta_{CB} = f_{sl}\cos\theta_Y - (1 - f_{sl}), \quad (1)$$

a weighted average between the contact angle for the solid substrate ($\theta_Y$) and for air ($\theta_{air} = 180°$), where $f_{sl}$ represents the wetted solid surface per base area of the drop.

If a drop in the Cassie–Baxter state is perturbed, for instance if a pressure difference is applied between the drop and the environment, the liquid–air interface will bulge, and eventually the liquid will begin to flow along the side of the posts when the angle $\theta_{bend}$ (see Fig. 2) exceeds the contact angle $\theta_Y$.

This effect is particularly important for inherently hydrophilic materials, for which a heterogeneous wetting state can be

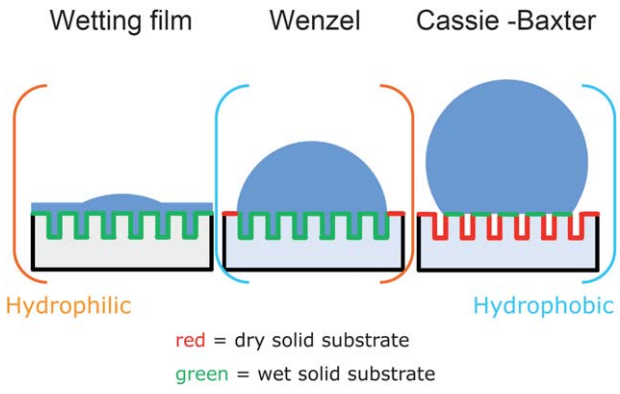


**Fig. 1** Sketch of the possible equilibrium positions of a drop on a textured surface. The states between orange brackets are accessible for hydrophilic materials, and those between blue brackets are accessible for hydrophobic materials.

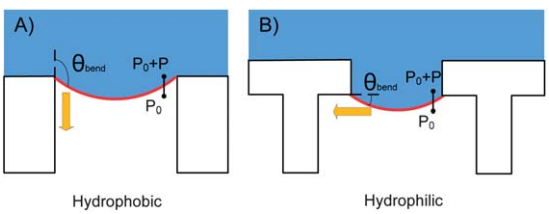


**Fig. 2** (A) Interface deformation under applied pressure, for hydrophobic materials. If $\theta_{bend} > \theta_Y$, the contact line slides along the side of the post, in the direction of the yellow arrow. (B) Analogous setup for hydrophilic materials. If $\theta_{bend} > \theta_Y$, the liquid wets the bottom face of the plate, in the direction of the yellow arrow.

*Department of Micro- and Nanotechnology, Technical University of Denmark, DTU Nanotech, Building 345 East, DK-2800 Kongens Lyngby, Denmark. E-mail: fridolin.okkels@nanotech.dtu.dk*

achieved through overhanging structures (see Fig. 2B), even if the global energy minimum will be a Wenzel state[7] (Fig. 1). Maximising the robustness of the suspended drop configuration upon applied pressure is therefore fundamental for effective superhydrophobic surfaces.

The research about "Cassie mode" superhydrophobicity has so far been characterized by a strong dichotomy. On the one hand, complex hierarchical structures have been fabricated and tested experimentally, but their modelling is difficult, since the structures are usually rough and non-periodic.[14] On the other hand, there is an active research for the optimal post shape to achieve a robust Cassie state, which however usually relies on simple shape perturbations to conventional cylindrical or square posts. In this paper, we take a step in bridging this gap, applying the tools of topology optimization.

Topology optimization[15] is a structural optimization method with no intrinsic constraint on the topology of the solution, which has been applied in such different fields as structural mechanics,[15] photonic crystal design[16] and microfluidic devices.[17] We will here apply it to obtain the texture that minimizes the deformation of the liquid–air interface under applied pressure, thus making the suspended state as robust as possible. We will see that this approach generates interesting branching structures, which resemble natural and experimentally tested superhydrophobic structures. However, the symmetry and length scale of the optimal design can be tuned in the numeric optimization procedure, leading to a better understanding and control of such features.

## Modelling and numeric setup

In this work we will restrict our analysis to a unit cell for a square array of posts (Fig. 3), neglecting finite size effects at the edge of the drop. We will consider a two-dimensional picture, in which the liquid–air interface is flat and suspended on top of the posts ($z = 0$) in the unperturbed configuration, and bulges between the posts to a depth $S(\vec{x})$ upon applying a pressure difference $\Delta P$. Such a pressure difference across the liquid–air interface can arise for different reasons, such as the Laplace pressure, due to the drop curvature or the pressure upon impact of a drop on the substrate. We also introduce non-dimensional units for length $l$, surface tension $\sigma$ and pressure $P$ as follows:

$$\begin{aligned} \sigma &= \sigma_0 \bar{\sigma}, \\ l &= L_0 \bar{l}, \\ P &= \frac{\sigma_0}{L_0} \bar{P} = P_0 \bar{P}. \end{aligned} \tag{2}$$

Here $L_0$ is the characteristic length of the system, which we will take as the side of the unit cell (typically few μm), and $\sigma_0$ can be taken as the surface tension of the liquid considered (72.9 mJ m$^{-2}$ for water at 20 °C). Moreover, since typically $L_0 \ll l_c = \sqrt{\frac{\sigma}{\rho g}}$, where $l_c$ is the capillary length for the liquid considered, we can neglect gravity.

Let us first consider a simple geometry, such as a cylindrical post (cross-section is shown in Fig. 3B). The deflection of the liquid–air interface among posts can then be described by the Young–Laplace equation[18]

$$\begin{cases} \nabla \cdot \left( \dfrac{\nabla S(\vec{x})}{\left|\nabla S(\vec{x})\right|} \right) = \Delta P & \text{on } D \\ S(\vec{x}) = 0 & \text{on } \partial D_1 \\ \nabla S(\vec{x}) \cdot \vec{n} = 0 & \text{on } \partial D_2. \end{cases} \tag{3}$$

A Dirichlet boundary condition $S(\vec{x}) = 0$ is used at the boundary of the solid structure $\partial D_1$ to represent the interface being pinned on the ridge of the post. A Von Neumann condition $\nabla S(\vec{x}) \cdot \vec{n} = 0$ is applied on the boundary of the unit cell $\partial D_2$ to account for the symmetry of the post array (in the following, we will also exploit the symmetry of the cell to work only on one-eighth of the domain).

For the optimization procedure, we will now slightly modify this setup. We still consider a "solid" support ($S(\vec{x}) = 0$, red dot in Fig. 3C) in the centre of the domain, but now the post cross-section is allowed to change around it, in order to provide an optimal support for the interface. The distribution of the material at point $\vec{x}$ inside the cell is described by the design variable $\gamma(\vec{x})$, a scalar field which ranges from 0 (completely solid) to 1 (completely empty) through intermediate values.

The field $\gamma(\vec{x})$ will be coupled with eqn (3), leading to the following formulation of the problem:

$$\begin{cases} \nabla \cdot \left( K(\gamma) \dfrac{\nabla S(\vec{x})}{\left|\nabla S(\vec{x})\right|} \right) = \Delta P & \text{on } D \\ S(\vec{x}) = 0 & \text{on } \partial D_1 \\ \nabla S(\vec{x}) \cdot \vec{n} = 0 & \text{on } \partial D_2. \end{cases} \tag{4}$$

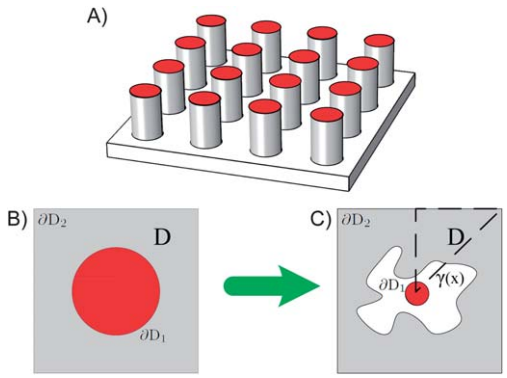


**Fig. 3** (A) Sketch of the considered post array. (B) Top view of a single post cell, for the basic circular cross-section. The domain D and boundaries $\partial D_1$ and $\partial D_2$ from eqn (3) are also shown. (C) Same view of a single cell, with a variable cross-section (white area) around a fixed "nucleus" (red dot). In the topology optimization procedure, the cross-section is not fixed but varies according to the field $\gamma(\vec{x})$. The dashed line in (C) shows the reduced computation domain that exploits the symmetry of the cell.

where $K(\gamma)$ is defined as:

$$K(\gamma) = 1 + \frac{(K_{\max} - 1)q(1-\gamma)}{(q+\gamma)} \quad (5)$$

Given the form of eqn (4) and (5), it is possible to understand the effect of the design variable $\gamma(\vec{x})$ on the solution $S(\vec{x})$. Where $\gamma(\vec{x}) = 0$, $K(\gamma)$ is equal to $K_{\max}$, which is fixed to be a large value. The value $\Delta P$ on the right side of eqn (4) then becomes negligible, and the liquid–air interface $S(\vec{x})$ does not deform significantly. We therefore recover the "solid" condition $S(\vec{x}) \simeq 0$. On the other hand, if $\gamma(\vec{x}) = 1$ ("empty space"), $K(\gamma) = 1$, and we recover the Young–Laplace equation out of the support of the post, as in eqn (3). Intermediate values of $K(\gamma)$ do not have a direct physical interpretation, but are required for a smooth optimization procedure. The interpolation between these two extreme ranges is controlled by the parameter $q$ in eqn (5). By choosing a sufficiently small value (through testing we found that $10^{-4}$ gives a reliable result), it is possible to drive the optimization procedure to give a well defined "solid-empty" binary design.[15] This formulation also resembles a 2D optimal heat conduction problem, where $K(\gamma)$ corresponds to the distribution of the conducting material.[19]

We eventually need to define an objective function, *i.e.* a quantity whose minimization with respect to $\gamma(\vec{x})$ will maximise the support to the liquid–air interface. We choose this quantity, called $\Phi[S(\vec{x}),\gamma(\vec{x}),\Delta P]$, to be the squared integral displacement of the interface (for a given pressure difference $\Delta P$ and material distribution $\gamma(\vec{x})$):

$$\Phi\left[S(\vec{x}),\gamma(\vec{x}),\Delta P\right] = \int_D S^2(\vec{x})\,\mathrm{d}A. \quad (6)$$

With this choice, we do not control directly the angle between the interface and the side of the post, which is indeed what would trigger the penetration of the liquid among posts. However, eqn (6) is easy to evaluate through the optimization procedure, and its minimization naturally constrains the maximum bending angle of the interface,[20] although there might be fluctuations along the post ridge.

At every iteration, the topology optimization code changes the value of $\gamma(\vec{x})$ over the domain and evaluates $\Phi[S(\vec{x}),\gamma(\vec{x}),\Delta P]$ and the sensitivity $\delta\Phi/\delta\gamma(\vec{x})$. We then use this information as input to find the configuration of $\gamma(\vec{x})$ that minimizes the objective function $\Phi$, using the method of moving asymptotes (MMA).[21] Details on the sensitivity analysis and the implementation of the code can be found in the paper by Olesen *et al.*[17] We will also introduce a constraint on the maximum solid fraction per unit cell as:

$$\int_D 1 - \gamma(\vec{x})\,\mathrm{d}A \leq f_{\mathrm{sl}}. \quad (7)$$

Remembering the Cassie–Baxter relation $\cos\theta_{\mathrm{CB}} = f_{\mathrm{sl}}\cos\theta_{\mathrm{Y}} - (1 - f_{\mathrm{sl}})$, eqn (7) can conveniently be interpreted as a constraint on the static contact angle shown by a surface patterned in this way.

The specific coupling $K(\gamma)$ we use in eqn (4) will generate a structure connected to the boundary $\partial D_1$, which "radiates" the support to the $\gamma \simeq 0$ regions.[19] This effectively makes our analysis a shape optimization with many degrees of freedom, while the general topology optimization routine we use could as easily generate disconnected topologies.

There are a few reasons for the choice of the connected design. First, it is well known that dense and thin posts, ideally down to the nanometer scale, offer increasingly better support to drops in the Cassie–Baxter state.[2,22] However, it is perhaps more interesting to optimize the shape of a *single* texture element, which can then be scaled up or down in size according to fabrication and performance constraints. Second, if we are interested in obtaining a hydrophobic behaviour from hydrophilic materials, overhanging structures are required. In this perspective, the central support in our optimisation can be considered as the stem of the post (see Fig. 2), while we effectively optimise the cross-section of the top plate. Eventually, we argue that our branching structures would show higher mechanical robustness than hair-like features, in particular to buckling and shear loads. This latter property is of great relevance for practical fabrication purposes, since most practical applications would include significant stresses for the substrates.[23]

A final remark regards the length scales in the optimal design: at every iteration in the optimisation routine we calculate a smoothed version $\tilde{\gamma}(\vec{x})$ of the design variable $\gamma(\vec{x})$, applying a diffusion step:[24]

$$L_{\mathrm{diff}}{}^2\nabla^2\tilde{\gamma}(\vec{x}) = \tilde{\gamma}(\vec{x}) - \gamma(\vec{x}). \quad (8)$$

While calculating the sensitivity, $\tilde{\gamma}(\vec{x})$ is then used. This process allows us to control the minimum size of the features appearing in the optimal design. As we will discuss in the next section, without filtering small length scale features would appear in the optimal design, ideally down to the mesh scale. However, these small solid features surrounded by empty space are transformed by the diffusion step in a homogeneous area with an intermediate $\gamma(\vec{x})$ value, and thus are penalized by the $K(\gamma)$ function, which favours a binary solid–empty solution. The main advantage of this technique is its formulation in terms of a partial differential equation, which relies on the same numeric tools used for eqn (4).

The actual implementation of our optimization routine uses a Matlab code that relies on the commercial software COMSOL to solve the partial differential equations at every iteration step.

## Discussion of optimized designs

In the following, the pressure difference acting on the interface has been fixed as $\Delta P = P_0$. In Fig. 4 we compare the performance of a cylindrical post (A) and an optimized design (C) inside a unit cell. The surface plots displayed on the right (B and D) show the vertical displacement $S(\vec{x})$ obtained through eqn (3). For both structures, the solid fraction is $f_{\mathrm{sl}} = 0.25$. It is easy to see the enhanced performance of the topology optimized structure, with the mean displacement reduced by a factor of 10. It is clear that the branching in the optimal structure increases the length of the contact line, where the surface tension acts on

 

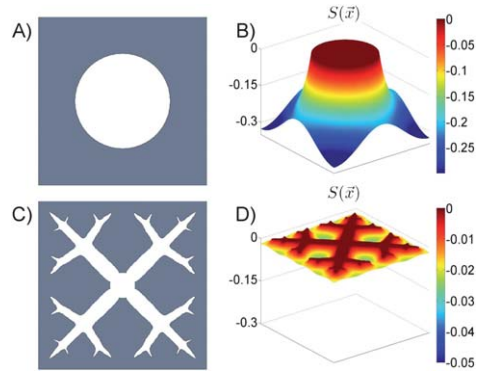


**Fig. 4** (A) Top view of a cylindrical post with a solid fraction $f_{sl} = 0.25$. (B) Displacement plot for applied pressure $\Delta P = P_0$. (C) Optimized material distribution with a solid fraction $f_{sl} = 0.25$. (D) Displacement plot for the topology optimized design.

the side of the post to balance the effect of the applied pressure difference. This results in a reduction of the interface deformation. However, we think that just choosing a meandering cross-section would not improve the performance dramatically. Lobaton and Salamon,[20] for instance, considered a simpler sinusoidal perturbation to a circular cross-section. While significantly increasing the contact line length, such a shape modification showed modest improvement in the critical pressure value. The added feature of our optimal designs is the convenient placement of the branches that adjust to the cell shape (here a square unit cell; however analogous solutions have been tested for hexagonal lattices) to reduce the size of the gaps between solid features. We therefore argue that the significant reduction in the surface displacement arises from the interplay of optimal location of the main branches and increased contact line length coming from the secondary branches.

This physical picture makes it easy to understand the effect of the filtering length $L_{diff}$ on the optimal design. The designs shown in the upper row of Fig. 5 were obtained by solving for the domain shown in the bottom row. The yellow dots have a radius equal to $L_{diff}$.

It can be seen that, for any value of $L_{diff}$, the structure branches along the diagonals of the square cell, thus filling the largest gap between two posts. If the resolution is sufficiently fine, further branching appears, with new branches filling the gap among the diagonals. The process continues for even smaller length scales and we get an overall quasi-fractal behaviour.

It is possible to see how the filtering procedure constrains the minimal length scale in the optimal design. This allows us to obtain structures suitable for fabrication, *i.e.* with a feasible amount of branching.

These fractal-like structures resemble several biological surfaces, such as the lotus leaf, which use analogous (although three-dimensional) multi-scale structures to achieve their superhydrophobic properties. Although our optimization is two dimensional, it is possible to complement the suggestions from topology optimization with general knowledge from superhydrophobic surfaces, to get an even more effective texture. Indeed, most artificial and natural superhydrophobic surfaces are characterized by a micron scale texture with superimposed nanometric roughness. The cross-sections shown here should be considered an optimal micron scale pattern, over which nano-grass features can be grown, thus achieving a multi-layer support for the interface (this procedure is currently being considered in collaboration with Nis K. Andersen and Rafael Taboryski at DTU Nanotech, and will be the subject of a future publication).

In Fig. 6, we eventually analyse the dependence of the mean interface displacement $\langle s \rangle = \sqrt{\frac{1}{D}\int_D S^2(\vec{x})\mathrm{d}A}$ on the solid fraction $f_{sl}$ for a fixed filter length $L_{diff} = 0.75\ h_{mesh}$, where $h_{mesh}$ is the characteristic mesh size. An increasing branching for a larger solid fraction is clearly seen in the optimal designs, which results in a better support for the interface. In the chart we compare the mean displacement for the optimal design to the displacement for a post of circular cross-section and same $f_{sl}$.

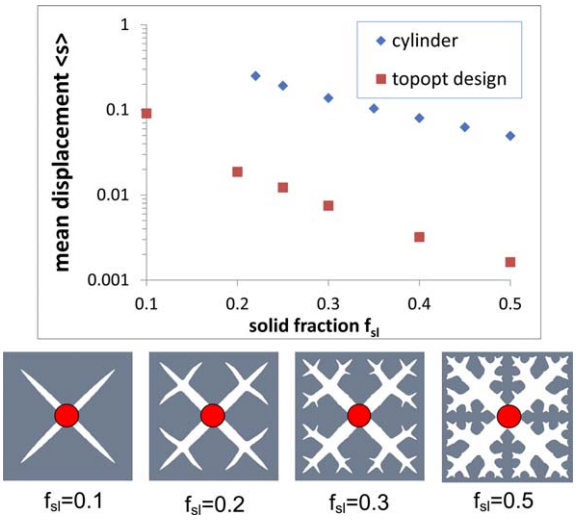


**Fig. 6** Optimal designs as a function of solid fraction $f_{sl}$. The red dot represents the fixed support in the optimisation procedure. In the chart, the mean vertical displacement of the liquid–air interface is compared for cylindrical posts and topology optimised ones.

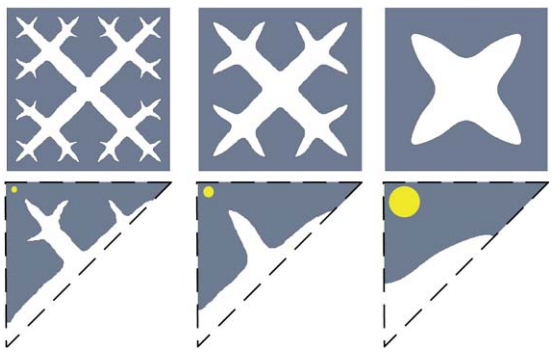

**Fig. 5** Optimal design for $f_{sl} = 0.3$ and $L_{diff} = 0.5$, 1, 3 times the mesh size $h_{mesh}$. The radius of the yellow dot in each column is equal to $L_{diff}$.

We can see that the optimised design always performs better than the simple circular cross-section, and even more so for large solid fractions, which is again a consequence of the higher degree of branching in the optimised configuration.

## Conclusion and outlook

In this paper we applied topology optimisation for the stability of superhydrophobic surfaces. We found that this technique is very effective for the task. Branching structures are found to be optimal to support hydrostatic pressure for a Cassie–Baxter state, in a two-dimensional analogy to natural structures. We also analysed the effect of a solid fraction constraint on the optimal design, as well as the use of a PDE filter to obtain designs suitable for fabrication. Further work will include the fabrication and characterization of such optimised micro-textured surfaces. Preliminary fabrication results obtained at DTU Nanotech suggest that the optimal shapes can be reproduced with a high degree of precision using common lithographic techniques. A further step will be to use a cost-effective procedure, such as injection moulding, to produce the same designs.

## Acknowledgements

This research is funded by the NanoVation consortium. The authors thank Kristian E. Jensen, Nis K. Andersen and Rafael J. Taboryski for useful suggestions and discussions. They also thank David Mackenzie for proofreading the final draft.

## References

1 A. Marmur, *Langmuir*, 2008, **24**, 7573–7579.
2 P. G. De Gennes, F. Brochard-Wyart and D. Quéré, *Capillarity and wetting phenomena: drops, bubbles, pearls, waves*, Springer, 2003.
3 M. Nosonovsky, *Langmuir*, 2007, **23**, 3157–3161.
4 G. McHale, *Langmuir*, 2007, **23**, 8200–8205.
5 N. A. Patankar, *Langmuir*, 2004, **20**, 7097–7102.
6 H. Kusumaatmaja, M. L. Blow, A. Dupuis and J. M. Yeomans, *EPL*, 2008, **81**, 36003.
7 A. Tuteja, W. Choi, J. M. Mabry, G. H. McKinley and R. E. Cohen, *Proc. Natl. Acad. Sci. U. S. A.*, 2008, **105**, 18200.
8 J. Bico, C. Marzolin and D. Quéré, *Europhys. Lett.*, 1999, **47**, 220.
9 J. Bico, U. Thiele and D. Quéré, *Colloids Surf., A*, 2002, **206**, 41–46.
10 C. W. Extrand and Y. Kumagai, *J. Colloid Interface Sci.*, 1995, **170**, 515–521.
11 E. Bormashenko, Y. Bormashenko, T. Stein, G. Whyman and E. Bormashenko, *J. Colloid Interface Sci.*, 2007, **311**, 212–216.
12 L. Gao and T. J. McCarthy, *Langmuir*, 2009, **25**, 14105–14115.
13 A. B. D. Cassie and S. Baxter, *Trans. Faraday Soc.*, 1944, **40**, 546–551.
14 B. Emami, H. V. Tafreshi, M. Gad-el Hak and G. C. Tepper, *Appl. Phys. Lett.*, 2011, **98**, 203106.
15 M. P. Bendsøe and O. Sigmund, *Topology optimization: theory, methods, and applications*, Springer Verlag, 2003.
16 O. Sigmund and K. G. Hougaard, *Phys. Rev. Lett.*, 2008, **100**, 153904.1–153904.4.
17 L. H. Olesen, F. Okkels and H. Bruus, *Int. J. Numer. Methods Eng.*, 2006, **65**, 975–1001.
18 Q. S. Zheng, Y. Yu and Z. Zhao, *Langmuir*, 2005, **21**, 12207–12212.
19 A. Gersborg-Hansen, M. P. Bendsøe and O. Sigmund, *Structural and Multidisciplinary Optimization*, 2006, **31**, 251–259.
20 E. J. Lobaton and T. R. Salamon, *J. Colloid Interface Sci.*, 2007, **314**, 184–198.
21 K. Svanberg, *Int. J. Numer. Methods Eng.*, 1987, **24**, 359–373.
22 Q. Zheng, C. Lv, P. Hao and J. Sheridan, *Sci. China: Phys., Mech. Astron.*, 2010, **53**, 2245–2259.
23 A. Cavalli, P. Boggild and F. Okkels, *Langmuir*, 2012, 17545–17551.
24 B. S. Lazarov and O. Sigmund, *Int. J. Numer. Methods Eng.*, 2011, **86**, 765–781.



 

## Appendix B

# Paper 2: Parametric Optimization of Inverse Trapezoid Oleophobic Surfaces

Langmuir

Article

pubs.acs.org/Langmuir

# Parametric Optimization of Inverse Trapezoid Oleophobic Surfaces

Andrea Cavalli,* Peter Bøggild, and Fridolin Okkels*

Department of Micro- and Nanotechnology, Technical University of Denmark, DTU Nanotech, Building 345 East, DK-2800 Kongens Lyngby, Denmark

Supporting Information

**ABSTRACT:** In this paper, we introduce a comprehensive and versatile approach to the parametric shape optimization of oleophobic surfaces. We evaluate the performance of inverse trapezoid microstructures in terms of three objective parameters: apparent contact angle, maximum sustainable hydrostatic pressure, and mechanical robustness (Im, M. ; Im, H: ; Lee, J.H. ; Yoon, J.B. ; Choi, Y.K. A robust superhydrophobic and superoleophobic surface with inverse-trapezoidal microstructures on a large transparent flexible substrate. *Soft Matter* **2010**, *6*, 1401−1404; Im, M. ; Im, H: ; Lee, J.H. ; Yoon, J.B. ; Choi, Y.K. Analytical Modeling and Thermodynamic Analysis of Robust Superhydrophobic Surfaces with Inverse-Trapezoidal Microstructures. *Langmuir* **2010**, *26*, 17389−17397). We find that each of these parameters, if considered alone, would give trivial optima, while their interplay provides a well-defined optimal shape and aspect ratio. The inclusion of mechanical robustness in combination with conventional performance characteristics favors solutions relevant for practical applications, as mechanical stability is a critical issue not often addressed in idealized models.

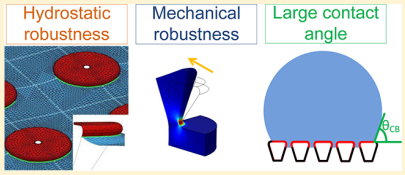


## 1. INTRODUCTION

In recent years, Nature has inspired several microstructures with fascinating wetting properties. Superhydrophobicity,[3] controlled spreading,[4] and unidirectional droplet motion[5,6] have been experimentally reported, taking inspiration from such diverse systems as Lotus leaves and the wings of butterflies. Recently, numerous studies have analyzed hydrophobic surfaces obtained from hydrophilic materials through micropatterning, both experimentally (Tuteja et al.,[7] Im et al.[1]) and theoretically (Marmur,[8] Nosonovsky,[9] Lobaton and Salamon[10]). This problem can be directly related to the realization of oleophobic surfaces, that is, surfaces where low surface tension fluids (like oils) show a Young contact angle larger than 90°. As a matter of fact, smooth surfaces of most materials are oleophilic and chemical coatings usually do not affect the surface energy enough to impart oleophobicity. Micropattering is then essential to obtain oleophobicity, since a micrometer-sized texture allows novel wetting states with respect to a smooth substrate.

As is sketched in Figure 1, there are many possible equilibrium configurations for a droplet on a textured substrate, depending on the chemical and geometrical properties of the surface. Here we focus on the Cassie−Baxter regime, where the liquid is suspended on the surface protrusions, so that the drop sits on a mixed solid−air substrate. In this case, the expected static contact angle $\theta_{CB}$ is a microscopic average between the contact angle with the solid surface ($\theta_Y$) and the one with air (i.e., 180°).

The two angles are weighted with the fraction of the base area of the drop in contact with the substrate ($f_{sl}$) and with air ($f_{gl}$), so we get the relation

$$\cos\theta_{CB} = f_{sl}\cos\theta_Y - f_{gl} \tag{1}$$

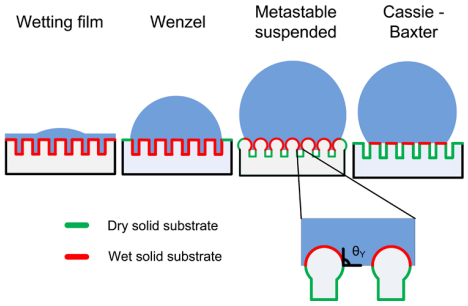


**Figure 1.** Sketch of the possible equilibrium positions for a droplet on a textured surface. The inset shows a magnification of the idealized liquid−gas interface for the metastable configuration.

As seen from this equation, for a proper choice of $f_{gl}$ and $f_{sl}$, a hydrophilic surface could show hydrophobic or even superhydrophobic behavior if it was able to sustain such a composite interface. However, an energetic argument shows that a suspended Cassie−Baxter interface will never be a global energy minimum for hydrophilic substrates. In fact, a suspended configuration is only energetically favorable if (De Gennes[3])

$$\cos\theta_Y \le \frac{-f_{gl}}{r - f_{sl}} \tag{2}$$

where $r$ is the roughness of the surface, defined as the ratio of the effective area below a drop to the base area of the drop. Since the right side of eq 2 is always negative, the inequality is never satisfied for hydrophilic materials ($\cos\theta_Y > 0$).

**Received:** April 13, 2012
**Published:** October 18, 2012

Nevertheless, *local* energy minima, corresponding to a suspended solid−air interface, are possible, and thus a microscale texture can still convert a hydrophilic substrate into a metastable hydrophobic or even superhydrophobic one.[11] This local energy minimum can be attained using an overhanging texture, so that in equilibrium the local contact angle matches the Young contact angle inside the protrusions (see inset in Figure 1). Since this equilibrium is not a global energy minimum, its stability against perturbations, such as an applied external pressure, must be carefully tested. In this paper, we will describe a novel optimization approach, that takes into account three different properties of candidate oleophobic microstructures. These are (a) the apparent or macroscopic contact angle shown by drops on the texture, (b) the maximum hydrostatic pressure the liquid−air interface can sustain while being in the suspended state, and (c) the mechanical robustness of the microstructures. We will show how the interplay of these objective parameters is essential in defining an optimal oloephobic structure. As a test geometry, we will consider inverse trapezoids as those realized by Im et al. in refs 1 and 2 and shown in Figure 2. These structures have been shown to be

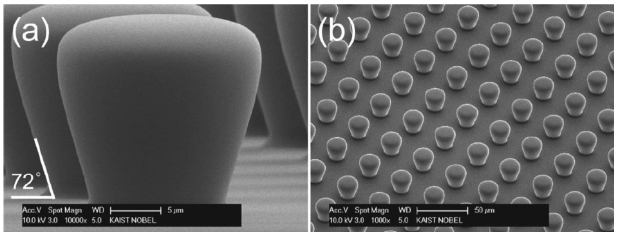


**Figure 2.** SEM image of a single PDMS inverse trapezoid (a) and an array of them (b) from Im et al. Reprinted with permission from ref 2. Copyright 2010 American Chemical Society.

realizable in a wide range of aspect ratios with high regularity, combining PDMS replication procedures and backside 3D diffuser lithography.

## 2. MODELING AND SETUP

From now on, we will consider a drop sitting on a square array of inverse trapezoid posts, as can be seen in Figure 2 and later in Figure 6. A complete description of a drop on a textured surface is a rather delicate task, that could include dynamics effects and several length and time scales.[19] Some relevant features of such a system can however be explained in terms of simpler static considerations. First of all, we will describe the liquid−air interface on the textured substrate, defining a model to assess the capillary stability of the suspended Cassie−Baxter configuration. We will then consider the mechanical robustness of the microstructures, using linear elasticity theory. To generalize the scope of the analysis, we introduce normalized surface tensions, lengths, and pressure as follows:

$$\gamma_{ij} = \gamma_0 \bar{\gamma}_{ij}, \quad l = L_0 \bar{l}, \quad P = P_0 \bar{P} \tag{3}$$

where $\gamma_0$ will be the liquid−air surface tension for the considered liquid, for instance, $\gamma_0 = 21.7$ mN/m at 19°C for octane.[18] $L_0$ will be a characteristic length for the texture, and we choose it to be $L_0 = 5$ $\mu$m, which is consistent with experimental studies.[1,7] $P_0$ can be related via the Young−Laplace equation to the other quantities, so $P_0 = \gamma_0/L_0 = 4.34 \times 10^3$ N/m$^2$.

**2.1. Wetting Analysis: Energetic Considerations and Failure Modes.** If we neglect effects due to the finite size of the drop (i.e., the drop radius is much larger than the texture size), we can restrict our analysis to a unit cell of the texture, exploiting the periodicity of the system. We will also forget about gravitational effects; this assumption is valid if the drop size is smaller than the associated capillary length $\lambda_c = (\gamma/\rho g)^{1/2}$, where $\gamma$ is the liquid−air surface tension, $\rho$ is the fluid density, and $g$ is the gravitational acceleration.

As shown by several authors,[8,9] a drop on a microtexture finds a local energy minimum if the local contact angle $\theta_{loc}$ with the solid wall equates the Young contact angle $\theta_Y$, that is,

$$\cos\theta_{loc} = \cos\theta_Y \tag{4}$$

Furthermore, it can be shown[8,9] that this equilibrium will be stable for infinitesimal displacements if the profile of the pillars/trenches is convex; that is, the center of curvature is inside the solid phase. These conditions then put a first set of constraints on the candidate profiles for an oleophobic texture.

In any case, a transition to a fully wetted configuration is still possible under applied pressure at the liquid−air interface. Tuteja et al.[7] have underlined the relevance of two failure mechanisms for such overhanging structures. If $\theta_{loc}$ exceeds $\theta_Y$, the contact line will slide along the pillars' side, eventually wetting the base of the microstructures (this failure mode is termed "angle" or "T*-failure" in Tuteja et al.[7] and is shown in Figure 3A). Alternatively, the liquid−air

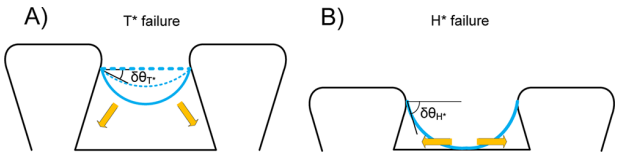


**Figure 3.** Two-dimensional sketch of the possible failure modes for a suspended configuration, with relevant geometric parameters shown. (A) T*-failure: the local contact angle gets too large for equilibrium, and the fluid slides on the side of the post. (B) H*-failure: the bending liquid−air interface touches the bottom of the texture, leading to full wetting.

interface could bend enough for the meniscus to touch the bottom of the texture, triggering a transition to a fully wetted state. This process is termed "height" or "H*-failure" in Tuteja et al.[7] and is shown in Figure 3B).

The critical pressure triggering either failure mode can be obtained analytically for two-dimensional structures, as shown in the Supporting Information. Alternatively, a numerical simulation can be used to predict the shape of the interface under applied pressure and therefore the onset of the failure mode. We carried out such simulation using the software Surface Evolver, as discussed in the next section.

**2.2. Surface Evolver Setup.** Although it is possible to get an approximate description of the liquid−air interface on textured surfaces, an exact analytic solution is often not available, and numerical modeling is therefore required to account for specific geometries. Some authors (Lobaton and ,[10] Zeng et al.,[12] Emami et al.[13]) have already considered the static problem of a liquid−air interface under applied pressure. However, Zheng et al.[12] consider already hydrophobic materials, while Lobaton and Salamon[10] assume sharp corners that pin the contact line. Our numerical model will instead be fully three-dimensional, thus allowing the sliding of the contact line along the side of the pillar structures. Our simulation has been realized using Surface Evolver (SE),[14] a C-like environment for drop and interface simulation. The interface is described by a triangular mesh, with an energy function associated to every facet. The free surface of the fluid is initialized with a coarse polygon, and then refined and relaxed according to an energy minimization algorithm. The boundary vertices are constrained to move on a two-dimensional manifold, representing the post. Since the evolution is generated with a gradient-descent algorithm, the transient dynamics of the simulation do not include inertial effects. However, the equilibria found this way coincide with the physical ones. Let us consider a unit cell of the texture. The total energy $G$ of the system can be expressed as


dx.doi.org/10.1021/la303853g | Langmuir 2012, 28, 17545−17551

$$G = \gamma_{ls}A_{ls} + \gamma_{lg}A_{lg} + \gamma_{sg}A_{sg} + PV \quad (5)$$

Here $V$ is the liquid volume inside the unit cell and $P$ is the prescribed pressure difference across the interface, while ($\gamma_{gl}$, $\gamma_{gs}$, $\gamma_{ls}$) and ($A_{gl}$, $A_{gs}$, $A_{ls}$) are the surface tensions and contact surfaces per unit cell between gas and liquid phase, gas and solid phase, solid and liquid phase, respectively. Since the solid area per unit cell has a finite extent, we can introduce its value $A_{tot}$, so that $A_{sg} = A_{tot} - A_{ls}$. Constant terms in the energy expression will not contribute to the minimization, so we can discard $A_{tot}$. Remembering the definition of Young contact angle $\cos\theta_Y = (\gamma_{sg} - \gamma_{sl})/\gamma_{lg}$ and eq 3, the nondimensional energy expression to be minimized becomes

$$G = \gamma_{lg}\left[A_{lg} - \cos\theta_Y A_{ls}\right] + PV \quad (6)$$

In eq 6, different weights for liquid−air and liquid−solid interfaces appear, with the latter weight being positive or negative according to the Young contact angle. It can also be seen that the solid−air interface does not appear explicitly in the relation, and therefore, the liquid meniscus can be modeled taking into account only $A_{gl}$ and $A_{ls}$. The standard Surface Evolver evolution takes downhill steps according to the provided energy function eq 6. Each vertex in the simulation is acted upon by a force depending on how much its displacement affects the surface area (through the surface tension) or the liquid volume (through the prescribed pressure). Details on the implementation can be found in the software manual.[14] A typical Surface Evolver setup is shown in Figure 4. In order to find the maximum hydrostatic pressure

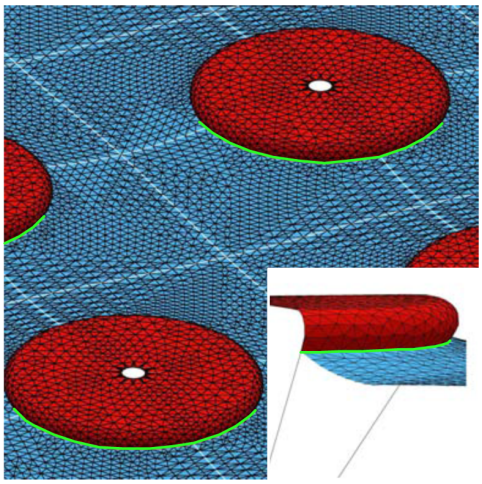

**Figure 4.** Top view of the inverse trapezoid array inside Surface Evolver. The red facets represent the wetted solid surface, while the blue facets are the liquid−air interface. The contact line is colored green. Inset: close up of the computation domain, where the curvature of the liquid−air interface is visible.

for which a suspended state can be supported by the posts, we run successive simulations with increasing applied pressure difference $P$. While we increase the pressure, the interface slides along the post side to satisfy the contact angle condition eq 4 and bulges to match Young Laplace equation $P = \gamma\kappa$, that relates the pressure difference across the interface $P$ to the surface mean curvature $\kappa$. The breakthrough pressure is then reached when the interface slides all the way along the post side to the base of the simulation box (T*-failure) or touches the base of the domain while bulging (H*-failure). Details of the calculation of the breakthrough pressure can be found in the Supporting Information.

**2.3. Mechanical Robustness Modeling.** A novel element in our optimality analysis will be an assessment of the mechanical robustness of the microtexture posts. Oleophobic microstructuring can find application in multiple fields, ranging from lab on a chip devices to food processing, where the integrity of the surface functionality will be compromised as smaller or larger areas are damaged; even minor changes of the surface may lead to pinning, contamination, and ultimately functional failure. While of key importance for any practical application, such issues are rarely addressed. The lifetime of any structure based on overhanging microstructures will benefit if the surface is able to support different kinds of mechanical stresses. We therefore perform a linear elasticity analysis to constrain feasible geometries, using the commercial software COMSOL. We especially focused on a shear load acting on the top face of the structures, since this would generate large stresses at the neck of the trapezoids and address a range of common situations encountered for instance during mechanical cleaning or other intended use of oleophobic surfaces. The equations solved are then, using tensor notation:

$$\begin{cases} \sigma_{ij,j} = 0 & \text{on } D \\ \sigma_{ij}n_j = \tau_i & \text{on } \partial D \end{cases} \quad (7)$$

where $\sigma_{ij}$ is the Cauchy stress tensor, $\tau_i$ is a boundary load, $D$ represents the post's volume, and $\partial D$ its boundary. The material considered in the simulation is a PDMS (polydimethylsiloxane) elastomer, corresponding to the structures described by Im et al.[1] In their experiment, the PDMS trapezoids are realized on a substrate of the same material.

The modeling and failure analysis of elastomers is a complex topic, since their response to stress changes dramatically depending on parameters such as their composition, curing, and temperature. Their ability to stretch several time their original size is usually described in terms of hyperelastic models, such as Mooney−Rivlin's. In the limit of small deformations, however, we recover a linear elastic response.[17] In this work, we will therefore limit ourselves to this regime, which can already give an useful insight into the dependence of the mechanical properties of the posts on their shape and aspect ratio. The relevant material parameters we will use are then the Young's modulus $Y = 6 \times 10^5$ Pa and Poisson ratio $\nu = 0.49$.[15,16]

Using a symmetric boundary condition along the direction of the load allows us to model only half of the structure. Moreover, given the linearity of our model, we can use an antisymmetric boundary condition on the plane passing through the center of the structure perpendicular to the load direction (see Figure 5) and thus solve only for a quarter of the structure. Figure 5 shows the computational domain and a typical mesh of $n \simeq 35\,000$ elements used in the calculations.

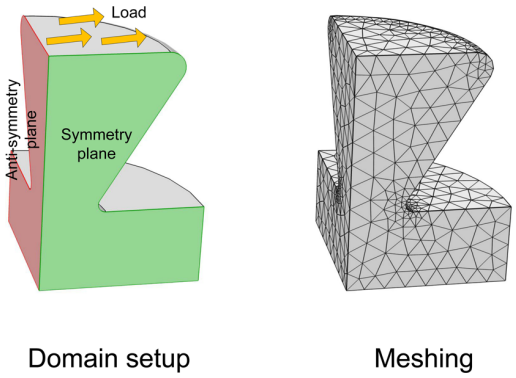


**Figure 5.** Typical domain and mesh used for stress calculation, using the commercial software Comsol 4.2.

## 3. DESIGN VARIABLES AND OBJECTIVE PARAMETERS

Having described the relevant physical properties of the liquid−solid interaction, we can now proceed to define the optimization parameters. As stated before, we optimize axially symmetric inverse trapezoid structures, which can be parametrized in terms of the design variables top radius $b$, base radius $a$, and height $h$ (see Figure 6). Another useful parameter can be the side angle $\theta_{side} = \arctan((b-a)/$


dx.doi.org/10.1021/la303853g | Langmuir 2012, 28, 17545−17551

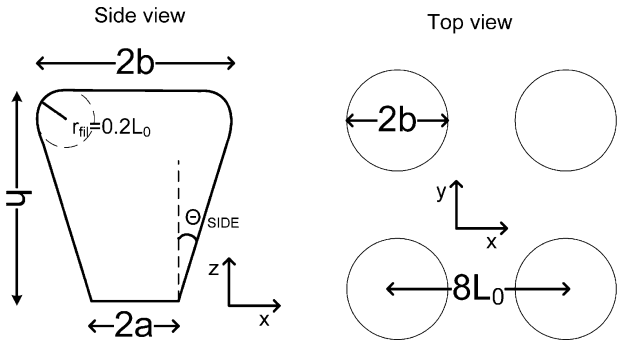


**Figure 6.** Sketch of the trapezoid array considered in the optimization procedure. Relevant geometric parameters (top width $b$, height $h$, base width $a$, and side angle $\theta_{side}$) are shown.

$h$) defined in Figure 6. The top corner of the microstructures is smoothed by a fillet of radius $r_{fil} = 0.2L_0$, to reproduce the experimental shape obtained by Im et al.[1,2] These parameters appropriately define the slenderness and aspect ratio of the structures. However, it is worth noticing that the length scale of the posts is another fundamental parameter in assessing the robustness of oleophobic surfaces.[20] Indeed, scaling down the posts while keeping the solid fraction constant would make the interface more robust to pressure deformation, while keeping the Cassie–Baxter angle fixed. One can expect that scaling down the size of the structures could improve mechanical robustness as well. However, nontrivial geometries such as inverse trapezoids are difficult to fabricate at arbitrarily small length scales with precision and regularity. At the same time, a high degree of control over aspect ratio and slopes can be achieved experimentally on micrometer-sized structures as described by Im and colleagues. It is therefore interesting to optimize such structures on a scalable unit cell, which should ideally be reproduced at the smallest length scale that assures perfection of features.

Since the existence of a suspended state is a necessary condition for oleophobicity, we will use the breakthrough pressure $P_B$ of the metastable state as the first measure of the performance of the oleophobic surface. For every choice of the design variables, we then apply an increasing pressure at the interface, until either of the failure mechanisms described in the modeling section triggers. Details on the

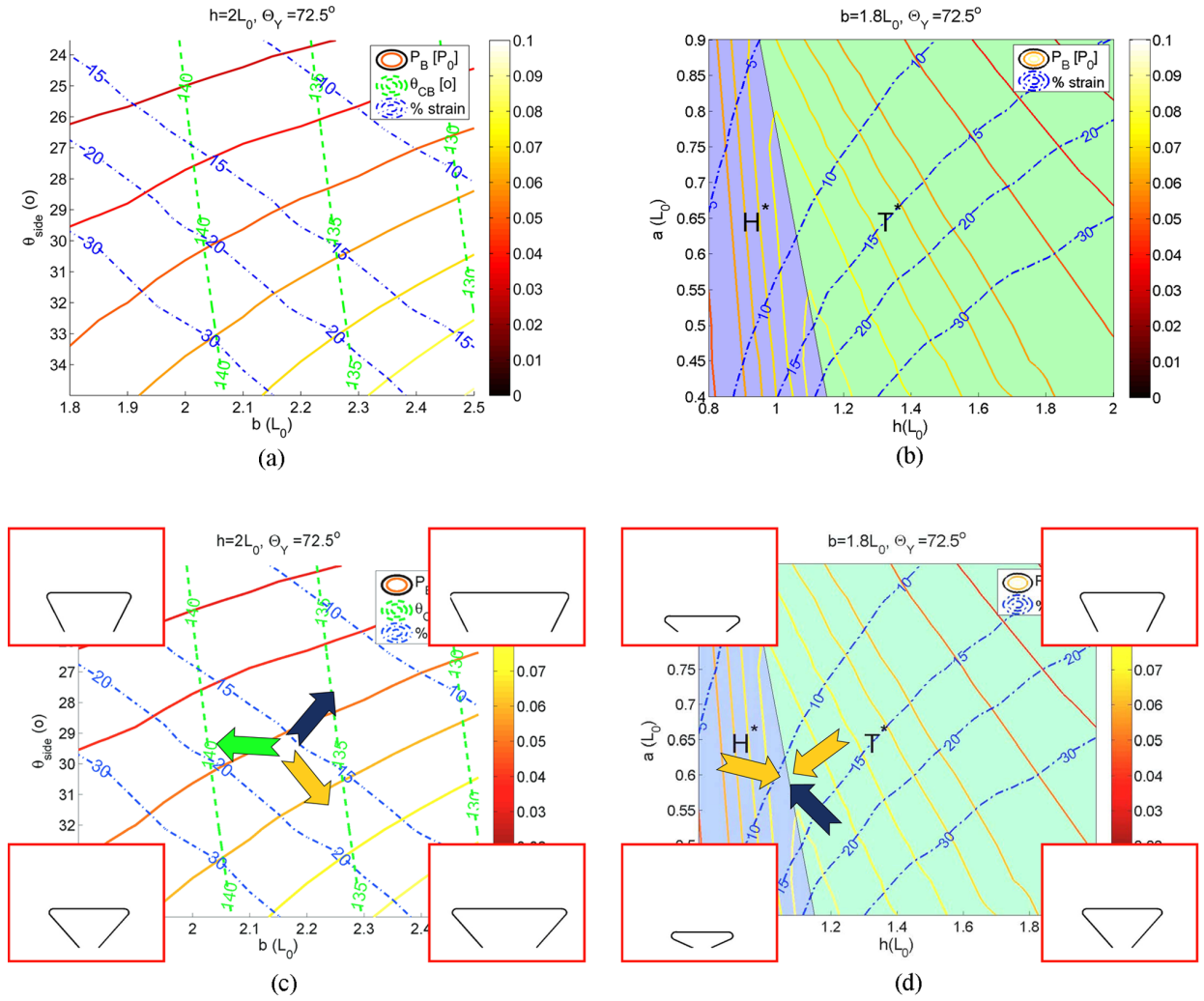


**Figure 7.** (a) $b$–$\theta_{side}$ parameter space ($h = 2L_0$), cos $\theta_Y = 0.3$. (b) $a$–$h$ parameter space ($b = 1.8L_0$), cos $\theta_Y = 0.3$. In each plot, the color legend is as follows: warm color scale, breakthrough pressure; green, apparent contact angle $\theta_{CB}$; blue, percent strain. The blue and green patches in (b) identify the H*- and T*-failure modes, respectively (see section 2). (c, d) copies of (a) and (b) showing the interplay of the optimality parameters. Each arrow represent an optimality direction, for mechanical robustness (blue), apparent contact angle (green), and maximum breakthrough pressure (orange). In each corner of the geometric space, the corresponding trapezoid is shown.


dx.doi.org/10.1021/la303853g | *Langmuir* 2012, 28, 17545–17551

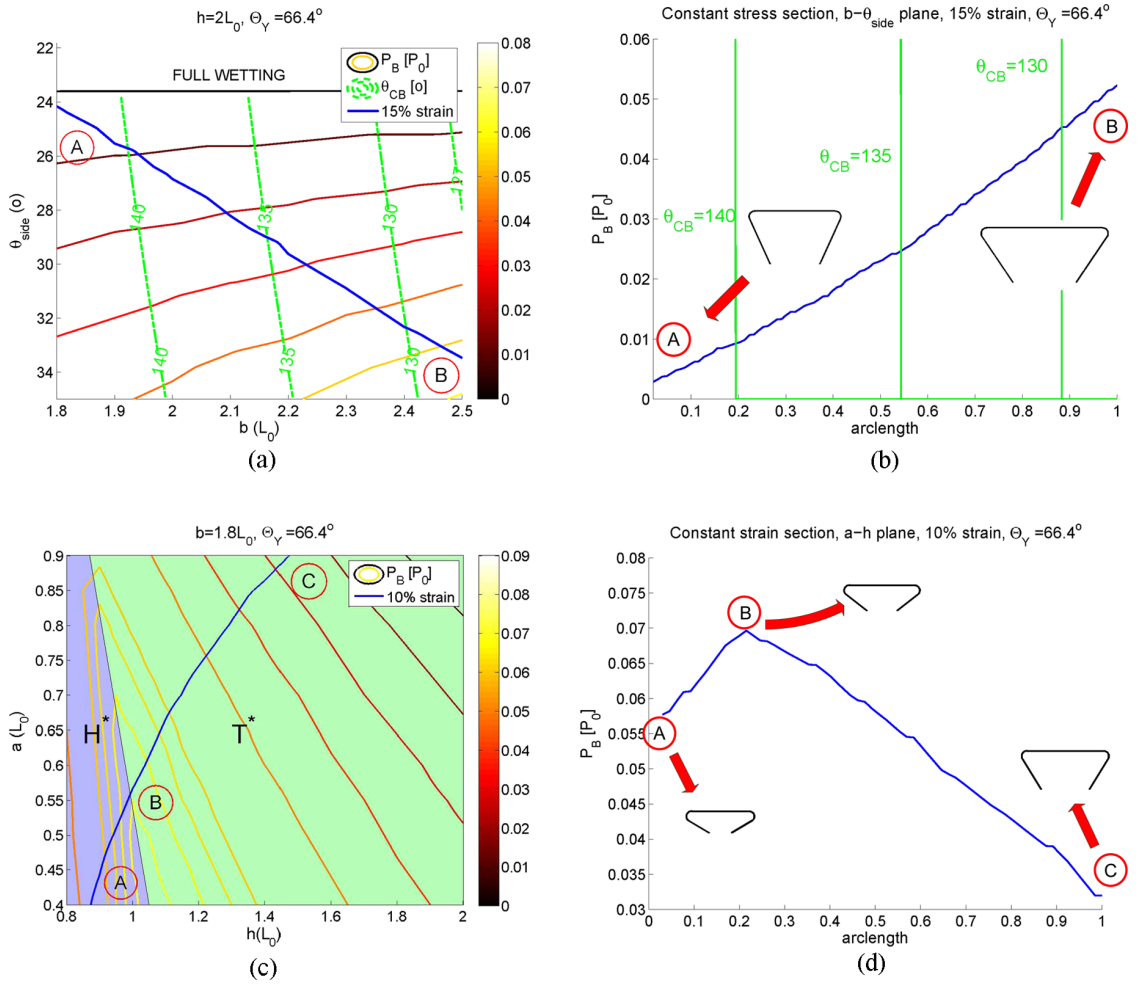


**Figure 8.** (a, c) $b-\theta_{side}$ and $a-h$ plots for cos $\theta_Y$ = 0.4 as in Figure 7a and b. A possible choice for a maximum strain contour is shown. (b, d) Breakthrough pressure along the contour in panels (a) and (c). Relevant positions in both plots are mapped using labels and corresponding geometries are also shown.

evaluation of $P_B$, consistently with the failure modes described in the previous section, can be found in the Supporting Information. Apart from the breakthrough pressure, we will include two further optimality parameters, that will be considered as constraints in defining admissible geometries. The first one is the apparent contact angle $\theta_{CB}$, which gives a clear indication of the degree of oleophobic or superoleophobic behavior shown by the textured surface. Since we assume the suspended configuration for drops, the Cassie expression eq 1 can be used to describe the apparent contact angle. A complete description of oleophobic behavior should also take contact angle hysteresis into account. This, however, would complicate the model significantly and is not strictly necessary in this work; it is reasonable to assume that a partially wetting configuration will show a modest hysteresis, if compared to a Wenzel/fully wetted configuration. The last parameter we include in our optimality analysis is a measure of the mechanical robustness of the inverse trapezoids. The ideal mechanical properties of the material can be achieved moving toward nanometric scale features, which will be almost atomically smooth. However, on the scale of several micrometers that we address in this work, the presence of cracks and other defects can lower the performance sensibly. The post will likely fail due to fracture propagations, which can be described in the framework introduced by Griffith. A detailed analysis of this phenomenon is however beyond the scope of the current work, where we want to assess how the shape and aspect ratio of the posts affects the mechanical performance as part of a broader parametric optimization. We will therefore introduce a simple yet relevant measure of the response of the structures to an applied shear load, which is the maximum principal strain in the structure. The utility of this measure is twofold. First, by measuring it, we can assess the range of validity of the linear approximation we use in modeling the elastomer structures. Second, we can expect large strains to be directly correlated to the onset of a tear-off failure. We then argue that a maximum strain threshold can be a useful confidence bound in characterizing such structures. As an example, we will consider a shear load of modulus $|\vec{\tau}| = P_0/2$ and a threshold strain of 10%−15%.

## 4. RESULTS AND DISCUSSION

To show the interplay of the different optimality parameters, we plot them as a function of the geometrical parameters introduced in the previous section, for a fixed Young contact angle cos $\theta_Y$ = 0.3 (i.e., $\theta_Y$ = 72.5°). In Figure 7a, we show the breakthrough pressure $P_B$ (plotted as contour lines in "warm" color scale), the apparent contact angle $\theta_{CB}$ (green dashed contours), and the maximum principal strain (blue dash-dot contours), as a function of the trapezoids top width $b$ and side angle $\theta_{side}$. The trapezoids height is fixed at $h = 2L_0$.

It can be seen that the three objective parameters present opposing trends. For example, a larger breakthrough pressure $P_B$ would be achieved, by increasing the top surface radius $b$, while keeping the side angle and cell size fixed. In this way, we


dx.doi.org/10.1021/la303853g | Langmuir 2012, 28, 17545−17551

effectively reduce the spacing between solid features. This means that a higher pressure would be required to cause a significant bulging of the liquid−air interface, which is at the origin of both the T*- and H*-failure modes. However, increasing $b$ would change the wetted solid fraction per unit cell, which results in a lower apparent contact angle $\theta_{CB}$, since the contact angle decreases with the wetted solid fraction per unit area. In the same way, a large $\theta_{side}$ for fixed top radius $b$ would reduce the risk of T*-failure. As explained in detail in the Supporting Information, the larger the undercut of the structures, the higher the pressure they can sustain while still satisfying eq 4. However, this results in a smaller base for the pillar, which implies very large stresses will build up at its neck, increasing the risk of failure and tear-off of the posts. From a design point of view, the geometric parameters space can then be imagined as partitioned into regions of almost constant $\theta_{CB}$ and strain values, inside which the geometry that gives the maximum $P_B$ is well-defined. If we instead considered only $P_B$-optimality, we would be led to asymptotically large values of $b$ and $\theta_{side}$. This corresponds to trapezoids with large top plate and minute supports, which would show modest contact angles and be prone to tear-off even for small applied loads. Similar considerations apply to Figure 7b, where we fix the pillar top width $b = 1.8L_0$ and change the height $h$ and base width $a$. Here a localized $P_B$ maximum exists in the $h$ parameter, corresponding to the transition from the T*-failure mode to the H*-failure mode. Because of the specific shape of inverse trapezoids, the height and side angle are connected by $\theta_{side} = \arctan((b - a)/h)$. In other words, if we make the posts higher for a fixed top area (this reducing the risk of H*-failure), we reduce $\theta_{side}$ (increasing the risk of T*-failure). Therefore, it is not convenient to arbitrarily increase the height of the posts, as would be the case for superhydrophobic surfaces, but the optimal height is rather the one for which both failures would happen for the same pressure. We find this optimal height is associated to a rather small aspect ratio $h/b$ for the trapezoids. Since the $b$ parameter is fixed, the apparent contact angle is almost constant at $\theta_{CB} \simeq 145°$ throughout Figure 7b (small variations coming only from the roundness of the corners), and is therefore not displayed in the picture. In the $a-h$ plane, the strain is minimum for short trapezoids with almost parallel wall (low $h$, large $a$), and grows with the side angle and height of the structures.

Plots like Figure 7a and b can then be considered optimality charts for oleophobic surfaces with specific constraints. The balance between optimality parameters is clearly depicted in Figure 7c and d, where each arrow points in the optimal direction for a given parameter (green for contact angle, blue for mechanical robustness, and orange for sustainable hydrostatic pressure). In each corner of the design parameter space, the correspondent geometry is also shown as an inset.

The usefulness of this analysis as a design tool can be shown by further restricting the performance constraints. To show the applicability of this method for different wetting configurations, let us also change the Young contact angle so that $\cos\theta_Y = 0.4$ (i.e., $\theta_Y = 66.4°$). In Figure 8a and c, we show a plot similar to Figure 7a and b, but with a fixed maximum strain contour (10% and 15%, respectively). If we move along this line, we get a curve for the $P_B$ behavior, as shown in Figure 8b and d. It is then possible to identify the most $P_B$-robust structures capable of supporting a prescribed mechanical stress, and associate them to the corresponding shape. Relevant positions in both plots are mapped using labels and correspondent post shapes are also shown.

## 5. CONCLUSION

In this paper, we describe a versatile and comprehensive approach to the optimization of oleophobic surfaces. We apply it to inverse trapezoid pillars, which were recently shown to be realizable in different shapes and aspect ratios. We find that, in order to identify a nontrivial optimum, several physical properties have to be taken into account, with the mechanical robustness of the pillars playing a fundamental role. Design charts showing the interplay of these objective parameters have been introduced for different values of the intrinsic contact angle of the substrate. In particular, a finite optimal height for the inverse trapezoids is found at the transition between different wetting modes, suggesting that low structures would be optimal. This result is quite interesting if compared to typical superhydrophobicity requirements for already hydrophobic materials. Further work directions will include considering wider parameter spaces, as well as substituting the static interface analysis used here with an approach that could capture dynamic effects.

## ■ ASSOCIATED CONTENT

### Supporting Information

Analytic derivation of breakthrough pressure. This material is available free of charge via the Internet at http://pubs.acs.org.

## ■ AUTHOR INFORMATION

### Corresponding Author

*E-mail: acav@nanotech.dtu.dk (A.C.); fridolin.okkels@nanotech.dtu.dk (F.O.).

### Notes

The authors declare no competing financial interest.

## ■ ACKNOWLEDGMENTS

The authors acknowledge the NanoVation consortium for funding this research. They thank Prof. Ole Hansen and Prof. Viggo Tvergaard for useful discussions and suggestions concerning the mechanical properties of the posts.

## ■ REFERENCES

(1) Im, M.; Im, H; Lee, J. H.; Yoon, J. B.; Choi, Y. K. A robust superhydrophobic and superoleophobic surface with inverse-trapezoidal microstructures on a large transparent flexible substrate. *Soft Matter* **2010**, *6*, 1401−1404.

(2) Im, M.; Im, H; Lee, J. H.; Yoon, J. B.; Choi, Y. K. Analytical Modeling and Thermodynamic Analysis of Robust Superhydrophobic Surfaces with Inverse-Trapezoidal Microstructures. *Langmuir* **2010**, *26*, 17389−17397.

(3) De Gennes, P.-G.; Brochard-Wyart, F.; Quéré, D. *Capillarity and wetting phenomena: Drops, Bubbles, Pearls, Waves*; Springer Science +Business Media: New York, 2004.

(4) Kreit, E.; Dhindsa, M.; Yang, S.; Hagedon, M.; Zhou, K.; Papautsky, I.; Heikenfeld, J. Laplace barriers for electrowetting thresholding and virtual fluid confinement. *Langmuir* **2010**, *26*, 18550−18556.

(5) Malvadkar, N. A.; Hancock, M. J.; Sekeroglu, K.; Dressick, W. J.; Demirel, M. C. An engineered anisotropic nanofilm with unidirectional wetting properties. *Nat. Mater.* **2010**, *19*, 1023−1028.

(6) Chu, K.-H.; Xiao, R; Wang, E. N. Uni-directional liquid spreading on asymmetric nanostructured surfaces. *Nat. Mater.* **2010**, *9*, 413−417.

(7) Tuteja, A.; Choib, W.; Mabryc, J. M.; McKinley, G. H.; Cohen, R. E. Robust omniphobic surfaces. *Proc. Natl. Acad. Sci. U.S.A.* **2008**, *105*, 18200−18205.
(8) Marmur, A. From Hygrophilic to Superhygrophobic: Theoretical Conditions for Making High-Contact-Angle Surfaces from Low-Contact-Angle Materials. *Langmuir* **2008**, *24*, 7573−7579.
(9) Nosonowski, M. Multiscale Roughness and Stability of Superhydrophobic Biomimetic Interfaces. *Langmuir* **2007**, *23*, 3157−3161.
(10) Lobaton, E. J.; Salamon, T. R. Computation of constant mean curvature surfaces: Application to the gas-liquid interface of a pressurized fluid on a superhydrophobic surface. *J. Colloid Interface Sci.* **2007**, *314*, 184−198.
(11) Liu, J.-L.; Feng, X.-Q.; Wang, G.; Yu, S.-W. Mechanisms of superhydrophobicity on hydrophilic substrates. *J. Phys.: Condens. Matter* **2007**, *19*, 356002−356014.
(12) Zheng, Q. S.; Yu, Y.; Zhao, Z.-H. Effects of Hydraulic Pressure on the Stability and Transition of Wetting Modes of Superhydrophobic Surfaces. *Langmuir* **2005**, *21*, 12207−12212.
(13) Emami, B.; Vahedi Tafreshi, H.; Gad-el-Hak, M.; Tepper, G. C. Predicting shape and stability of air-water interface on superhydrophobic surfaces with randomly distributed, dissimilar posts. *Appl. Phys. Lett.* **2011**, *98*, 203106.
(14) Brakke, K. The surface evolver. *Exp. Math.* **1992**, *1* (2), 141−165.
(15) Armani, D.; Liu, C.; Aluru, N. Re-configurable fluid circuits by PDMS elastomer micromachining. *Micro Electro Mech. Syst. (MEMS)* **1999**, 222−227.
(16) Mark, J. E. *Polymer Data Handbook*, 2nd ed; Oxford University Press: New York, 2009.
(17) Yu, Y.-S.; Zhao, Y.-P. Deformation of PDMS membrane and microcantilever by a water droplet: Comparison between Mooney−Rivlin and linear elastic constitutive models. *J. Colloid Interface Sci.* **2009**, *332*, 467−476.
(18) Dean, J. A. *Lange's handbook of chemistry*, 15th ed.; McGraw-Hill, Inc.: New York, 1999.
(19) Deng, T.; Varanasi, K. K.; Hsu, M; Bhate, N.; Keimel, C.; Stein, J.; Blohm, M. Nonwetting of impinging droplets on textured surfaces. *Appl. Phys. Lett.* **2009**, *94*, 133109.
(20) Chhatre, S. S.; Choi, W.; Tuteja, A.; Park, K.-C.; Mabry, J. M.; McKinley, G. H.; Cohen, R. E. Scale dependence of omniphobic mesh surfaces. *Langmuir* **2010**, *26*, 4027−4035.
(21) Ali, S. A.; Gauglitz, P. A.; Rossen, W. R. Stability of solids-coated liquid layers between bubbles. *Ind. Eng. Chem. Res.* **2000**, *39*, 2742−2745.

## Appendix C

# Paper 3: Modelling unidirectional liquid spreading on slanted microposts

Soft Matter

RSC Publishing

PAPER

View Article Online
View Journal

# Modelling unidirectional liquid spreading on slanted microposts

Cite this: DOI: 10.1039/c3sm00043e

Andrea Cavalli,*[a] Matthew L. Blow[b] and Julia M. Yeomans*[c]

A lattice Boltzmann algorithm is used to simulate the slow spreading of drops on a surface patterned with slanted micro-posts. Gibb's pinning of the interface on the sides or top of the posts leads to unidirectional spreading over a wide range of contact angles and inclination angles of the posts. Regimes for spreading in no, one or two directions are identified, and shown to agree well with a two-dimensional theory proposed in Chu, Xiao and Wang. A more detailed numerical analysis of the contact line shapes allows us to understand deviations from the two dimensional model, and to identify the shapes of the pinned interfaces.

Received 6th January 2013
Accepted 22nd February 2013

DOI: 10.1039/c3sm00043e

www.rsc.org/softmatter



## 1 Introduction

Unusual wetting and spreading properties of drops on natural and artificial surfaces can often be explained by the micro-structure of the substrate.[2] For example drops spreading on superhydrophobic surfaces patterned with micron-scale ridges reach an elongated final state,[3,4] and a drop imbibing into a surface patterned with posts can form a faceted final configuration, which reflects the symmetry of both the lattice and of the posts themselves.[5]

The physics behind this behaviour was first described by Gibbs, who pointed out that an interface can pin on the edge of a post over a range of angles, as illustrated in Fig. 1. The pinning occurs because there is a free energy penalty to the interface moving away from the edge in either direction as it would then have to form an angle with the adjacent surface which differs from the equilibrium contact angle. A pinning strength that depends on the lattice direction leads to the drop having one or more preferred directions of motion, and hence anisotropic drop movement and shapes.

In this paper we focus on unidirectional drop motion: where the symmetry of the underlying surface structure can pick out one easy direction of spreading.[6,7] Such surfaces occur naturally, for example, the unidirectional motion of droplets on butterfly wings results from their ratchet-like structure,[8,9] and rye-grass leaves shed water in a preferred direction[10] due to the asymmetric contact angle hysteresis. Microfabricated surfaces that lead to uni-directional motion are a very recent development. Unidirectional spreading has been observed on bent silicon micro pillars,[1] while other authors[11,12] were able to transport droplets on vibrating ratchet structures. Similar results where obtained using PDMS replicas of the naturally occurring asymmetric micro-texture[10] taken from rye grass, and anisotropic hysteresis was observed on printed ratchetlike surfaces.[13] Despite the different material and geometries employed, the unidirectional liquid motion consistently reflects the asymmetry of the substrate on microscopic length scales. This highlights the importance of understanding the underlying physical phenomena involved.

In this paper, we use a two-phase lattice Boltzmann algorithm to model imbibition on an hydrophilic surface patterned with slanting posts, varying the contact angle of the substrate and the tilt angle of the posts. For a range of contact angles we observe a single, preferred spreading direction as observed in recent experiments.[1] The results are in good qualitative agreement with a two-dimensional model of the uniaxial spreading proposed in ref. 1, and enable us to describe the corrections to

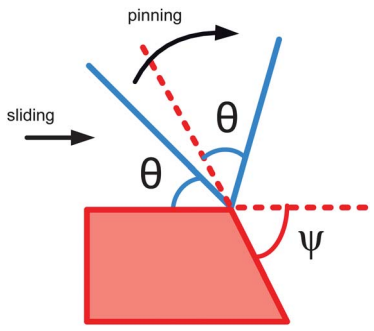


**Fig. 1** Gibbs' pinning on the corner of a post. The interface (blue line) remains pinned to the post over the range of angles indicated by $\psi$ as there is a free energy barrier to its moving in either direction.

[a]*Department of Micro- and Nanotechnology, Technical University of Denmark, DTU Nanotech, Building 345 East, DK-2800 Kongens Lyngby, Denmark. E-mail: acav@nanotech.dtu.dk*

[b]*Centro de Física Teórica e Computacional Instituto de Investigação Interdisciplinar Av. Prof. Gama Pinto, 2 P-1649-003 Lisboa, Portugal*

[c]*The Rudolf Peierls Centre for Theoretical Physics, Oxford University, 1 Keble Road, Oxford OX1 3NP, UK. E-mail: j.yeomans1@physics.ox.ac.uk*

the model for a three dimensional geometry. By visualizing the shape of the contact line we describe in detail the mechanisms through which the interface pinning and de-pinning occurs.

## 2 The model liquid

### 2.1 Governing equations

To model a two phase system interacting with a surface, we apply a diffuse interface scheme. The thermodynamic state of the fluid is described at every point $\vec{x}$ and time $t$ by its density $\rho(\vec{x},t)$. The free energy of the system, $\Psi$, is taken as a Landau double-well potential with the addition of a derivative term representing the surface tension, and a surface contribution of the form proposed by Cahn:[14]

$$\Psi = \iiint_D \left(\psi_b(\rho) - \mu_b\rho + \frac{1}{2}\kappa|\nabla\rho|^2\right)\mathrm{d}V - \iint_{\partial D}\mu_s\rho\mathrm{d}S. \quad (1)$$

The first term in the integrand of (1) is the bulk free energy density[15]

$$\psi_b(\rho) = p_c[(\nu^2 - \beta\tau_W)^2 - (1 - \beta\tau_W)^2] \quad (2)$$

where $\rho_c$, $p_c$, $\tau_W$ and $\beta$ are, respectively, the critical density, critical pressure, reduced temperature and a free parameter controlling the density difference between phases and $\nu = \frac{\rho - \rho_c}{\rho_c}$ is a normalised density. This potential leads to two equilibrium bulk densities $\rho_e = \rho_c(1 \pm \sqrt{\beta\tau_W})$. $\mu_b$ is a Lagrange multiplier constraining the total mass of fluid, while the third term in the free energy expression is an interface energy cost, tunable through the parameter $\kappa$, associated with density gradients. It allows for solutions with a diffuse interface between phases, with surface tension $\gamma$ and width $\chi$:

$$\gamma = \frac{4}{3}\rho_c\sqrt{2\kappa p_c(\beta\tau_W)^3}, \quad \chi = \frac{1}{2}\rho_c\sqrt{\frac{\kappa}{\beta\tau_W p_c}}. \quad (3)$$

The final term in eqn (1) is the surface contribution to the free energy $\Psi$. When $\Psi$ is minimised this gives the boundary condition $\partial_\perp\rho = -\mu_s/\kappa$ which fixes the value of the density at the solid surface. The Young contact angle $\theta$ at the surface is related to the surface chemical potential by[15]

$$\mu_s = 2\beta\tau_W\sqrt{2p_c\kappa}\sin\left(\frac{\pi}{2} - \theta\right)\sqrt{\cos\frac{\alpha}{3}\left(1 - \cos\frac{\alpha}{3}\right)}, \quad \alpha = \arccos\left(\sin^2\theta\right). \quad (4)$$

In our simulations, the main parameters are set as follows: $\kappa = 0.01, p_c = 0.125, \beta = 1, \tau_W = 0.3, \rho_c = 3.5$. The corresponding surface tension is $\gamma = 0.04$ and the surface thickness is $\chi = 0.9$ (in simulation units).

The hydrodynamics of the fluid is described by the continuity and Navier–Stokes equations:

$$\partial_t\rho + \partial_\alpha(\rho u_\alpha) = 0, \quad (5)$$

$$\partial_t(\rho u_\alpha) + \partial_\beta(\rho u_\alpha u_\beta) = -\partial_\beta P_{\alpha\beta} + \partial_\beta(\rho\eta[\partial_\beta u_\alpha + \partial_\alpha u_\beta] + \rho\lambda\delta_{\alpha\beta}\partial_\gamma u_\gamma), \quad (6)$$

where $\boldsymbol{u}$ is the fluid velocity field and $\eta$ and $\lambda$ are the shear and bulk kinematic viscosities, respectively. $\partial_t$ represents a time derivative and $\partial_\alpha$, $\partial_\beta$ spatial derivatives (Einstein summation convention is assumed). The connection between the thermodynamic and fluid dynamic of the system arises through the pressure tensor $\boldsymbol{P}$, which is derived from the free energy (1). Eqn (5) and (6) are solved using the Lattice Boltzmann method. Details of the implementation can be found in ref. 9 and 15.

### 2.2 Geometry

Each post has a square cross-section of dimensions $w$, which was typically chosen to be equal to 5 or 10 computational grid spacings. The posts are tilted at an angle $\phi$ to the positive $x$-axis, and extend to a height $h = 4w$ above the surface. We start considering a rectangular array of posts with lattice constant $a_x = 4.6w$ in the $x$ direction and $a_y = 4w$ in the $y$ direction as shown in Fig. 2.

Placing a sufficiently large drop on the surface to allow significant spreading through the posts is computationally expensive. Therefore we define a reservoir of fluid in the centre of the post array typically extending across $\simeq 10w$ and reaching to the top of the posts. If the fluid density inside the reservoir decreases below the equilibrium density of the liquid phase, new mass is slowly added to feed the imbibition. The contact angle of the liquid with both the posts and the substrate is $\theta$ which we vary in the range 30° to 70°. This range is representative of different hydrophilic material, for example the polymers considered in ref. 1 or 16.

We first consider a quasi-2D geometry which allows us to concentrate on the directional spreading in the $x$-direction. We choose a simulation box of length $40w$ in the $x$-direction, $4w$ in the $y$-direction and $6w$ along $z$, with periodic boundary conditions along both $x$ and $y$. The reservoir spans the simulation box in $y$ corresponding to simulating a cylindrical drop with

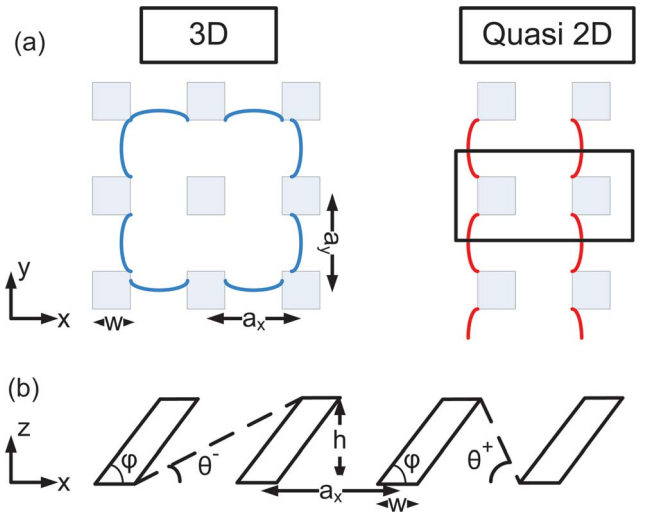


**Fig. 2** (a) Diagrams to contrast the quasi-2D and full 3D geometries used in the simulations. The red and blue lines represent typical interface positions. (b) Side view of the posts showing the interface geometry corresponding to the threshold for movement which is assumed in deriving eqn (7).

interfaces which lie, on average, parallel to the $y$-direction. The average of any fluid motion is along $x$. We then present results for a full 3D geometry, using a simulation box with typical dimensions $40w \times 32w \times 6w$, with periodic boundary conditions along $x$ and $y$. A schematic comparison of quasi-2D and 3D spreading is given in Fig. 2a.

## 3 Results

Fig. 3 shows snapshots of the imbibition process as a function of time for the quasi-2D geometry and a contact angle $\theta = 45°$. The interface advances in the positive $x$-direction, but not in the negative $x$-direction, because of pinning on the posts. As pointed out in Chu *et al.*[1] a good understanding of why this occurs follows from assuming that the interface is pinned at the top corner of the posts and ignoring any interface curvature along $y$. We illustrate this situation in Fig. 2b. The bottom of the interface will advance along the surface until it reaches the equilibrium contact angle $\theta$. If this enables the interface to reach the next post it will wet this post and move forwards, if not, it will remained pinned because any forward motion will increase the free energy. Because of the two dimensional nature of the model, it is easy to work out the threshold Young angles for spreading in the two directions as a function of the post geometry. Defining these as $\theta^+$ and $\theta^-$ for spreading along $+x$ and $-x$ respectively, gives[1]

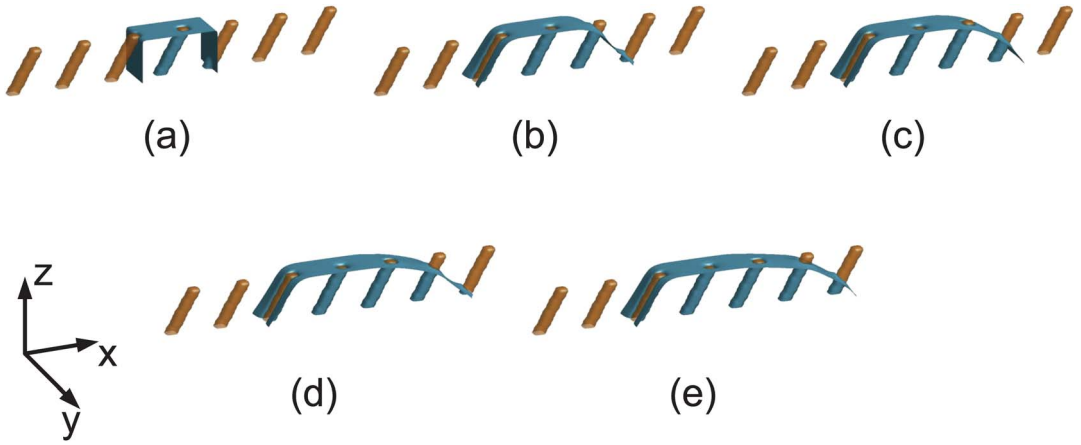


**Fig. 3** Advancing front in the unidirectional spreading regime for contact angle $\theta = 45°$ and post angle $\phi = 60°$. This is a quasi-2D geometry with periodic boundary conditions along $y$. The snapshots (a)–(e) correspond to 0, 1, 2, 4, $5 \times 10^4$ time steps.

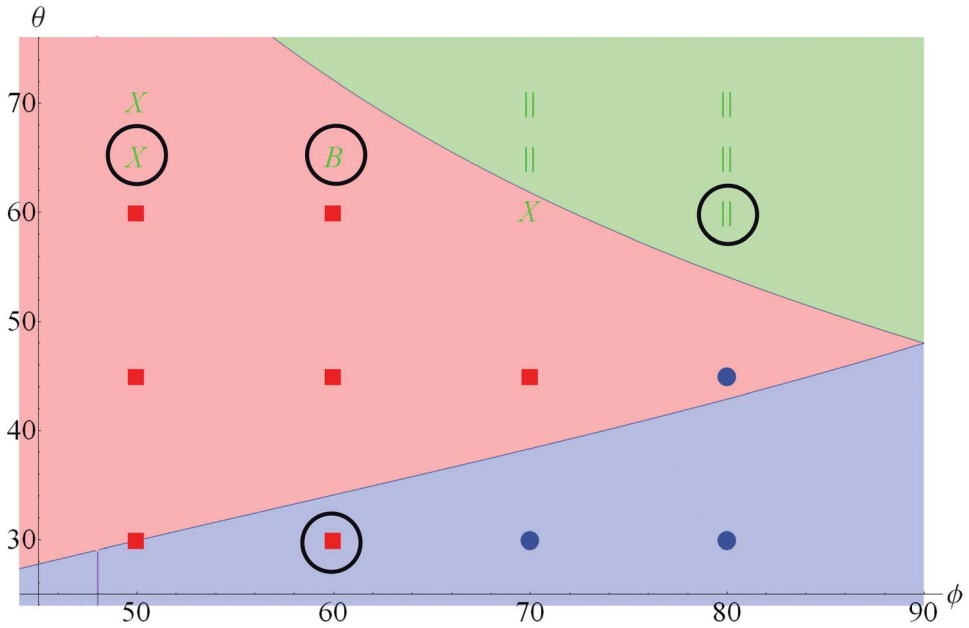


**Fig. 4** Plot of the different wetting regimes in the quasi-2D geometry, as a function of wetting angle $\theta$ and post angle $\phi$. The other geometric parameters are: $a_x = 4.6w$, $h = 4w$. The legend is: blue/circles: bidirectional spreading, red/squares: unidirectional spreading, green: no spreading. The different green symbols represent different pinning modes in the forward direction, as described in Fig. 5. Selected configurations (black circles) are shown in Fig. 5. The background indicates wetting regimes from a theory assuming a 2D geometry, see eqn (7).[1]

$$\theta_{cr,\pm X} = \tan^{-1}\left(\frac{H}{a_x - w \mp H\cot(\phi)}\right). \quad (7)$$

Thus there are three regimes: the interface can remain pinned in both directions, advance just along $+x$, or move forward in both directions. The different regimes predicted by eqn (7) are indicated in Fig. 4 as a function of the Young angle $\theta$ and the post inclination $\phi$. Note that, for $\phi = 90°$, $\theta^+ = \theta^-$ as expected. The value of $a_x$ also affects the transition between different spreading regimes, as is apparent from eqn (7): closer posts will ease the spreading, while posts that are further apart will make it more difficult. Our choice of $a_x = 4.6w$ allows us to observe the different spreading regimes over the range of contact angles $\theta$ and slanting angles $\phi$ we consider.

Fig. 4 also shows the results of simulations for the quasi-2D geometry. All three regimes are reproduced in the simulations. The analytic model gives a good account of the boundaries between them, but spreading in both directions is slightly more difficult than predicted by the 2D theory. The simulations allow us to identify this as being due to the details of the interface pinning on the posts. For an interface advancing along the positive $x$-axis, where the post points towards the direction of travel, we observe three different possible pinning mechanisms, labelled ||, B and X in Fig. 5. If the post is almost vertical, the leading interface is disconnected and is pinned to the vertical sides of the post (|| label). For a more pronounced post tilt the interface remains disconnected, but does not reach the top of the final post (B label). For large tilt the leading interface is connected and has reached the equilibrium contact angle on the substrate. However, in contrast to two dimensions, the final post is only partially wet (X label). The situations, B and X, where the interface has only reached the top of the penultimate post is only observed for slanted posts. It occurs because the interface can take the correct contact angle on the final post without a large penalty in curvature energy. The interface configuration resembles that in the partially suspended state identified in Kusumaatmaja and Yeomans.[9] We considered a small spacing between posts to facilitate spreading over a wide range of wetting angles. It is worth noticing however that, if the spacing between posts were increased in the spreading direction, configurations analogous to the 2D theory would likely appear, with pinning on the final rather than penultimate row of posts.

In the hard direction for spreading, $-x$, the interface is pinned at the edges of the final line of posts, adjusting to their slope, as shown in Fig. 5, label *. Bidirectional spreading only occurs for very low contact angles $\theta < 30°$ or posts close to vertical $\phi > 70°$.

These simulations correspond to quasi-static spreading, with the fluid reservoir replenished very slowly. Borderline configurations between different wetting modes (such as $\phi = 70°$, $\theta = 60°$) are very sensitive to exact details of the position and filling speed of the reservoir. This is expected because the free energy barriers and capillary forces driving the flow are very small. A comparison between two resolutions used shows that, as expected, spreading is slightly more difficult for a narrower interface. We also note that, if the rate at which fluid is added to the reservoir is increased, the resulting inertia allows the fluid to de-pin from the top of the posts, forming a spherical cap.

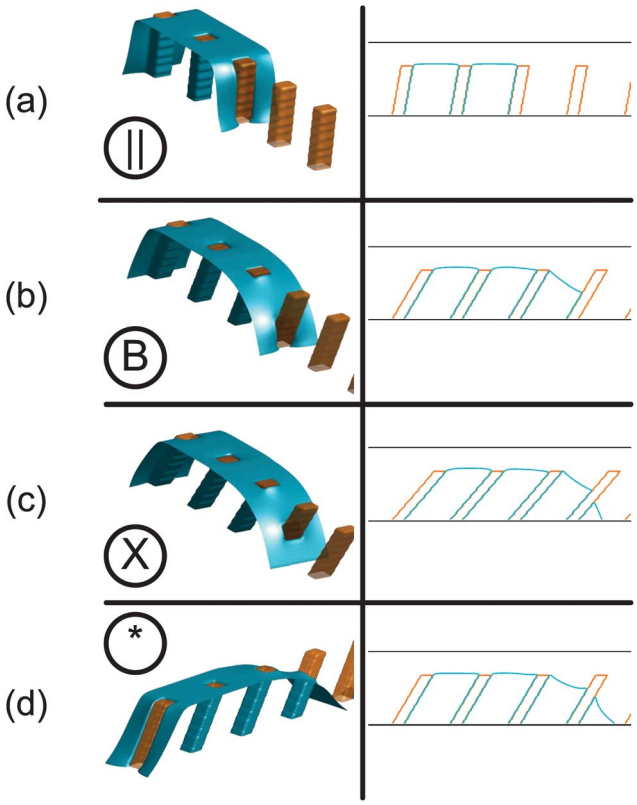


**Fig. 5** Different pinning configurations appearing in the quasi 2D simulations. The first three correspond to the easy spreading direction, $x$, while the last shows the typical pinning in the hard direction, $-x$. They can be identified with the circled points in Fig. 4 by matching symbols. Cross-sections taken through the centres of the posts are shown on the right as full blue lines. (a) If the post is almost vertical, the leading interface is disconnected and pinned to the vertical sides of the post (|| label). (b) For more pronounced post tilt the interface remains disconnected, but does not reach the top of the final post (B label). (c) For large tilt the leading interface is connected and has reached the equilibrium contact angle on the substrate. However, in contrast to two dimensions, the final post is only partially wet (X label). (d) The interface in the negative $x$-direction is disconnected, and pinned by the sides of the final post (* label).

We next report a full three-dimensional simulation which allows the fluid to spread along both $x$ and $y$. The reservoir is defined as a circular region of radius $10w$ in the centre of the domain, and the contact angle is $\theta = 45°$. In Fig. 6 we plot contour lines showing the spreading of the drop base for subsequent time steps. The first plot is for vertical posts; as expected it reflects the symmetry of the lattice. In the second plot the lattice spacing is the same, but the posts are now slanted with $\phi = 60°$. In the slanting direction the behaviour is consistent with the quasi-2D model, with the liquid spreading only in the positive $x$ direction. The spreading in the $y$ direction is comparable to the vertical post case. The overall dynamics closely resembles the imbibition observed in experiments by Chu *et al.*[1] In Fig. 6c the posts are closer in the $x$-direction. One can see that the asymmetry of the spreading becomes more pronounced, with the fluid spreading easily

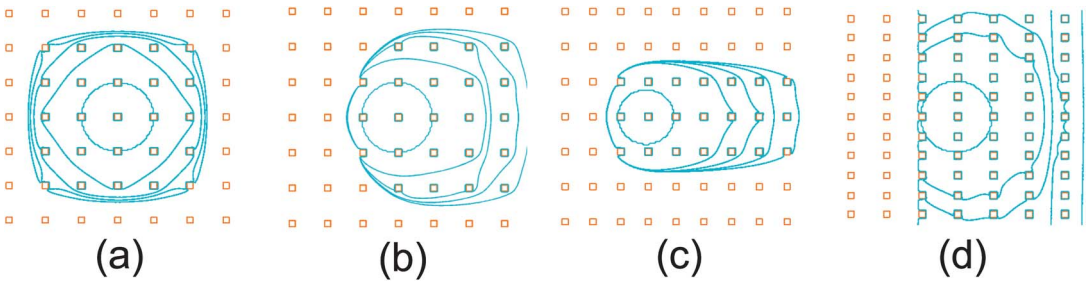


**Fig. 6** Three dimensional spreading for $\theta = 45°$ and (a) $\phi = 90°$, $a_x = a_y = 4.6w$. (b) $\phi = 60°$, $a_x = a_y = 4.6w$. (c) $\phi = 60°$, $a_x = 3.6w$, $a_y = 4.6w$. (d) $\phi = 60°$, $a_x = 4.6w$, $a_y = 2.53w$. Contours showing the interface position at the base of the drop are taken every $4 \times 10^4$ time steps.



from one row to the next along $x$, while only spreading very slowly along $y$. This occurs because the thermodynamic driving force for spreading is much stronger in the $x$ direction. For a contact angle of 45° there is slow spreading along $y$, however for a larger contact angle the fluid will remained pinned along $y$ (the crossover can be estimated from eqn (7), taking $\phi = 90°$ in Fig. 4), and/or $x$ (as seen in the quasi-2D simulations reported in Fig. 4). Eventually, in Fig. 6d, we simulate densely packed posts in the $y$ direction, while keeping the same $x$ spacing as in Fig. 6b. The behavior is now quite different, with the spreading happening first in the transverse direction, and only subsequently along the slanting direction. The unidirectionality is however maintained. These results indicate that the final shape of a spreading drop can be tuned in detail by varying the lattice geometry and tilt angle of the posts, while retaining the relevant property of unidirectionality.

## 4 Conclusions and outlook

We have applied a lattice Boltzmann algorithm for two phase flow to model the spreading of liquid drops on a surface patterned by a lattice of slanted micro-posts. Gibb's pinning of the interface on the sides or top of the posts led to unidirectional spreading over a wide range of fluid-substrate contact angles and inclination angles of the posts. Regimes for spreading in no, one or two directions were identified, and shown to agree well with a two-dimensional theory proposed by Chu *et al.*[1] A more detailed numerical analysis of the contact line configurations enabled us to understand deviations from the two dimensional model, and to identify the configurations of the pinned interfaces.

The final drop shape depends on spacing of the post lattice, the contact angle, and the geometry and inclination of the posts. Our simulations correspond to slow spreading, but inertial terms will also alter the final drop configuration. Thus there are many, varied possibilities to use slanted posts to control drop shapes or the direction of a flowing stream of fluid. Contact angles can be varied *in situ* by electrowetting, and it would be of interest to design substrates with addressable posts where the contact angle of each of the posts could be varied independently to allow steering of microfluidic flows.

## Acknowledgements

AC acknowledges the NanoVation consortium for funding this research. He also acknowledges Otto Mønsted fonden, Reinholdt W. Jorck fonden and P.A. Fisker for travel and accommodation support during the collaboration between the institutes. MLB acknowledges the support of the Portuguese Foundation for Science and Technology (FCT), through the grants SFRH/BDP/73028/2010 and PEst-OE/FIS/UI0618/2011. JMY acknowledges support from the ERC Advanced Grant MiCE.

## References

1 K. H. Chu, R. Xiao and E. N. Wang, *Nat. Mater.*, 2010, **9**, 413–417.
2 P. G. De Gennes, F. Brochard-Wyart and D. Quéré, *Capillarity and wetting phenomena: drops, bubbles, pearls, waves*, Springer Verlag, 2004.
3 Y. Chen, B. He, J. Lee and N. A. Patankar, *J. Colloid Interface Sci.*, 2005, **281**, 458–464.
4 F. Zhang and H. Y. Low, *Langmuir*, 2007, **23**, 7793–7798.
5 M. L. Blow and J. M. Yeomans, *Philos. Trans. R. Soc., A*, 2011, **369**, 2519–2527.
6 M. J. Hancock, K. Sekeroglu and M. C. Demirel, *Adv. Funct. Mater.*, 2012, **22**, 2223–2234.
7 C. W. Extrand, *Langmuir*, 2007, **23**, 1867–1871.
8 Y. Zheng, X. Gao and L. Jiang, *Soft Matter*, 2007, **3**, 178–182.
9 H. Kusumaatmaja and J. M. Yeomans, *Soft Matter*, 2009, **5**, 2704–2707.
10 P. Guo, Y. Zheng, C. Liu, J. Ju and L. Jiang, *Soft Matter*, 2012, **8**, 1770–1775.
11 N. A. Malvadkar, M. J. Hancock, K. Sekeroglu, W. J. Dressick and M. C. Demirel, *Nat. Mater.*, 2010, **9**, 1023–1028.
12 K. Sekeroglu, U. A. Gurkan, U. Demirci and M. C. Demirel, *Appl. Phys. Lett.*, 2011, **99**, 063703.
13 M. Barahman and A. M. Lyons, *Langmuir*, 2011, **27**, 9902–9909.
14 J. Cahn, *J. Chem. Phys.*, 1977, **66**, 3667.
15 A. J. Briant, A. J. Wagner and J. M. Yeomans, *Phys. Rev. E: Stat., Nonlinear, Soft Matter Phys.*, 2004, **69**, 031602.
16 R. J. Vrancken, M. L. Blow, H. Kusumaatmaja, K. Hermans, A. M. Prenen, C. W. Bastiaansen, D. J. Broer and J. M. Yeomans, *Soft Matter*, 2013, **9**, 674–683.